NONDESTRUCTIVE TESTING FOR CORROSION

ASSESSMENT OF EPOXY COATED REBAR

By

KRISTIN KARLESKINT

Bachelor of Science in Civil Engineering

Oklahoma State University

Stillwater, Ok.

2018

NONDESTRUCTIVE TESTING FOR CORROSION

ASSESSMENT OF EPOXY COATED REBAR

Thesis Approved:

_____

Dr. Julie Ann Hartell

Thesis Adviser

_____

Dr. Robert Emerson

Committee Member

_____

Dr. Yongwei Shan

Committee Member

ACKNOWLEDGEMENTS

None of the writing herein could have been possible without the endless emotional support from my family and mentor. None of the data would have been attainable without help and lab support from many other students.

Thank you, mom and dad, for leading by example and showing me what it means to work hard for something.

Thank you Julie, for everything you have taught me about concrete, the world and myself. Thank you for not giving up on me, when so many others would have and making me realize my worth when I was blind to it.

I would like to express my gratitude towards all graduate and undergraduate research assistants who have helped me collect data and better understand my thesis goals. Thank you Evan Karunaratne, Cody Shults, Austin Cratty, Trevor Galusha, Brock Turner, Nathan Brooks and Joe Fodor. Thanks for all the stories and laughs on the long days spent collecting data in the freezing winter and summer heat.

I want to give a special thanks to PhD student, Hang Zeng, for his selflessness. Thank you Hang, for always going out of your way to help others, explain different test principles to me, and help me troubleshoot equipment problems when you had your own work to do. Your kindness does not go unseen.

Thank you to my committee members for taking the time to read and advise me further on my thesis:

Thank you Dr. Emerson for teaching me what it means to make the most of something and be lighthearted at all times. I admire how you solve problems with curiosity and creativity; I hope to be like that someday.

Name: KRISTIN KARLESKINT

Date of Degree: DECEMBER, 2020

Title of Study: NONDESTRUCTIVE TESTING FOR CORROSION ASSESSMENT OF

EPOXY COATED REBAR

Major Field: CIVIL ENGINEERING

Abstract:

The corrosion of reinforcement is a leading cause of structural deficiency and the reduction of a structure's service life. To enhance structural performance and ensure that each structure meets its intended design life, it is important that corrosion be mitigated and monitored. Epoxy coated rebar (ECR) was first introduced in 1973 and has since been implemented in bridge decks by at least 41 state transportation departments due to the increased usage of deicing salts and the related corrosion problems. It has been observed in some case studies that the inclusion of ECR either increased the risk of corrosion or that it did not improve the corrosion resistance of the bridge deck. Due to an increasing demand for more resilient and sustainable structures, a method to properly test and evaluate the condition of ECR is necessary to determine the service life and to propose an adequate maintenance or rehabilitation program.

The half-cell potential is the most common test for in-situ corrosion assessment, but only provides insight on the probability of corrosion and must be supplemented by other forms of non-destructive testing (NDT). In this study, other NDT methods are used to supplement half-cell potential including: visual assessment, ultrasonic pulse velocity, rebound hammer and pulse echo. High and low corrosion risk areas will be identified in the non-destructive survey and verified with lab testing of cores obtained from these areas. Evaluation of the correlations between the nondestructive survey and mechanical properties of the concrete and reinforcement will determine the efficacy of using this test methodology for corrosion identification in the field.

The proposed methodology will be performed on 9-inch-thick reinforced bridge-deck slabs from I-35 in Oklahoma. The bridge was constructed with both standard and epoxy coated rebar; a corrosion assessment of the standard rebar will be used for comparison and validation of the ECR assessment. The experimental results will reveal the accuracy of the test methodology compared to standard rebar assessment and determine if it is adequate to evaluate the probability of corrosion in bridge decks with ECR.

TABLE OF CONTENTS

LIST OF TABLES

LIST OF FIGURES

Figure Page

Figure   Page

CHAPTER I

INTRODUCTION

The US Federal Highway Administration conducted a study in 2002 which revealed the
direct cost associated with corrosion in the transportation infrastructure industry. A
surprising $8.3 billion was estimated to be spent on the replacement and maintenance of
bridges every year. When indirect costs to the user such as traffic delays and loss of
productivity were included, the cost increased as much as 10 times that seen in the direct
corrosion cost estimate (FHWA 2002). The rapid deterioration and high costs associated
with corrosion in bridges has been combatted since the 70's with efforts being made to
prevent the onset of corrosion through improvement of the steel reinforcement and the
surrounding concrete.

The primary methods of corrosion mitigation include the use of alternative types of
reinforcement and implementation of sacrificial anodes. Of the choices, the cheapest and
most widely used option is the replacement of black rebar with epoxy coated rebar
(ECR). In most moderate exposure conditions, the replacement of black rebar in the top
mat with ECR has proven to be highly successful at corrosion prevention. However, at
the time of its inception, the extent of the benefits to this practice were unknown. The
Oklahoma Department of Transportation (ODOT) foresaw an opportunity to study these
benefits when constructing the first ECR bridge in Oklahoma by implementing ECR in
only half of the structure. This provided a great opportunity to compare the in-service
benefits of a structure which underwent a full service life of real loading and exposure
conditions. Corrosion is a concern for structures as it can result in a decrease in structural

capacity and performance. Corrosion products will result in a loss of cross sectional area of reinforcement and destroy the bond between the steel and concrete, both of which can result in structural failure under loading (Cabrera 1996). A decrease in structural performance is the result of cracking and the subsequent increase in deflection. Both insufficient structural capacity and poor performance can lead to extensive maintenance and repair in a highly serviced bridge.

In order to better understand and quantify the effects of rebar type, a comparative assessment of the ECR and black rebar was performed. The comparative assessment consisted of two major parts (1) a non-destructive evaluation which is indicative of the material quality during a field assessment and (2) a destructive assessment in order to compare the mechanical properties of the bridge. The non-destructive survey consisted of four commonly practiced tests including the visual assessment, surface hardness survey, pulse-echo survey and half-cell potential mapping. Of these, the half-cell potential test is the most used test for corrosion assessment in the field. In principal, the half-cell potential test should be unfeasible in coated rebar but this study will assess the viability of its use for ECR since there is no standard yet for its use with any alternative reinforcement. The destructive assessment will include the collection of cores and conduction of tests including ultrasonic pulse velocity (UPV), bulk resistivity, modulus of elasticity and compression strength. Additionally, colorimetric methods will be used to aid the results of mechanical testing including tests for carbonation depth, chloride penetration and silane treatment. The destructive assessment will divulge the effect of rebar type on material condition and further investigation of the rebar will aid in determining the true effectiveness of ECR implementation for the climate and exposure conditions of Oklahoma.

CHAPTER II

REVIEW OF LITERATURE

This literature review was prepared with the intent of covering all possible topics that will arise in the results and discussion section. Corrosion mechanisms, concrete durability mechanisms, rebar performance and current methods for corrosion assessment are discussed to provide a comprehensive understanding of corrosion as it relates to reinforced concrete structures. In addition to this, the theory and working mechanics behind each non-destructive test will be referenced as well as the material properties and atmospheric conditions that affect their results.

2.1 Corrosion Mechanism

Corrosion is the widely known term used to describe the product of a reaction between metal oxides/hydroxides with water and oxygen. The corrosion process is caused by two electrochemical reactions: the oxidation of a metal (anodic reaction) and the reduction of an oxidizing agent (cathodic reaction).

$$\text{Anodic Reaction: } Fe \rightarrow Fe^{2+} + 2e^-$$

$$\text{Cathodic Reaction: } 2e^- + H_2O + \frac{1}{2}O^2 \rightarrow 2OH^-$$
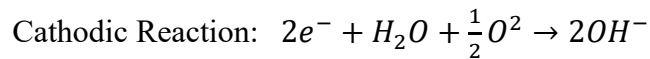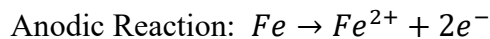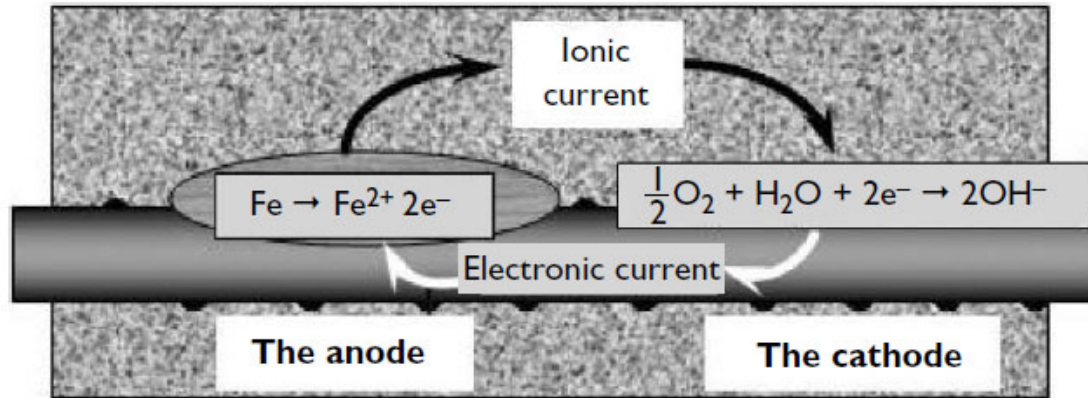
Figure 2.1: Anodic and Cathodic Reactions of Steel Corrosion

In the case of steel rebar, the anodic reaction is always the dissolution of Iron due to the oxidation of the surface atoms which results in the release of ferrous ions into the concrete pore solution. In order to maintain a net zero current, water and oxygen are reduced and consume the electrons that are released during oxidation to form hydroxides. The movement of ferrous ions between the anodic and cathodic sites is facilitated by the concrete pore solution which serves as an electrolyte. These reactions are perfectly counterbalanced and each contribute one-half of the whole process that is known as corrosion. The chemical reactions that produce corrosion products are shown in the formulae below (Oudar and Marcus 1995):

Ferrous Hydroxide: $Fe^{2+} + 2OH^- \rightarrow Fe(OH)_2$

Ferric Hydroxide: $4Fe(OH)_2 + O_2 + 2H_2O \rightarrow 4Fe(OH)_3$

Ferric Oxide (red rust): $2Fe(OH)_3 \rightarrow Fe_2O_3 * H_2O + 2H_2O$
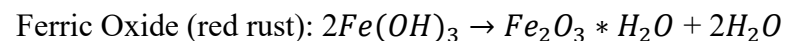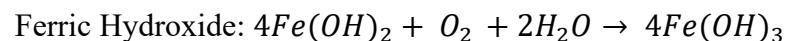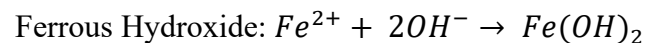
The corrosion process is initiated by the movement of electrons from high to low density areas within the steel. This relocation of electrons is dependent on the presence of imperfections and dislocations within the crystal structure of the steel. This means that the metallurgical state of the rebar due to cold working, annealing, grain size and boundaries is deterministic of iron dissolution areas. In the case of concrete reinforcement, there can be a presence of a protective film that surrounds the rebar called the passive layer. This passivation of the rebar minimizes the rate of the reaction and is

the product of the high alkalinity environment provided by the concrete pore solution and adequate presence of Iron Oxides. Localized crystal defects can greatly influence the integrity of the passive layer and lead to a phenomena called pitting corrosion. Further information on the mechanisms that drive the dissolution of the passive layer are discussed in following sections.

The corrosion process can be analyzed by determining the corrosion potential of a metal in a certain environment. The corrosion potential falls between the equilibrium potentials of the respective anode and cathode and is determined by the kinetics of these partial reactions. The term "corrosion cell" is used when there is a spatial separation between the anodic and cathodic sites. The distance between the anode and cathode is variable and so the corrosion rate is highly influenced by the resistivity of the electrolyte and the internal resistance which is determined by the cell geometry (Shreir 1994).

2.1.1 Corrosion Related Distress Features

The most commonly used and least controversial method for identification of corrosion in the field is the visual assessment. Due to its simplicity and widely accepted practice, the visual assessment is required of any structural evaluation and the first step when conducting a non-destructive survey. This is largely because of the strong correlation between distress features observed in the concrete material and corrosion severity. These distress features can be classified as either promotors of corrosion or as direct results of a present ongoing corrosion mechanism. Guidance on how to properly identify and classify different distress features is provided in *ACI 201.1 - Guide for Conducting a Visual Inspection of Concrete in Service.* Further insight on how major distress features relate to corrosion can be found in *ACI 224.1 – Causes, Evaluation and Repair of Cracks in Concrete Structures.*

Iron oxides and hydroxides produced by the corrosion process have a much larger volume than that of the original iron in the steel. This volumetric change creates internal stresses and is the source of the distress features associated with excessive ongoing corrosion.

2.1.1.1 Cracking

The internal stresses created by corrosion will cause internal, radial cracking at the rebar due to concrete failure in tension. Although crack initiation happens at the onset of corrosion, a critical amount of corrosion products is needed for crack propagation to the surface. It was found that after reaching the surface, a crack will rapidly reach a width of about 0.016 inches. At this point, the width will continue to increase but at a greatly reduced rate (Tran et al. 2011). Presumably this is because corrosion products will begin to penetrate into internal lateral cracks surrounding the rebar, thus reducing the internal stresses necessary for crack width propagation (Val et al. 2009). In largely anodic areas, these splitting cracks can travel in a path parallel to the rebar creating a longitudinal crack.

The concrete cover may also dictate the shape of the corrosion induced crack; it is known that a larger cover will have a high probability of inducing a 'v-shaped' crack as opposed to a 'parallel-wall' crack. The formation of a v-shaped crack is preferred to a parallel-wall crack as it will reduce corrosion rate by limiting external exposure to the rebar.

2.1.1.2 Spalling and Delamination

Functioning under the same mechanics as crack initiation and propagation, spalling and delamination occur due to rebar configuration and specific material properties. It is known that closely spaced rebar will result in the most spalling. Once corrosion initiates at neighboring rebar, the crack propagation paths have a high likelihood of crossing before reaching the surface consequently leading to a mass of material loss. Similarly, if 'broad cracks form at a plan of bars' delamination can occur (ACI 224).

2.1.1.3 Surface Deformation

Even through cracking alleviates internal stresses there is still a substantial tensile force at the concrete surface above rebar that can cause surface deformation. This becomes more self-evident as the corrosion induced surface cracks widen. Although the magnitude

of vertical deformation is low, it can lead to problems related to weathering and abrasion/erosion, resulting in a loss of concrete cover (Tran et al. 2011).

2.2 Construction Practices Leading to Corrosion

Implementing poor construction practices can be the sole reason for premature structural failure or deficiency due to corrosion. This is due to the major role that concrete cover has on protecting the reinforcement from external exposures that stimulate and rapidly increase the rate of corrosion. According to D. Breysse in *Non-Destructive Evaluation of Reinforced Concrete Structures, Volume 1*, "their rate of development is a power function of time, with an exponent of about 0.5. This means that doubling the cover, multiplies by a factor of four the time before [corrosion] initiation." Unacceptable construction practices can also lead to poor concrete quality in the bulk material which will also adversely affect service life however, the most easily identifiable problems can be easily assessed by visual assessment of the covercrete.

2.2.1 Cracking

As mentioned before, the presence of longitudinal cracks along the rebar can be detrimental. These cracks are formed by factors other than corrosion initiation and can be present immediately after construction due to settlement and shrinkage (ACI 224). After initial placement and finishing, concrete will continue to consolidate which will cause a local restraining of the plastic concrete surrounding a rebar. As the concrete continues to settle, the tensile forces above the rebar can be enough to cause a surface crack. This is more prevalent when inadequate vibrating techniques or curing regimens are implemented. Additionally, when these problems occur it is common construction practice to simply refinish the concrete which if done early enough will be acceptable but if done after prolonged cracking, will result in an internal crack leading directly to the rebar without any indication on the concrete surface.
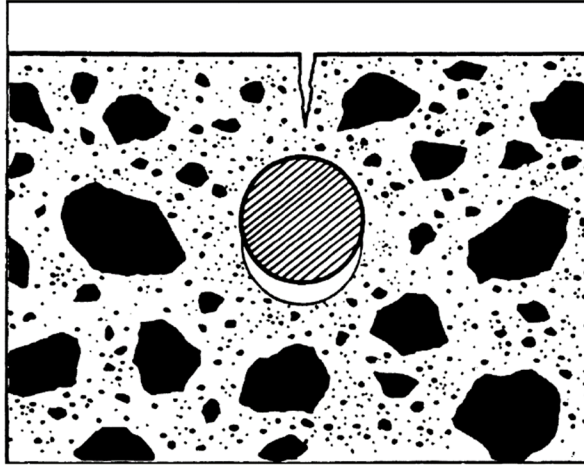
Figure 2.2: Crack formed due to obstructed settlement (ACI 224.1)

Although transverse cracks are more common, longitudinal cracks create a much bigger threat as they allow easy access of chlorides, moisture and oxygen to a large area, causing a loss of passivity along the entire rebar (Shaikh 2018). Cracks can further aid in the corrosion process without showing any signs of corrosion induced deterioration by supplying necessary oxygen to cathodic sites. This is probable because bridge decks are constructed with dense, interconnected rebar mats which provide a widespread electrical connection between anodic and cathodic sites. This means that all cracks propose a threat to long-term durability even if located in areas that are believed to be in good condition.

2.2.2 Water to Cement Ratio

As mentioned, the concrete cover is of primary importance in regards to corrosion mitigation. Recommendations for concrete mix design and cover depths regarding durability issues can be found in *ACI318 – Building Code Requirements for Structural Concrete.* A cover depth of 2 inches is required for the design of reinforced concrete structures exposed to weather. Additionally, structures exposed to deicing salts would be classified as "severe" exposure class for corrosion and a maximum w/cm ratio of 0.40 is instated by ACI318. This limitation is in place to ensure that enough hydration products form to decrease porosity and increase the difficulty for fluids to move through the concrete. One of the foremost harmful construction practices is that of adding water in

order to increase workability. This increase in w/cm ratio can exceed beyond the mixture requirements and ultimately lead to an early onset of corrosion.

2.3 In-Service Exposures Leading to Corrosion

The rate at which steel corrodes in a purely atmospheric condition is low and relatively homogeneous, but exposure conditions when implemented in concrete can rapidly increase corrosion rate and promote localized corrosion. These exposure conditions are chloride exposure and carbonation. Both mechanisms rely on diffusion through the concrete to reach reinforcement and are therefore determined by the volume fraction, tortuosity and connectivity of the pores. Pore interconnectivity and tortuosity are dictated by the amount of hydration products present and thus are mostly influenced by water/cement ratio (w/cm), inclusion of supplementary cementitious materials (SCM), degree of hydration and cement type (Breysse 2010). Ultimately, this means that the concrete cover quality and saturation content are the primary factors driving these durability mechanisms.

2.3.1 Chloride Exposure

Bridge decks in particular are highly exposed to chloride ions through the diffusion of de-icing salts heavily implemented in winter months. Although it is unclear why, it is believed that the chlorides disrupt the passive layer of the steel by reducing the pore solution pH and serving as a catalyst for oxidation (Breysse 2010). Several methods exist to analyze the extent of chloride induced corrosion such as chloride depth profiling in the field and laboratory testing for chloride content. Although commonly used, corrosion determination by chloride content alone can be misleading due to variations caused by the capability of the chlorides to bind to the hardened paste. In addition to this, chloride induced corrosion is also a function of the chloride threshold level which is determined by the concentration of hydroxyl ions in the pore solution surrounding the reinforcement. These reasons demonstrate the complexities to using chloride content to assess corrosion and provide a reliable service life estimation (Beddoe 2010).

2.3.2 Carbonation

Alkalis in the pore solution of concrete will react with carbon dioxide, in a process referred to as carbonation. This reaction dissolves carbon dioxide to form carbonic acid, H_2CO_3, which reacts with hydration product $Ca(OH)_2$ which produces calcium carbonate, $CaCO_3$. The primary reaction is shown below:

$$Ca(OH)_2 + H_2CO_3 \rightarrow CaCO_3 + 2H_2O$$
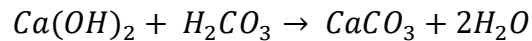
The result of these reactions occurring is a reduced pH in the pore solution, and thus an unfavorable environment for the passive layer of steel (see section 2.5.1) (Malhotra and Carino 2004).

2.4 Corrosion Mitigation Practices

2.4.1 Silane Treatment of Concrete Surface

A favorable method for mitigating chloride penetration into the concrete surface is by the means of applying a hydrophobic treatment to the surface. The penetration of chlorides into the concrete is determined by the pore structure and capillary forces that are created on the surface. Hydrophobic agents such as silicones behave in a way that weaken the molecular attraction between water and concrete, thus repelling water molecules from entering the concrete pores. It has been found that hydrophobic treatment can reduce the water absorption of concrete by 70 to 90%. The effect that this has on chloride penetration specifically is a reduction of penetration depth by a factor of 5 to 6 (Vries 1997).

2.4.2 Implementation of Overlay Material

The application of an overlay has become a general solution to the deterioration mechanisms induced at a critical corrosion level. Overlays are used to extend the service life of a concrete bridge deck by forming a barrier between the existing material and the external factors that cause corrosion or further physical concrete deterioration. The

inclusion of an overlay may not prevent future deterioration if the underlying bulk material still provides a corrosive environment for the reinforcement (Meng et al. 2020).

2.5 Corrosion Performance of Rebar

Observing long-standing concrete structures built during the time of the roman empire, reveals the potential for concrete longevity. With the inclusion of steel in modern day structures, this is unobtainable and instead "their service life is limited precisely because of the corrosion of reinforcement" (Bertolini et al. 2004). Current design standards place a service life of 50 years on most structures, with the primary form of protection being that of the concrete quality. Under temperate exposure conditions, a structure should be able to meet the required design service life so long as great care is taken to abide by the standards in regards to choosing concrete materials, mixture composition, placement, compaction and curing techniques. Even these structures that have ideal exposure conditions may be unable to meet the 50-year service life if the concrete has been inadequately prepared or placed. This means that structures exposed to highly aggressive environments have an even higher likelihood of corrosion long before 50 years has elapsed. It is because of this that great lengths have been taken to better understand the impact that reinforcement type has on deterring corrosion. Many coatings and corrosion resistant reinforcement options have been studied but presently, epoxy coated reinforcement is the preferred method in this region.

2.5.1 Standard Black Rebar

Corrosion of ordinary steel is inevitable under atmospheric conditions. This is because of the instability of iron as an alloy and the inclination for it to revert to a more stable state in the form of iron oxide (Malhotra and Carino 2004). Exposure to atmospheric oxygen is enough for this chemical reaction to occur and exposure to water increases the reaction rate rapidly. In the case of black rebar, the only form of protection from environmental exposure is the concrete cover and the passive layer (see section 2.1). The passive layer behaves as a barrier between the iron in the steel and atmospheric oxygen to prevent the formation of iron oxides, however it is known to be brittle and easily compromised.

Carbonation and chloride exposure are the primary durability mechanisms that aid in corrosion, due to the breakdown of the passive layer.

Black reinforcement in bridge decks is extremely susceptible to large macro-cells through wire tied connections between the top and bottom rebar mats. Exposure to chlorides from the surface will create anodic sites in the top mat while exposure to carbon dioxide will create large cathodic sites in the bottom mat (Breysse 2010).
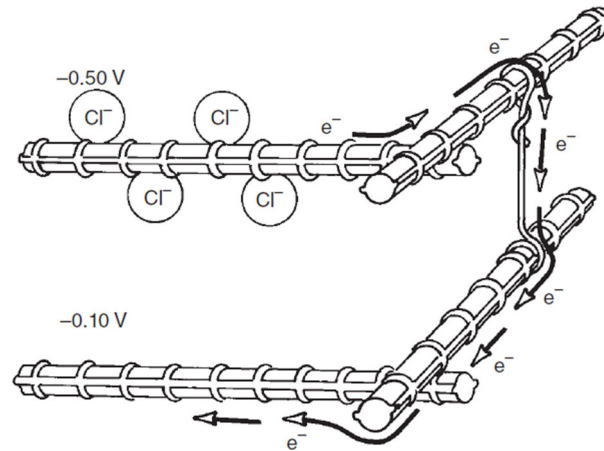
Figure 2.3: Differences in Chloride Ion Concentration Establish Formation of Macro-Cell

2.5.2 Epoxy-Coated Rebar

Epoxy-coated rebar (ECR) has been among the primary methods for corrosion resistance in North America since its development in the 1970's. The epoxy coating acts as a protective barrier around the rebar that inhibits corrosion in carbonated concrete or chloride rich environments. However, concerns about its effectiveness in very aggressive exposure conditions have been brought to light after several independent studies have reported negative experiences when studying the rebar in-service.

2.5.2.1 Protection Mechanisms

Two theories exist to describe the mechanisms which protect the reinforcement: physical barrier and electrochemical barrier theories. The first of these simply implies that

corrosion is controlled by the presence of a physical layer between the metal substrate and the aqueous corrosive environment. This dielectric layer is impervious to charged chloride ions and thus should prevent any contact between the rebar and harmful external elements, but its protection is limited due to its permeability in regards to water and oxygen. The second of these pertains to the increase in resistivity at the rebar surface due to the coating material. The increased resistance limits the electrical flow of ions between the cathodic and anodic sites along the rebar thus reducing the reaction rate (Oudar and Marcus 1995).

2.5.2.2 Failure Mechanisms

Failure mechanism, in this case, refers to the formation of an active corrosion cell despite the application of an epoxy coating on the rebar. There exist two explanations as to why this may happen in concrete reinforcement: underfilm corrosion due to water penetration and debonding due to blistering and cathodic delamination.

As mentioned above, the epoxy layer is permeable to water by some degree which can penetrate the protective coating and create an electrochemical layer at the rebar surface. The degree of permeability relies heavily on the permeability coefficient which is determined by the epoxy material characteristics. However, the driving forces that influence permeation susceptibility are areas with high moisture gradients, areas with high amounts of impurities and areas with high capillary forces. The most prevalent of these being the presence of moisture gradients which can be induced through exposure to wetting/drying cycles and very humid environments, resulting in diffusion through the polymer. Once water and oxygen reach the rebar surface, corrosion initiation can occur under the presence of a cathodic reaction (Oudar and Marcus 1995).

Debonding is the general term used to describe the loss of adhesion between the epoxy coating and substrate and can be initiated once the water layer separates the coating from the rebar. This adhesion loss can be caused by either chemical disbondment through molecular interactions between the polymer and metal or mechanical/hydrodynamic disbondment by an increase in osmotic pressures under the coating. The result of this is a relatively uniform debonding of the epoxy coating.

There is also the case of a localized cathodic delamination due to defects within the coating; this is usually referred to as pitting corrosion. The presence of a defect in the coating means that a small area of the rebar is more exposed to the corrosive environment and will have an earlier onset of corrosion than the surrounding areas. Once corrosion products have formed at the defected area, permeation of oxygen is no longer possible which will result in a large anodic area underneath the defect while cathodic sites are pushed away to locations where oxygen can still permeate the coating; this in essence is the formation of a "blister." The limited ionic transport between anodic and cathodic sites due to the epoxy coating results in the propagation of corrosion products laterally at the edges of the blister. This lateral progression along with the high pH environment of concrete will cause local debonding and an area of accelerated corrosion (Oudar and Marcus 1995).
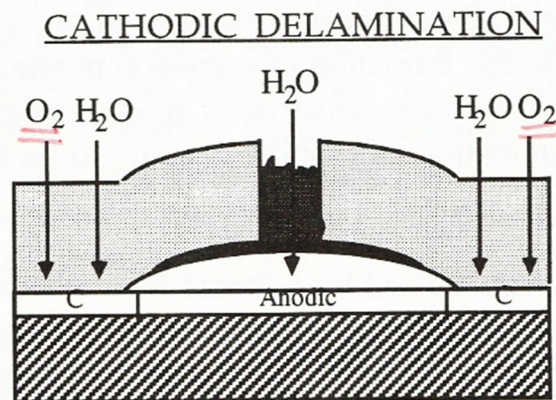
Figure 2.4: Blister Initiation and Propagation Due to Cathodic Delamination

2.6 Current Practices for Field Assessment of Corrosion

Due to the inherent seriousness of corrosion, much investigation and research has been tasked with optimizing the design, inspection and repair of those structures most at risk. Assessment of corrosion in the field has proven to be an extremely delicate task as it is usually the determining factor for demolition. To determine the true extent of corrosion, destructive testing is necessary which on a large structure can be costly and naturally undesirable as it will be more harmful to the structure and those using it. To avoid this,

extensive research has been performed to better understand the extent to which nondestructive testing can be used in the field to assess corrosion. The general consensus among industry professionals is that a combination of tests should be used synonymously and so began the search for the most efficient, yet reliable testing program. Commonly used methods of corrosion assessment include visual inspection, delamination survey, chloride content measurement, concrete resistivity survey, concrete cover-depth survey, carbonation profile determination, corrosion potential and rate of corrosion measurement (Broomfield 1994).

Most commonly used inspection strategies employ the various levels of visual inspections in addition to collection of non-destructive properties. The preliminary stages of assessment include mapping of deterioration, concrete cover depth mapping, and potential mapping when in the case of chloride induced corrosion. This level of information is accepted as adequate for determining critical areas (Raupach et al. 2013). Further investigation can be conducted in critical and non-critical areas with the addition of destructive testing for mechanical properties. These results are then calibrated for interpretation of the entire structure.

The determination of structural integrity on the premises of NDT is difficult, despite the theoretical premise that each test is directly related to a mechanical property, because real structures are never exactly similar to the materials which were used for data collection. The combined use of multiple nondestructive methods is helpful, as each test is sensitive to some physical property. The true skill of the engineer lies in the ability to "uncouple effects between influence of the real material properties and those of other parameters" (Breysse et al. 2008).

2.7 Nondestructive Evaluation of Structures Affected by Corrosion

2.7.1 Half-Cell Potential Testing

The half-cell potential test is an electrochemical test that has become a staple for assessing corrosion in the field. The corrosion potential of reinforcement is determined by variances at different locations on the rebar when compared to a reference electrode

with a standard half-cell potential for oxidation. Commonly used reference electrodes are copper/copper sulfate ($Cu/CuSO_4$) and silver/silver chloride ($Ag/AgCl$).

2.7.1.1 Electrical Potential

The term 'half-cell' is used to refer to the independent reactions that occur at the anode and cathode within an electrolytic cell. These reactions which govern the rate at which the anode and cathode release electrons and enter solution as positive ions, is called 'half-cell potential.' Replacing the external circuit required of an electrolytic cell with a voltmeter will create an 'open-circuit condition' and calculate the difference between the anodic and cathodic half-cell potentials. The result of this is a measurement in volts which indicates the direction of electron flow as well as the magnitude. The magnitude in volts gives an indication of possibility for corrosion because it displays how readily the material will give up electrons, which is the first step of the corrosion reaction.
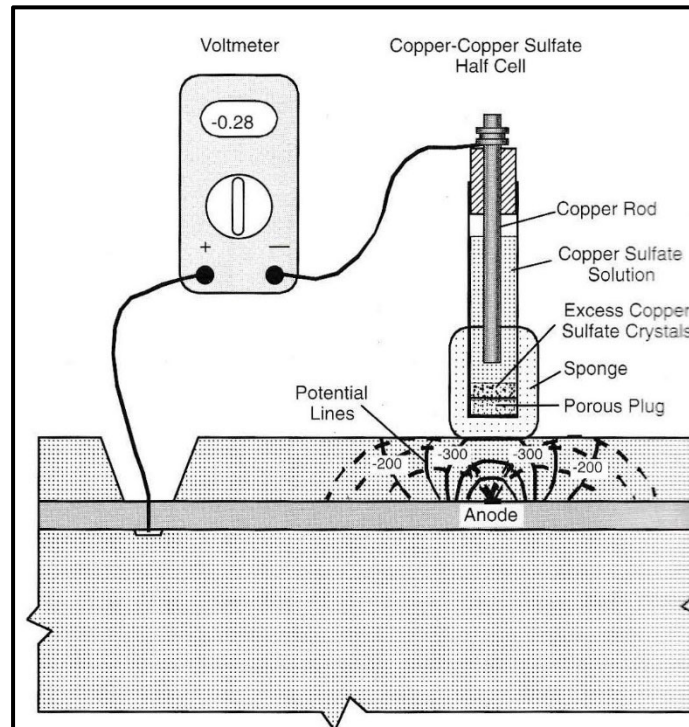
Figure 2.5: Half-Cell Potential Test Schematic

2.7.1.2 Data Interpretation

Two methods of data interpretation are recommended by ASTM C876, (1) the numeric technique and (2) the potential difference technique. The numeric technique is more commonly known and offers less variability for interpretation by assigning a 'probability' of corrosion for observed potential measurements. These recommendations come from testing of controlled, laboratory samples and so this technique should not be used in situations where carbonation extends to the level of reinforcement or concrete is exposed to variable moisture and oxygen content.
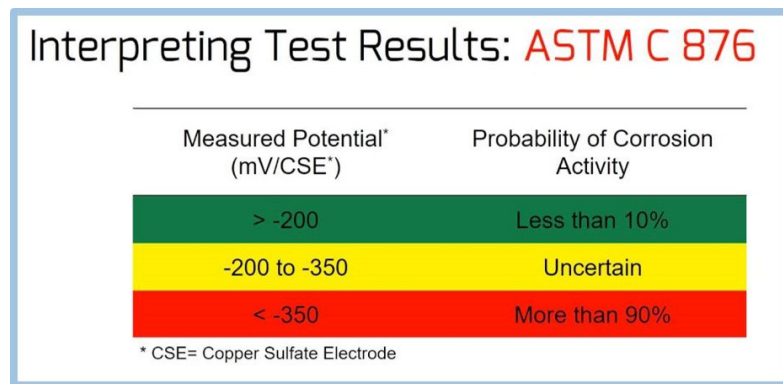
Figure 2.6: Half-Cell Potential Interpretation According to ASTM C876

Although it is not recommended to use the limits defined in figure 2.6 for most structures, it is possible to draw conclusions regarding the magnitude of potential for a given structure after verifying the state of corrosion and relating it back to previously obtained data. This has been conducted in multiple studies which after collecting half-cell data, verified the findings with the loss of cross-sectional area of reinforcement. Following this method, multiple studies have observed a correlation between loss of cross-sectional area when potential values are lower than -450 mV in dry conditions (Yodsudjai and Pattarakittam 2017).

The potential difference technique is advised in most cases, providing a knowledgeable and experienced engineer is able to interpret the data. This method provides no insight regarding the magnitude of potential and instead calls for identification of active corrosion areas through inspection of potential gradients.

2.7.1.3 Factors Affecting Half Cell

In reinforced concrete, the half-cell potential cannot be measured directly at the steel surface due to the presence of concrete cover. Because of this, the composition and depth of concrete cover will greatly influence observed half-cell potential measurements as it can induce a significant ohmic potential drop (IR). "The potential difference between the position above the anode and a distant cathode become smaller with increasing cover depth – thus the location of a small corroding spot becomes more difficult with high cover depth" (Elsener and Bohni 1997). Additionally, a dense concrete cover can limit the oxygen diffusion process resulting in a low oxygen content at the rebar-concrete interface, shifting the potential to a more negative value.
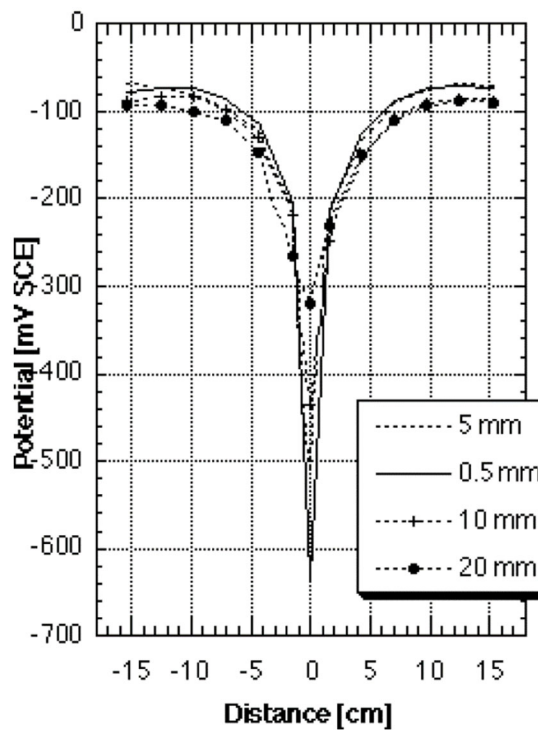
Figure 2.7: Influence of Cover Depth on Half Cell Potentials (Elsener and Bohni 1997)

It has been found that variations in concrete pore solution pH will induce changes in potential as passive steel will behave as an oxygen electrode. In the case of heavily

18

carbonated concrete, this means that the potentials will be more positive (Elsener et al. 2003).

Additionally, concrete moisture heavily influences the resistivity of the concrete cover, so a more saturated concrete will enable more electrical flow resulting in more negative half-cell potentials. Saturation content should not affect the potential gradients and therefore should not inhibit the detection of anodic spots, so long as moisture distribution is uniform. Despite this, a completely dry concrete may hinder the detection of corroded rebar altogether. Similarly, it is known that the external temperature also results in a change of half-cell due to the change in diffusion rates of local O_2 and an increase in moisture. This will result in an accelerated transportation between the cathode and anode also decreasing the observed corrosion potential (Zou 2016).

Due to the electrochemical nature of the half-cell test, concrete resistivity heavily influences the potential measurements. It has been seen that the relationship between concrete resistivity and potential is more prominent in seriously deteriorated concrete. One such study found that the potential drastically increased when resistivity values were below 4 kΩcm (Sadowski 2013).

It is known that the theoretical basis of half-cell potential is not supported for reinforcement types like epoxy-coated and galvanized rebar. In the case of epoxy-coated rebar, the coating does not allow for a sufficient electrical connection. An accurate potential reading may not be feasible, but the presence of coating defects or unprotected rebar ends may allow for a stable reading that can then be interpreted by an experienced, corrosion specialist (Gu and Beaudoin 1998).

2.7.2 Surface Resistivity Testing

Resistivity is defined as a measure of the resisting power of a specified material to the flow of an electric current. In concrete, this is governed by the pore microstructure and condition of such. Concrete resistivity and electrode potential go hand in hand in determining the state of corrosion of steel in concrete. As stated above, the electrode potential determines if a reaction is possible and thus is the thermodynamic factor of

corrosion. The concrete resistivity and availability of oxygen, on the other hand, are the kinetic factors and thus determine the rate at which the reaction can occur (Carino 1999).

Surface resistivity is a method first suggested by Robertshaw and Brown; surface resistivity is calculated by measuring the potential drop between two inner electrodes when a current is sent between two outer electrodes. This test differs from the widely used, two point (bulk resistivity) test as the electrical current travels parallel to the concrete surface as opposed to through the material axis. It is commonly used in field-assessments since access is limited to one side for testing and therefore is completely non-destructive.

2.7.2.1 Factors Affecting Resistivity

It is known that as temperature increases the resistivity of an electrolyte decreases. Because of this, it is expected that the same would occur in moist paste, mortar and concrete (Malhotra and Carino 2004). Similarly, resistivity is heavily influenced by moisture content and saturation conditions as the availability of water in pores will greatly increase the conductivity and accelerate ionic movement.

The presence of cracks will also influence the resistivity measurement since it alters the transport properties by reducing the availability of paths for ionic flow. This means that a reduction of resistivity may be an indication of internal cracking on the microstructure level (Layssi 2015).

2.7.3 Surface Hardness Testing

Often referred to as rebound testing, the surface hardness test, gives some indication of the material stiffness of the surface layer. The equipment utilizes a spring and hammer mass to impact the concrete and measure the distance travelled after it has rebounded off the surface. This means that the test is analyzing the material stiffness by measuring the conversion of potential energy into kinetic energy of a spring. Furthermore, research was conducted to study the stress waves created by this impact and it was found that the rebound number is approximately proportional to these waves. Upon impact, there is

generated a compressive wave and a reflected wave, which were both found to depend upon the material stiffness (Akashi and Amasaki 1984).

The rebound hammer has shown to be a highly sensitive test regarding a plethora of factors including surface condition, coarse aggregate type, moisture condition and carbonation penetration among many others (Malhotra and Carino 2004). Research has revealed that the effect of moisture can greatly impact rebound results. Concrete older than three years was shown to differ by 10-12 rebound units when comparing wet samples and laboratory-dry samples (Zoldners 1957).

Since this test is reliant on the surface condition of the concrete, the results will be drastically impacted by the products of carbonation. This is especially true for old concrete, which can have carbonation depths which exceed that of the stress waves created by the rebound impact. It has been found that in severe cases, the rebound data can experience a 50% increase compared to uncarbonated concrete (Kolek 1969).

2.7.4 Ultrasonic Testing

2.7.4.1 Wave Propagation Theory

There are three types of waves that are the resultants of a disruption within a solid material: compression waves (P-waves), shear waves (S-waves) and Raleigh surface waves (R-waves). These waves are named according to the direction of particle motion in relation to the sound wave path. Compression waves are defined as particle motion that is parallel to the wave path, shear waves are defined by particle motion that is perpendicular to the wave path and surface waves are defined as particles that move an in elliptical pattern along the contour of the surface, with the elliptical axis perpendicular to the wave path (Hellier 2001). In an infinite, elastic material the velocity of compression waves is determined by the material Elastic Modulus (E), Poisson's Ratio (v) and the material density (ρ).

At the interface of different materials, a change in wave velocity will occur due to the change in material characteristics, resulting in a reflection of a portion of the sound wave.

The determination of how much energy is reflected is called 'acoustic impendence' and is governed by density and elasticity. When a stress wave encounters a change in impedance, a portion of the wave is reflected back towards the source of impulse. This means that a change of impedance indicates the location where the material changes density, modulus, or area; all of which are associated to material and structural integrity.

The terms reflection and refraction are used to describe the mechanism that occurs as a P-wave or S-wave front encounter an acoustic impendence change. Similar to light rays, a portion of the original stress wave will be reflected back at an angle of incidence relative to the boundary plane while a portion will be refracted through the underlying material.

2.7.4.2 Ultrasonic Pulse Velocity

Ultrasonic pulse velocity (UPV) is a test that analyzes the compression wave in order to derive understanding of the material integrity. The equation that describes this relationship is shown below:

$$Cp = \sqrt{\frac{E(1-v)}{\rho(1+v)(1-2v)}} \qquad \text{.... Eq. 1}$$

where,

      C_p: Compression wave velocity

      v: Poisson's ratio

      E: Modulus of Elasticity

      ρ: Density

The standard test device will have a transducer which will emit the ultrasonic pulse and a receiver which will sense the arrival time of the wave once it passes through the material. This method is most appropriate for identifying low quality concrete in a relative assessment because deviations will be the result of heterogeneous areas including cracking, deterioration, honeycombing and changes in mixture proportions.

One of the primary factors which will affect UPV results is the type and amount of aggregate in the concrete. Research indicates that rounded aggregate produces the lowest velocity, while crushed limestone produces the highest. It has also been observed that for concrete within the same strength level, the pulse velocity will increase with an increase in coarse aggregate content (Jones 1954).

In addition to this, UPV can also be effected by temperature, moisture condition and presence of reinforcement. Research has shown the influence of temperature is negligible when in a range of 41 and 86 degrees Fahrenheit and correction factors have been calculated to account for data collected outside of this range (Jones and Facaoaru 1969). Pulse velocity will increase in a saturated environment as compared to an air dry environment. Because of this, the influence of moisture is related to the porosity of the concrete meaning that older and high-strength concrete will be less influenced by moisture due to the increased formation of hydration products.

The presence of steel reinforcement is highly influential on pulse velocity, as it provides a much stiffer and denser material for the wave to pass through, subsequently the results are anywhere from 1.4 to 1.7 times that of plain concrete (Malhotra and Carino 2004). Unlike other parameters, the reinforcement layout can be easily known and so research has been conducted to account for changes in UPV based on different rebar configurations during testing. It is thanks to this research that UPV can be performed on almost any reinforced concrete element and still provide a relatively accurate depiction of the pulse velocity of the concrete.

2.7.4.3 Pulse Echo

Pulse echo methods derive meaning of material properties by analysis of the reflections and refractions caused by material change boundaries. The true pulse-echo method implements a transducer that also acts as a receiver that monitors the surface response of the reflected waves. The output is called a time-domain waveform and can be used in conjunction with the material wave speed to calculate the depth at which a certain reflection occurred. This method is primarily used to identify the back wall or determine depth of a structural element, with secondary benefits being the location of large defects or changes

in material composition. More advanced methods allow for real-time analysis of these features by internally calculating the material wave speed and providing a visual aid such as a heat map for interpretation.

All parameters that influence UPV, will also have an effect on pulse echo as both tests are based on the ability of a compression wave to travel through the concrete. In addition to these, pulse echo is influenced by sample geometry. The effect of attenuation in large structures can influence detection of discontinuities at certain depths because the reflected wave is not strong enough to be received at the surface (Hellier 2001).

CHAPTER III

DESCRIPTION OF STRUCTURE

3.1 Structure Description

The structure of study is a reinforced concrete bridge deck on I-35 near Perry, Oklahoma passing over Cow Creek, NBIS #14495. The southbound lanes were constructed with black reinforcement and the northbound lanes were constructed with epoxy-coated reinforcement.

Figure 3.1: Bridge Location in Relation to Perry, Oklahoma and Surrounding Highways

3.2 Bridge Deck Specimens

During the demolition of Cow Bridge, ODOT sampled the bridge deck for further investigation. Figures 3.2 and 3.3 (courtesy of ODOT) show the panel locations in regard to the bridge deck orientation and rebar type. The highlighted areas indicate individual

sections that were carefully cut during demolition and then transported to the residency in Perry.
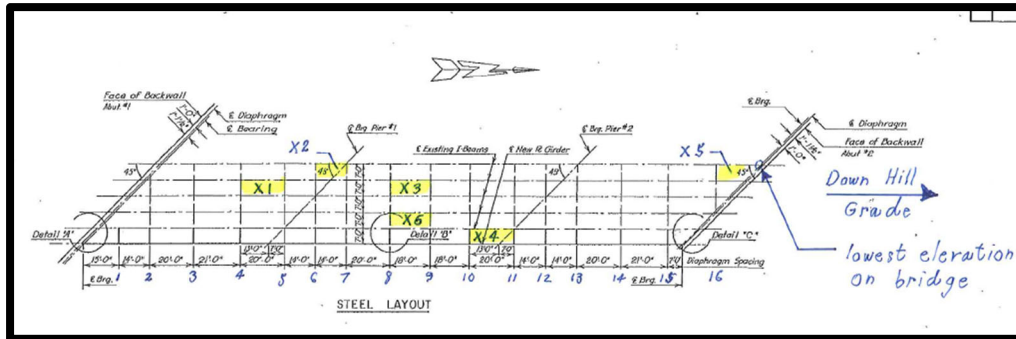
Figure 3.2: Slab Location for Epoxy Coated Rebar Slabs
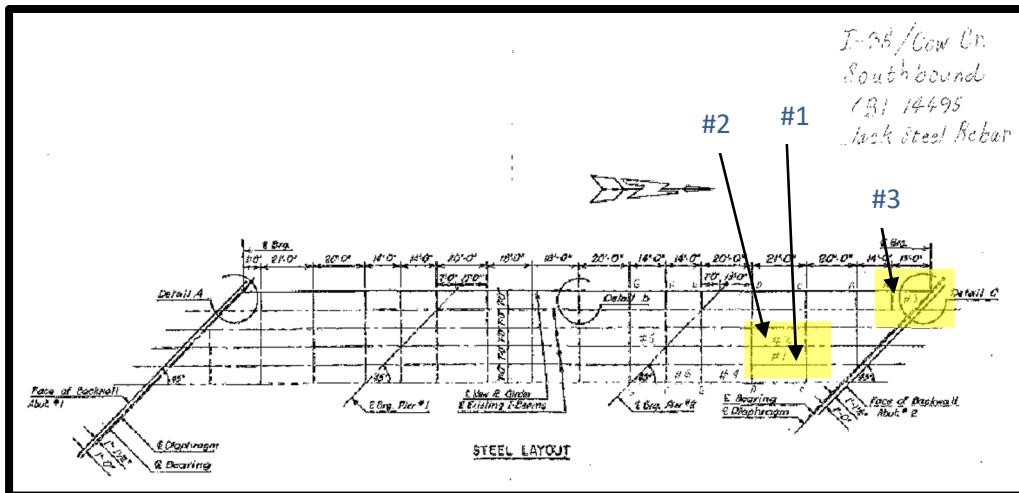
Figure 3.3: Slab Location for Black Rebar Slabs

The slabs were sawed down further at the Perry Residency to meet the load restrictions of the fork lift at Bert Cooper Lab. Thereafter, they were transported to the laboratory by ODOT staff. The slabs were stored outside for most of the time during testing, exposed to all climatic conditions. The slabs were moved and conditioned inside for at least 48 hours prior to performing any laboratory analysis that required controlled temperature conditions (approximately 73°F and 50% RH).

There are ten total slabs, four with black rebar and six with epoxy coated rebar. For the purpose of this paper, only six total slabs will be discussed. The final dimensions and

naming convention for each slab is shown in the table 3.1, along with the original location on the bridge deck.

Table 3.1: Slab Information

Slab Number	Bridge Deck Location	Width (ft - in)	Length (ft - in)	Depth (in)	Rebar Type
1	X1	5'- 8"	8 '- 1"	8"	ECR
3	#3	5' – 0" & 11"	10' – 0" & 5' – 10"	9"	Black
4	X2	5' – 4"	7' – 9"	8.5"	ECR
6	#1	5' – 2"	7' – 2"	8"	Black
7	#2	5' – 2"	9' – 1"	8"	Black
9	X3	5' – 4"	7' – 3"	9"	ECR

For testing purposes, a one-foot by one-foot grid was mapped out on the surface at each slab. An alphanumeric naming convention was used to identify each individual box, with letters differentiating boxes in the longitudinal direction and numbers differentiating boxes in the lateral direction. Each slab was given a new 'slab number' and a unique set of letters for the grid naming convention.

Figure 3.4: Slabs Outdoor Storage at Bert Cooper Engineering Lab

CHAPTER IV

EXPERIMENTAL METHODOLOGY

4.1 Visual Condition Survey

A visual condition survey was completed for each slab while referencing ACI 364.1, *Evaluation of Concrete Structures Before Rehabilitation,* and ACI 201.1R-08, *Guide for Conducting a Visual Inspection of Concrete in Service.* ACI 201.1 provides industry standards for distress feature terminology and classification of severity as well as recommendations for reporting. ACI 364.1 provides different methodologies for sampling and material testing of large structures. Many of the sampling methods mentioned in the proceeding sections come from these guides.

For this research, identifying and classifying distress features directly related to poor construction practices or an ongoing corrosion mechanism was most crucial. Primary distress features include transverse cracks, spalls, severe scaling, bug holes and shrinkage cracking. These features were mapped by using chalk on the concrete surface, paired with an aerial photo which was then imported into software and made to the proper scale.

4.1.1 Test Grid and Nomenclature

For the purpose of this research, the implementation of an alphanumeric grid system was used for each slab. The alphanumeric system used is independent for each slab in order to easily identify exact locations during analysis. Letters indicated areas in the transverse direction while numbers indicated locations in the longitudinal direction. The grid was

determined to be set at 1 ft intervals in both directions in order to create 1 ft^2 boxes for ASTM standardized testing. The nomenclature for each slab used in this study is shown in table 4.1 and an example is shown in figure 4.1.

Table 4.1: Alphanumeric Grid Designation of Slabs

Slab 1 - ECR	*A - E*	*1 - 8*
Slab 3 - Black	*K - O*	*1 - 9*
Slab 4 - ECR	*P - T*	*1 - 7*
Slab 6 - Black	*Z - AD*	*1 - 7*
Slab 7 - Black	*AJ - AN*	*1 - 9*
Slab 9 - ECR	*AO - AS*	*1 - 7*
Slab 10 - Black	*AT - AX*	*1 - 7*
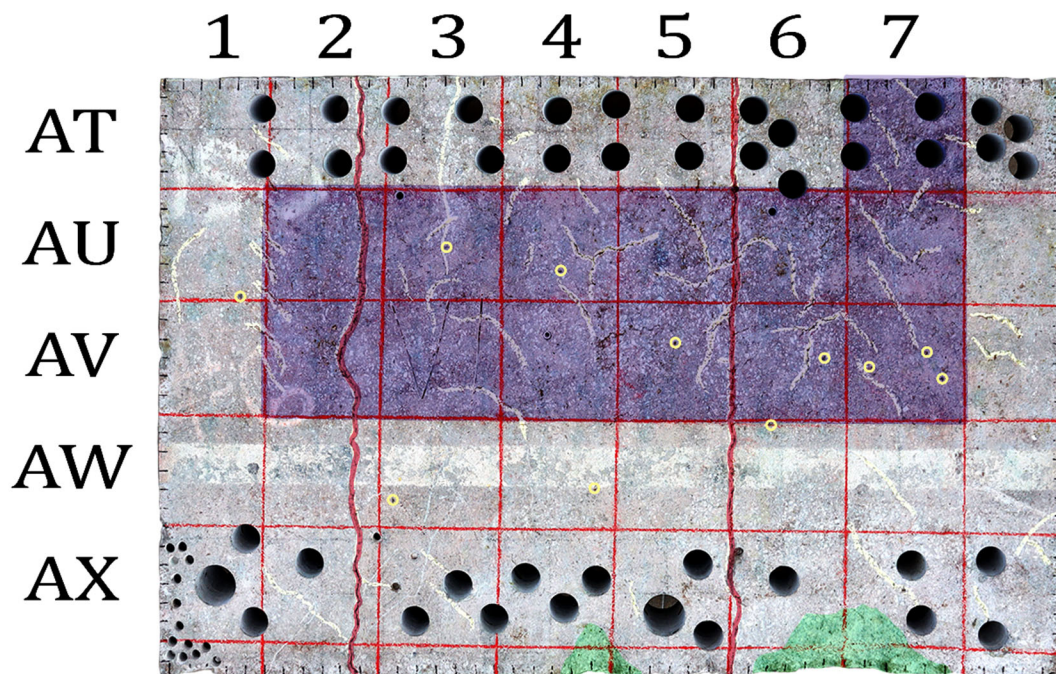
Figure 4.1: Grid Naming Convention for Slab 10

4.1.2 Crack Density

Another method of crack quantification is the 'crack density' or 'crack intensity' which has been implemented in many studies. This method is dissimilar to the commonly used 'crack frequency' by taking crack length into account. Crack density is a ratio of the total length of cracks and the surface area in question. This method can provide some indication of crack severity between different areas of the structure and allows for a consistent means of crack monitoring without any excessive field equipment. As suggested, only cracks that were visible to the unaided eye from a standing position were considered for calculation of the crack density.

Figure 4.2: Crack Mapping for Visual Condition Survey

4.2 Rebar Mapping

In order to accurately map the rebar layout a combination of methods was used. The preliminary layout was determined by measuring individual rebar sizes and rebar spacing with a tape measure. This procedure was done on every side of the slab to account for any skewed rebar placements. Ground penetrating radar and a rebar locater were then used to identify the ends of spliced rebar within the slab. The rebar configuration was then drawn

in CAD for each slab and oriented according to its unique alphanumeric system. For the purpose of this research, only the top layer of steel was considered.

4.3 Surface Hardness Survey

A surface hardness survey was completed with the Rebound Hammer in compliance with ASTM C805. 10 measurements were taken within each 1ft x 1ft box and averaged. Any data points that varied from the mean by more than six units were discarded and a new mean was calculated according to the remaining values. If any given data set had more than two values outside of this allowable variance, the entire data set was discarded and recollected.

ACI 228.1 states that to properly use surface hardness to estimate concrete strength for a structure, a correlation curve must be derived from the RN values obtained in the field and compression strengths of cores obtained from the associated areas. In order to derive this correlation, the range of RN values for a given slab was calculated and equal intervals were determined to produce a set of six data points for the curve. At each of these data points, a minimum of three cores were taken to collect compression strength.

4.4 Pulse-Echo Survey

A pulse-echo survey was completed for the entirety of each slab surface. The equipment used for this survey was the Proceq-Pundit 250 Array, which provides real-time B-scan tomography by combining 28 individual A-scans instantaneously. The b-scan provides a cross-sectional image perpendicular to the concrete surface along the length of the scan pass, which is incredibly useful for identification of inhomogeneous areas.

B-scans were collected in the longitudinal direction of each slab in the direction of increasing grid numbers. There are a total of three b-scans per longitudinal grid sections. The Pulse Velocity Estimation method uses the pulse velocities of surface signals to approximate the concrete velocity. A new velocity was estimated by averaging multiple estimates for each longitudinal grid section while ensuring that no rebar influenced the

estimate. B-scans were analyzed at different gains in order to detect smaller and larger defects or discontinuities.

4.5 Half-Cell Potential Survey

A copper/copper sulfate reference electrode was used for this project along with a single electrode wheel model for data collection.

4.5.1 Saturation Method

Saturation is the primary factor that effects concrete resistivity and therefore has a major influence on the observed half-cell potential. According to ASTM 876, two conditions exist to determine the extent of pre-wetting needed (1) value of corrosion potential does not change with time and (2) value of corrosion potential changes with time. The first condition does not require any pre-wetting to conduct the test while the second condition warrants saturation of the concrete surface until a stable reading (±20 mV) is observed for at least five minutes. In place of this method, a standard 'ponding time' was determined based on lab results achieved from multiple sample sets on the slabs in question.

The method for ponding in the lab consisted of running a continuous stream of water across the slab so that there was visibly ponded water on the concrete surface. Before half-cell potential testing, excess water was removed from the surface to achieve as close to saturated surface dry (SSD) condition as possible. This ponding procedure was implemented while half-cell tests were performed at 5, 15, 25, 45, 60, 85, 95, 110 and 140 minutes at various locations and different rebar in the slab. Tables 4.2 through 4.6 show the statistical differences between the potentials at different times for values in a 1 ft^2 area. The null hypothesis is that difference between the potential mean at time, t min, is the same as the mean potential at time 5 min.

The slab used for this testing was slab 10 and a picture of the slab surface with the naming convention used below, can be seen in figure 4.1.

It can be seen that for AU7, AU6 and AV6, that the values become significantly different at 60 minutes of ponding. Whereas in AU5 and AV3 values become significantly

different at 95 minutes of ponding. To be conservative, a minimum of 90 minutes ponding time was selected for all half-cell testing. Figure 4.3 shows the results for grid box AU6 as an example to show that at 90 minutes, the decrease in potential becomes more stable as well.

Table 4.2: Ponding Time Statistical Significance for AU7

Time(min)	15	25	45	60	85	95	110	140
p-value	0.496	0.348	0.04	0	0	0	0	0.016
Reject H_o	No	No	No	Yes	Yes	Yes	Yes	Yes

Table 4.3: Ponding Time Statistical Significance for AU6

Time(min)	15	25	45	60	85	95	110	140
p-value	0.405	0.138	0.23	0.001	0	0	0	0
Reject H_o	No	No	No	Yes	Yes	Yes	Yes	Yes

Table 4.4: Ponding Time Statistical Significance for AU5

Time(min)	15	25	45	60	85	95	110	140
p-value	0.288	0.156	0.356	0.09	0.156	0.046	0.069	0.005
Reject H_o	No	No	No	No	No	Yes	No	Yes

Table 4.5: Ponding Time Statistical Significance for AV6

Time(min)	15	25	45	60	85	95	110	140
p-value	0.206	0.2946	0.456	0.029	0.001	0	0	0
Reject H_o	No	No	No	Yes	Yes	Yes	Yes	Yes

Table 4.6: Ponding Time Statistical Significance for AV3

Time(min)	15	25	45	60	85	95	110	140
p-value	0.433	0.417	0.298	0.102	0.079	0.037	0.013	0.011
Reject H_o	No	No	No	No	No	Yes	Yes	Yes
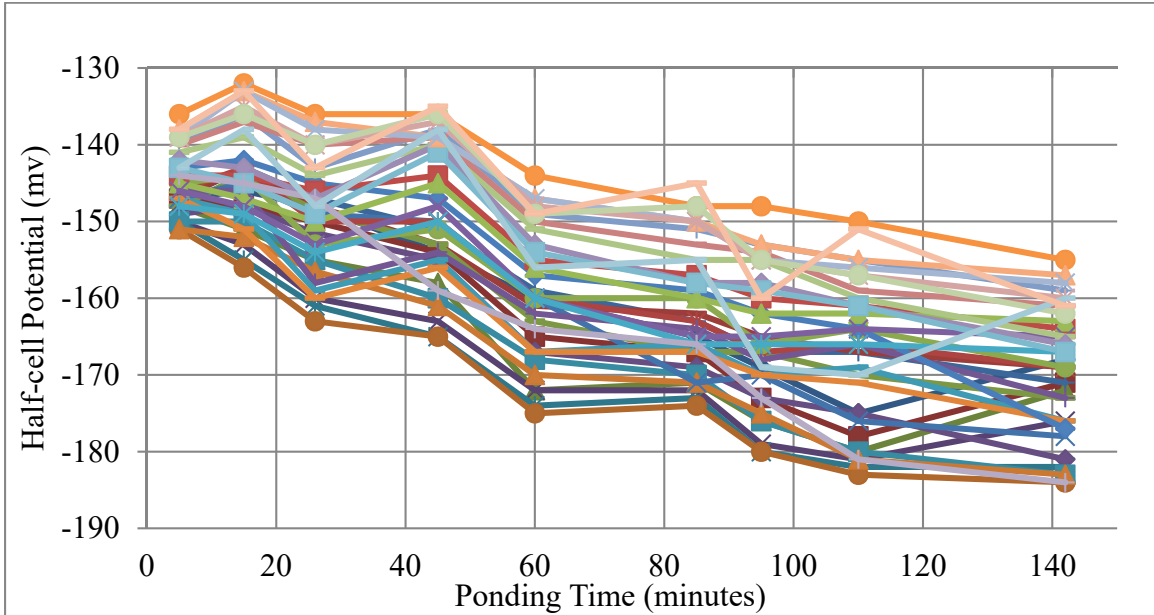
Figure 4.3: Effect of Ponding Time on Half-Cell Potential for AU6

4.5.2 Rebar Connection

In order to achieve the most representative corrosion potential map, half-cells were collected when connected to the closest rebar. In order to maintain a constant proximity, the path of data collection moved parallel to the rebar. This method was carried out for both orientations of rebar: longitudinal and transverse. Electrical connection was made by means of welding a bolt to the externally exposed rebar end and in some cases, drilling a screw into the rebar. For the purpose of this research, only top layer reinforcement was considered since the top layer is the most at risk of corrosion in a bridge deck.

Figure 4.4: Example of Rebar Connection Using Screws

4.5.3 Data Collection and Reporting

A suggested spacing of four feet is satisfactory according to ASTM 876 for large horizontal surfaces including bridge decks. In this survey, a much closer grid of 2" x 2" was used for data collection. This was proposed since the rebar spacing is limited in many areas and a clear indication of corrosion potential for each rebar was desired. Values were obtained over the entirety of the slab surface and reported in a contour map.

4.6 Compressive Strength Testing

Compressive strength was evaluated for 2.6"x5" cores in accordance to the procedure stated in ASTM C39. Cores were all conditioned in the lab for the same amount of time after being taken form the slabs outside. Both ends of each core were ground and checked for alignment in order to provide an even stress distribution under loading and provide proper friction for testing. All cores were vacuum saturated for 16 hours prior to load testing in order to meet saturation requirements. The cores were subject to a load rate of 185.83 lb/s which is within the tolerance of 35 ± 7 psi/s stated in ASTM C39. The peak load and failure type was recorded for each specimen. Compression strength can be calculated from the peak load with equation 2:

$$C = \frac{P}{A} \qquad\qquad ....\text{Eq. 2}$$

Where:

C = compression strength (psi)

P = ultimate load (lb)

A = average cross sectional area (in^2)

Figure 4.5: Compression Test Setup

Compression testing was performed on three cores sampled form the same 1ft x 1ft box at locations determined by the surface hardness survey mentioned above. Two cores were tested solely for compression while the third underwent a series of loading and unloading required for modulus testing prior to loading to failure; this method is discussed in the following subsection.

4.7 Modulus of Elasticity Testing

In accordance with ASTM C469, one core from each sample set was tested for modulus of elasticity. The third core from each sample set was to be tested for modulus by loading to 40% of the ultimate load while recording the longitudinal strain. The ultimate load was determined to be the lowest resulting value from the compression tests done from the preceding cores of the same sample set. This loading and unloading procedure was

completed a total of five times for each core tested. The first data set was disregarded in order to account for seating, while the stress-strain behavior was evaluated for the other four tests in order to calculate the modulus of the elasticity based on the load vs. strain data received.

Figure 4.6: Modulus of Elasticity Test Setup

4.8 Electrical Resistivity Testing

Bulk resistivity testing was conducted with the GIATEC RCON2 with data output in kΩ. The core is secured between two electrodes and provided an electrical collection by wet sponges. The potential drop is measured after an alternative current (AC) of 1kHz frequency is sent through the longitudinal axis from one electrode to the other. Two measurements per core were collected and averaged. Resistivity is calculated from resistance by equation 3:

$$\rho = R\frac{A}{L} \qquad \qquad ....\text{Eq. 3}$$

Where:

ρ = resistivity (kΩ*cm)

R = resistance (kΩ)

A = average cross sectional area (cm^2)

L = average length (cm)
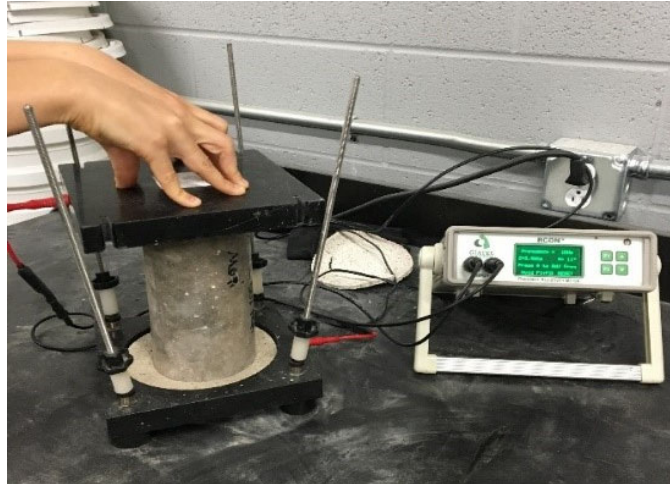
Figure 4.7: Bulk Resistivity Test Setup

4.9 Ultrasonic Pulse Velocity

UPV measurements were taken on cores using a means of direct transmission between transducers. Due to the small core size, it was optimal to use a higher frequency and so all testing was done with 120 kHz transducers. A water-based gel was used as a coupling agent between the transducers and the core ends as the pulse was sent along the longitudinal axis of the cores. Data output is recorded in µs and converted to a wave velocity using equation 4:

$$V = L/t$$ ....Eq. 4

 Where:

V = wave velocity (ft/s)

L = length between transducers (ft)

t = pulse transit time (s)
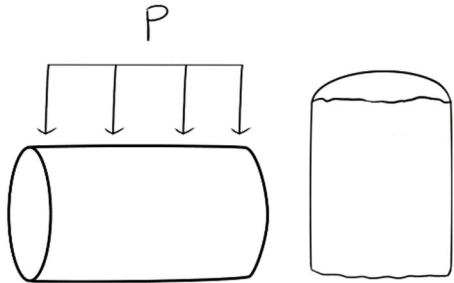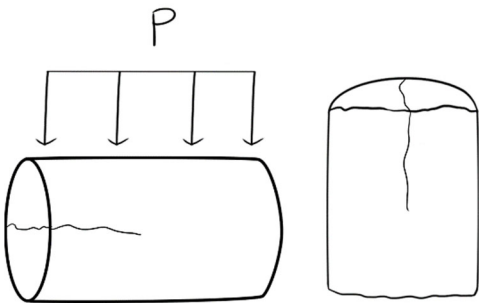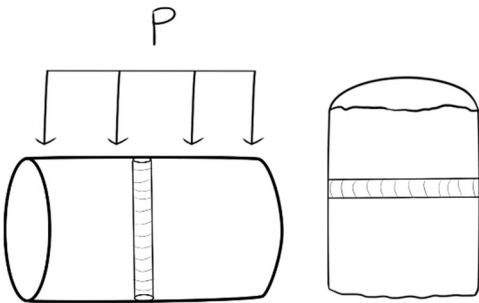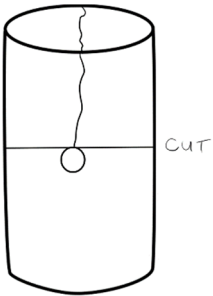
Figure 4.8: UPV Test Setup

4.10 Procedure for Colorimetric Testing of Cores

Four inch cores were collected from areas identified for stain tests including carbonation depth, chloride penetration and silane treatment depth. Coring locations were determined to deliberately include severe cracks and rebar in certain locations. Splitting tension tests were performed abiding by ASTM C496 procedures to expose the inside of the core for testing. Prior to loading, cores were secured by electrical tape at many locations along the length to ensure that the correct fracture mechanism occurred. The orientation of the desired failure plane was controlled by loading direction and is represented for each core type in table 4.7.

Table 4.7: Core Types and Procedure for Splitting Tension Test

Core Type	Procedure	Example
A No Rebar No crack	1. Split anywhere along core 2. Thymolphthalein on one half (measure at four locations) 3. Silver Nitrate on one half (measure at four locations)	
B No Rebar Crack	1. Split perpendicular to crack propagation 2. Perform procedure for Type A 3. Measure thickness of carbonation/chloride along the length of crack	
C Rebar No Crack	1. Split parallel to rebar direction 2. Perform procedure for Type A 3. Note corrosion products on rebar	
D Rebar & Crack that extends to rebar	1. Cut core at location above rebar 2. Follow procedure for Type B on top portion 3. Follow procedure for Type C on bottom portion	

4.10.1 Determination of Chloride Penetration

The method used for chloride determination was that of the application of a silver nitrate ($AgNO_3$) colorimetric indicator, commonly used in field applications. The silver nitrate concentration used was 0.1 mol/L and was applied to the freshly fractured concrete surface created by the splitting tensile test. The depth of discoloration was measured at four locations along the radial axis of the core, avoiding large aggregates. The recorded value was the mean of these four measurements.

Brown silver oxide (Ag_2) and silver hydroxide ($AgOH$) precipitates upon application but soluble white silver chloride ($AgCl$) will precipitate with the silver oxide in the presence of chloride ions. Decomposition of the silver chloride will result in a metallic, blue-grey discoloration of the concrete indicating the location of chloride contamination. It is important to note that the level of discoloration does not, at present, show any correlation with chloride content and therefore is not suitable for quantitative analysis (Beddoe 2010).

The primary limitation to this test is witnessed in the presence of carbonates because the lower pH will also result in a reaction of silver chloride to produce a discoloration. It has been observed that when the pH is below 10, determination of the chloride penetration depth becomes unreasonable (Real et al. 2015). To address this uncertainty, it is recommended for structures exposed to both chlorides and CO_2 that the carbonation depth be assessed in conjunction with chloride profiling.

Figure 4.9: Silver Nitrate Test Setup

4.10.2 Determination of Carbonation Depth

The carbonation depth for the tested samples was determined via a colorimetric method using Thymolphthalein. Traditionally a solution of phenolphthalein, coloring the concrete a shade of dark pink for a pH above 10, is recognized to be toxic to the user during its preparation from powder. It has been demonstrated to be an effective alternate to phenolphthalein (Mitchell et al. 2010). As such, a solution of Thymolphthalein was prepared and used in this investigation.

Coloration threshold for the phenolphthalein indicator is at a pH of 8.2 to 14 with a darker coloration at a pH of 10 and above. However, steel corrosion mechanisms, due to depassivation of the steel rebar, may initiate at an approximate pH of 10-11. Here, Thymolphthalein may be more appropriate colorimetric indicator of the change in pH as its threshold is 9.3 to 14 with a darker marker at a pH of 10.5. Therefore, the depth at which a detrimental change in pH occurs can be better identified with Thymolphthalein as opposed to underestimated with phenolphthalein.
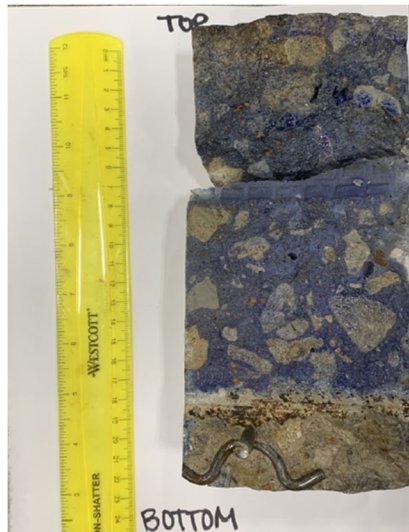
Figure 4.10: Carbonation Depth Test Setup

4.10.3 Determination of Silane Treatment

Determination of the presence of a hydrophobic agent such as silane was tested by measurement of the depth of absorption for a water based dye into the concrete surface. Proceeding testing for carbonation depth and chloride penetration depth, the cores were placed in bins containing a dark dye for 30 minutes, then removed and measured for penetration depth.

Figure 4.11: Silane Treatment Test Setup

CHAPTER V

RESULTS AND DISCUSSION

To fulfill the purpose of this research project, it was imperative that an extensive non-destructive testing regimen be performed in addition to laboratory analysis of the concrete material. The nondestructive survey included various techniques that are commonly used in the field today. The survey performed for this project, accompanied by the concrete mechanical properties will help to validate the use of a nondestructive test methodology specifically for corrosion assessment of in-service structures.

To emulate the process of corrosion assessment in the field, a NDT methodology was chosen and followed with few deviations from ASTM and ACI standards and recommendations. This survey was carried out in full, before any destructive testing was completed in order to assess the capability of purely non-destructive tests to locate active and passive corrosion areas.

Coring locations for strength estimation were selected based on sampling techniques recommended in ACI 364.1 for a surface hardness survey.

Coring locations for staining were determined based on the combination of NDT results. Six coring locations were selected for each slab:

1. High Half-Cell
2. Low Half-Cell
3. 'Poor' Area with Rebar
4. 'Poor' Area without Reba

5. 'Good' Area with Rebar
6. 'Good' Area without Rebar

In cores obtained "with rebar," it was ensured that the rebar sample taken with the core was the exact rebar associated with the qualities described in the core classification (i.e. If the transverse rebar resulted in the highest potential, then the core would have a sample of that exact rebar that produced those values).

5.1 Non-Destructive Assessment of Panel 3 - Black Rebar

5.1.1 Visual Condition Survey

As seen in Figure 5.1, 3 severe transverse cracks parallel to each other can be seen. The results of the crack index performed is 0.46. The cause of cracking cannot be determined. 23.8% of the surface area appears to have signs of surface disintegration. The latter is concentrated in two areas of the slab, K3, L-2, -3, -4 and K-7, -8, -9, L-7, -8, -9. The origin of disintegration appears to be a combination of surface scaling and erosion-abrasion as both the mortar and coarse aggregate are deteriorated. Under the combined action of vehicular loading or weathering, the weaker surface material may have scaled resulting in the apparent loss in surface material. This may have been further exacerbated overtime by the repetitive action of vehicular traffic eroding the surface of the pavement. Moreover, there are to visible spalls (K-3 and L-4) located in one of the disintegrated area. There are few air voids sparingly located. Due to disintegration within and around the void, the cause of the void cannot be determined.

5.1.2 Surface Hardness Survey

After the visual survey was conducted, a non-destructive surface hardness test was conducted using a Schmidt rebound hammer. The resulting rebound number range between 33 and 42, with a majority between 35 and 40. From figure 5.2, it can be seen that the areas exhibiting surface disintegration recorded lower rebound numbers. Meanwhile, areas recording higher rebound numbers (e.g. column 4) exhibited few distress features.

5.1.2.1 Determination of Coring Locations for Strength Estimation

In order to estimate the mechanical properties of the concrete material for this element, several cores, representative of the range in results, were taken. A total of 3 cores per location were taken for further property analysis (section 4.3). Table 5.1 provides the locations for the cores. Here, care was taken to avoid rebar in the core samples.

Table 5.1: Coring Locations for Properties Estimation – Slab 3

RN	*34*	*36*	*38*	*39*	*40*	*41*
Overlay	*K4*	*N6*	*N1*	*O6*	*M4*	*L2*
No Overlay	*N3*	*O2*	*N2*	*N4*	*N5*	*K5*

5.1.3 Half-Cell Potential Survey

A half-cell potential survey was performed on slab 3 and the results are shown in Figures 5.3 and 5.4. The recorded potentials ranged between -79 mV and -265 mV (Table 5.13). Based on figure 2.6 from ASTM C876, the probability of an ongoing corrosion is low to uncertain. Here the difference in potentials along with poles of activity may be more indicative of an ongoing corrosion cell in that location. Such is the case in the N-2, -3 region where a pole exhibits the lowest recorded potentials. It coincides with the location of both longitudinal and transverse rebar. Based on the visual survey, there are no major distress features in that area, apart from the tip of a surface crack. On the other hand, a low rebound value (34) was recorded in that region (N-3).

The cumulative probability distribution shown in figure 5.5, shows that slab 3 displayed a normal distribution of potential values making it difficult to estimate the passive and active potential thresholds. I small point of inflection can be seen in the transverse rebar and this point was used to decide the active threshold of <-170 mV and >-140 mV for passive.
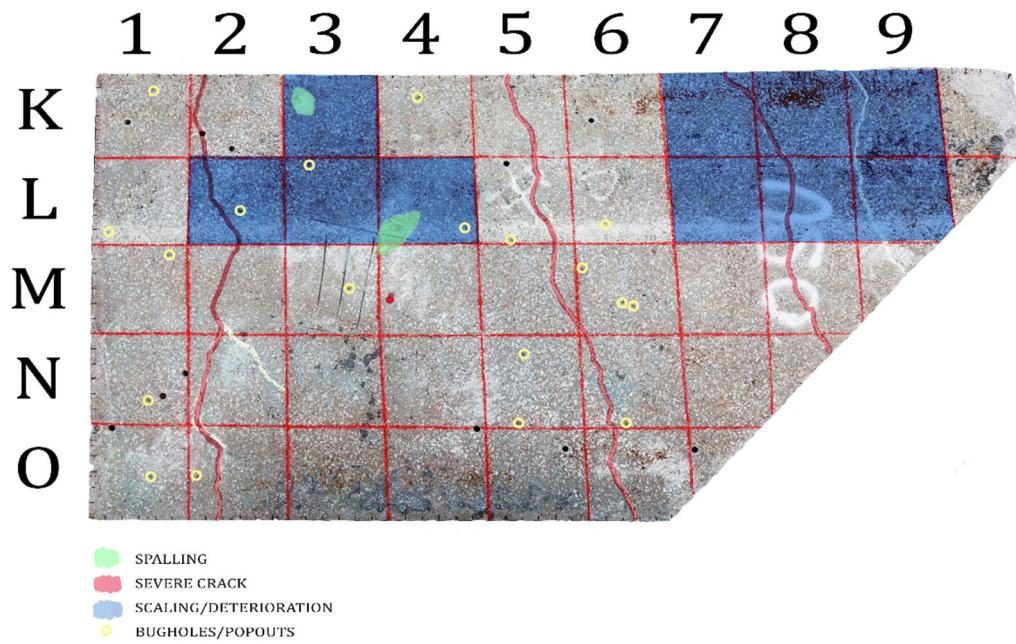
Figure 5.1: Visual Survey - Slab 3
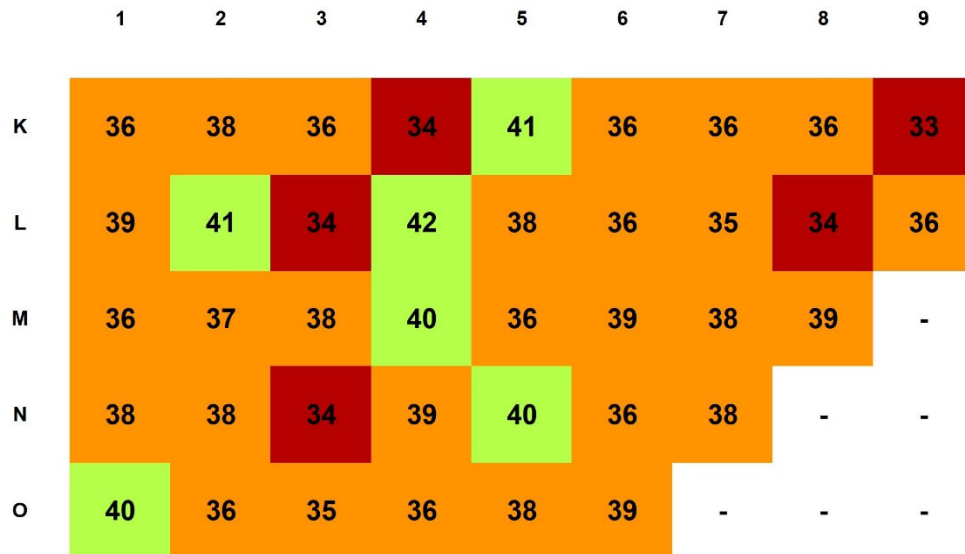
Figure 5.2: Surface Hardness Survey – Slab 3
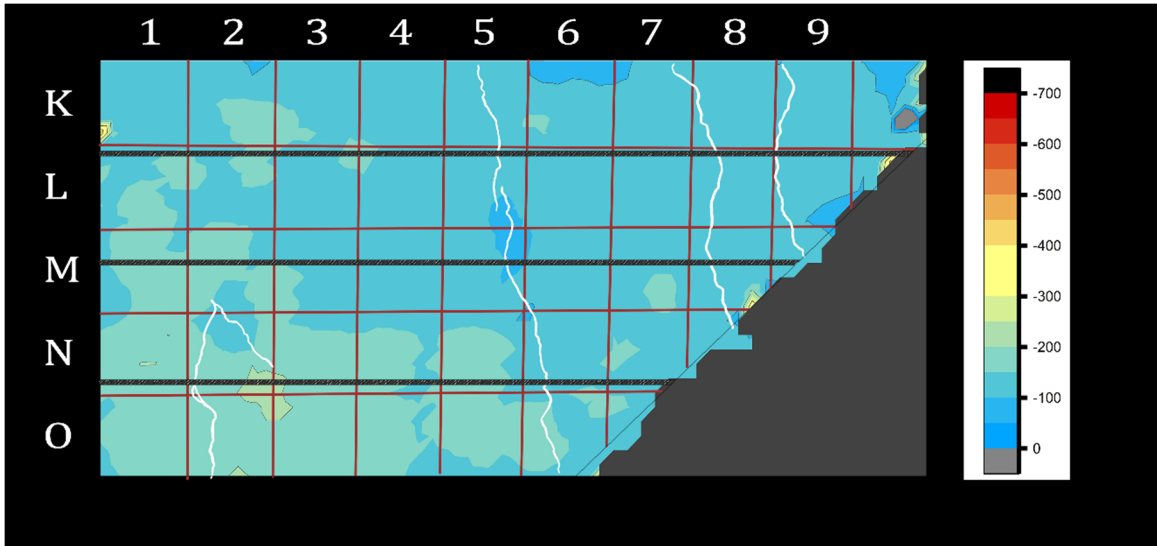
Figure 5.3: Half-Cell Potential Map for Longitudinal Rebar – Slab 3
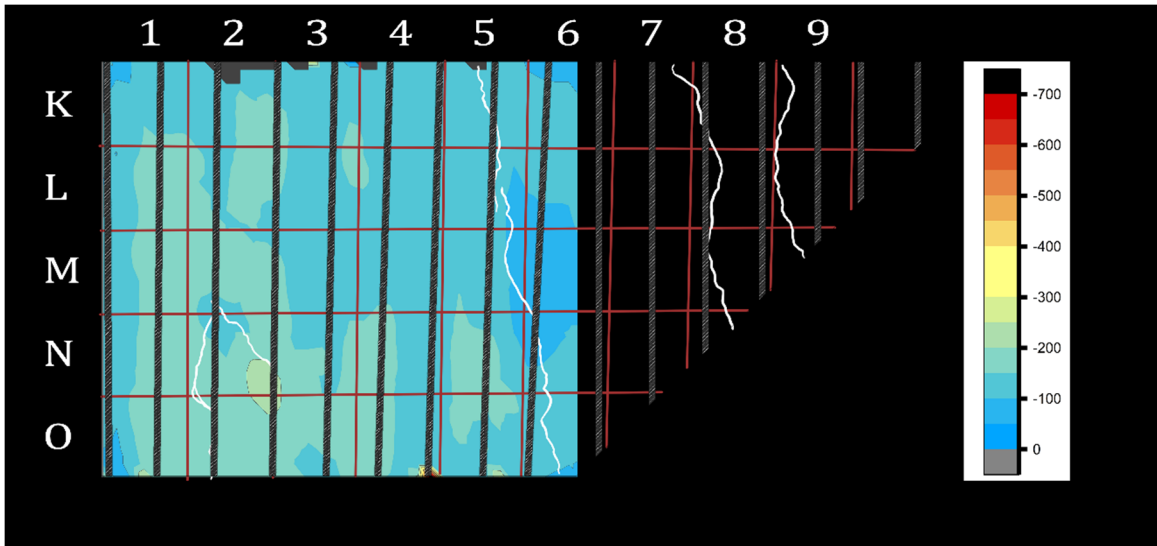
Figure 5.4: Half-Cell Potential Map for Transverse Rebar – Slab 3
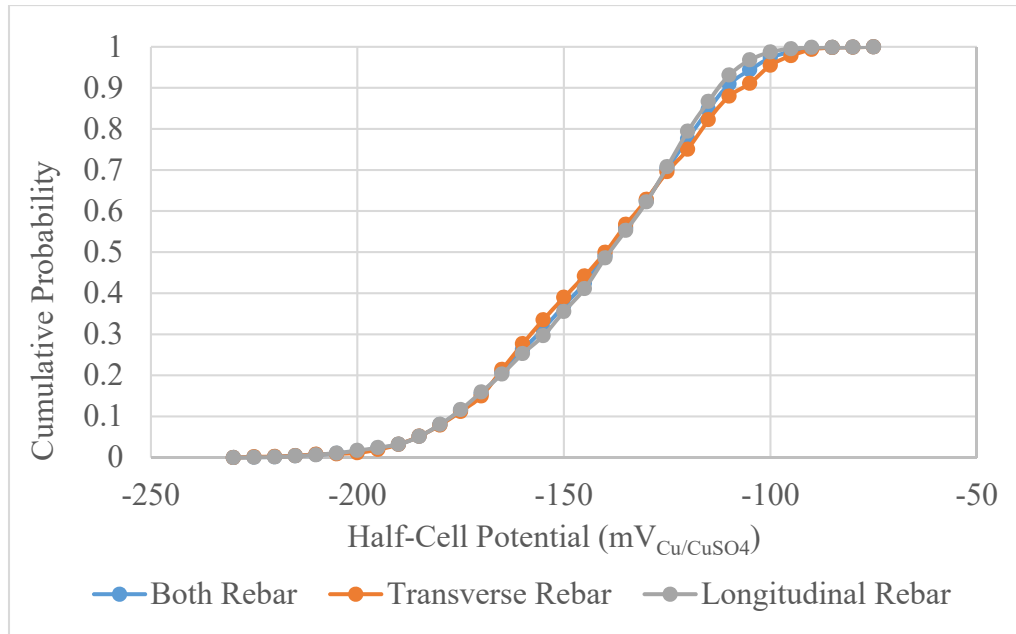
Figure 5.5: Half-Cell Probability Distribution – Slab 3

5.1.3.1 Determination of Coring Locations for Colorimetric Testing

Based on the results of the non-destructive survey, coring locations were determined to further the analysis and identify presence of chlorides and carbonation. The location of what was deemed "poor", K3 and K2 was mostly determined by the local hot-spots for half-cell potential in addition to surrounding low RN values. The identification of L8 as a 'poor' area was primarily due to the increased crack density in the area, paired with moderate scaling and a low RN value. The location of good cores, M7 and N7 had no presence of cracking or defects. A summary of core location is provided in Table 5.2.

Table 5.2: Coring Locations for Calorimetric Testing – Slab 3

Grid Box Location	Core Identification	Features/Rebar
N3/O3	High X-Cell	w/ rebar
N6/M6	Low X-Cell	w/ rebar
K3	Poor	w/ rebar
K2	Poor	None
L8	Poor	w/ rebar +crack
M7	Good	w/ rebar
N7	Good	none

5.2 Non-Destructive Assessment of Panel 6 - Black Rebar

5.2.1 Visual Condition Survey

As seen in Figure 5.6, 5 severe transverse cracks parallel to each other can be seen in addition to the formation of a 1 severe diagonal crack running between two transverse cracks. The results of the crack index performed is 0.86. The cause of cracking cannot be determined. 11.4% of the surface area appears to have signs of severe surface disintegration, located in the area Z2, AA-1, -2, -3. However, the entirety of the slab surface appeared to have minor deterioration to the point of some coarse aggregate exposure. The reasoning for this deterioration is discussed in section 5.1.1.

5.2.2 Surface Hardness Survey

After the visual survey was conducted, a non-destructive surface hardness test was conducted using a Schmidt rebound hammer. The resulting rebound number range between 30 and 41, with more values tending towards the lower range. From figure 5.7, it can be seen that the most densely cracked area resulted in the lowest rebound values as observed in AB6 and AC6.

5.2.2.1 Determination of Coring Locations for Strength Estimation

Like section 5.1.2.1, table 5.3 provides the locations of cores used for property analysis.

Table 5.3: Coring Locations for Properties Estimation – Slab 6

RN	30	32	34	37	39	41
Overlay	AC6	AA6	AD7	AA4	AD1	AD5
No Overlay	AC6	AB6	Z3	AA1	AD1	AA2

5.2.3 Pulse Echo Survey

Individual pulse echo B scans of prominence are show in figures 5.8 and 5.9. The approximated wave velocities for scan AA and AD are 7182 ft/s and 7165 ft/s respectively. This slab displayed a lot of regions with reflections that would indicate large inhomogeneous areas such as honeycombing. The excess wave reflections detracted from the back wall and rebar reflection in most areas.

5.2.4 Half-Cell Potential Survey

A half-cell potential survey was performed on slab 6 and the results are shown in Figures 5.10 and 5.11. The recorded potentials ranged between -90 mV and -294 mV (Table 5.13). Here the difference in potentials along with poles of activity may be more indicative of an ongoing corrosion cell in that location. Such is the case for box Z4 which exhibits the lowest recorded potentials for both longitudinal and transverse rebar. This local minimum is also located at the junction of both rebar and the severe diagonal crack.

The cumulative probability distribution in figure 5.12, reveals that the longitudinal rebar exhibits the expected bimodal distribution needed to determine potential thresholds. For this reason, the threshold limits were determined based on the longitudinal rebar distribution. The determined potential thresholds are shown in table 5.13.
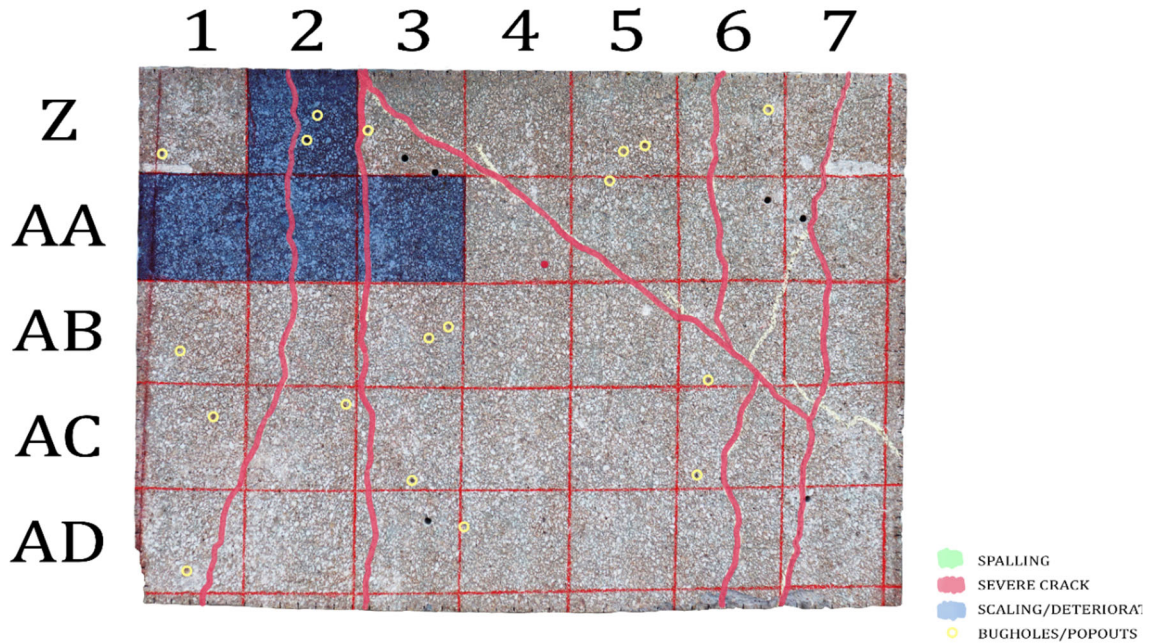
Figure 5.6: Visual Survey –Slab 6

	1	2	3	4	5	6	7
Z	37	38	34	37	37	40	38
AA	37	41	35	37	33	32	35
AB	34	33	33	35	34	32	36
AC	33	36	36	35	40	30	34
AD	39	36	36	36	41	36	34
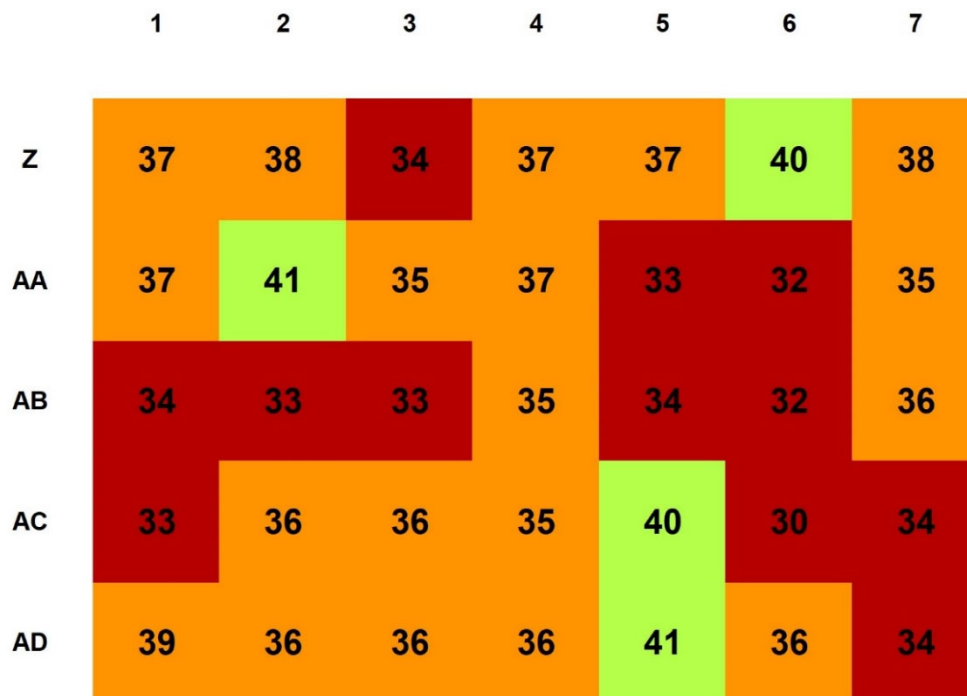
Figure 5.7: Surface Hardness Survey – Slab 6
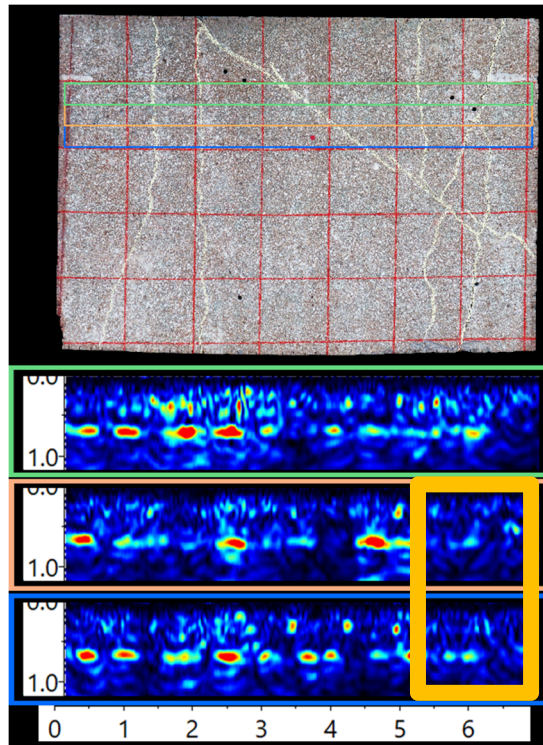
Figure 5.8: Pulse Echo Scan – Slab 6 AA
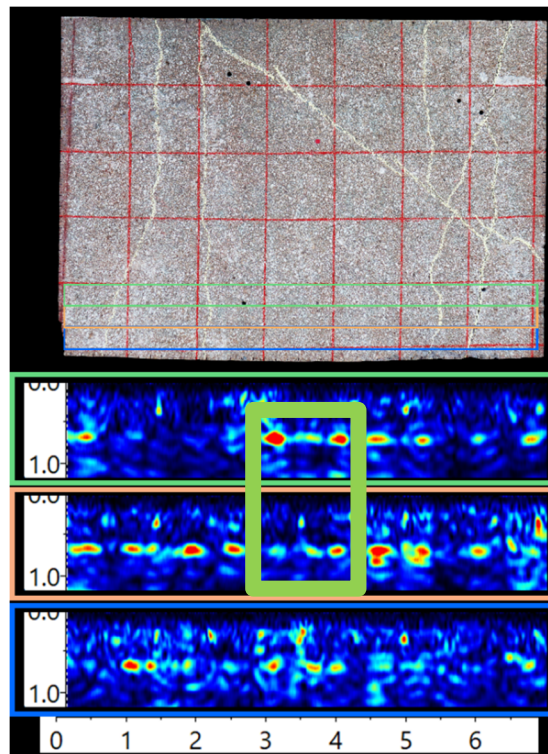
Figure 5.9: Pulse Echo Scan – Slab 6 AD
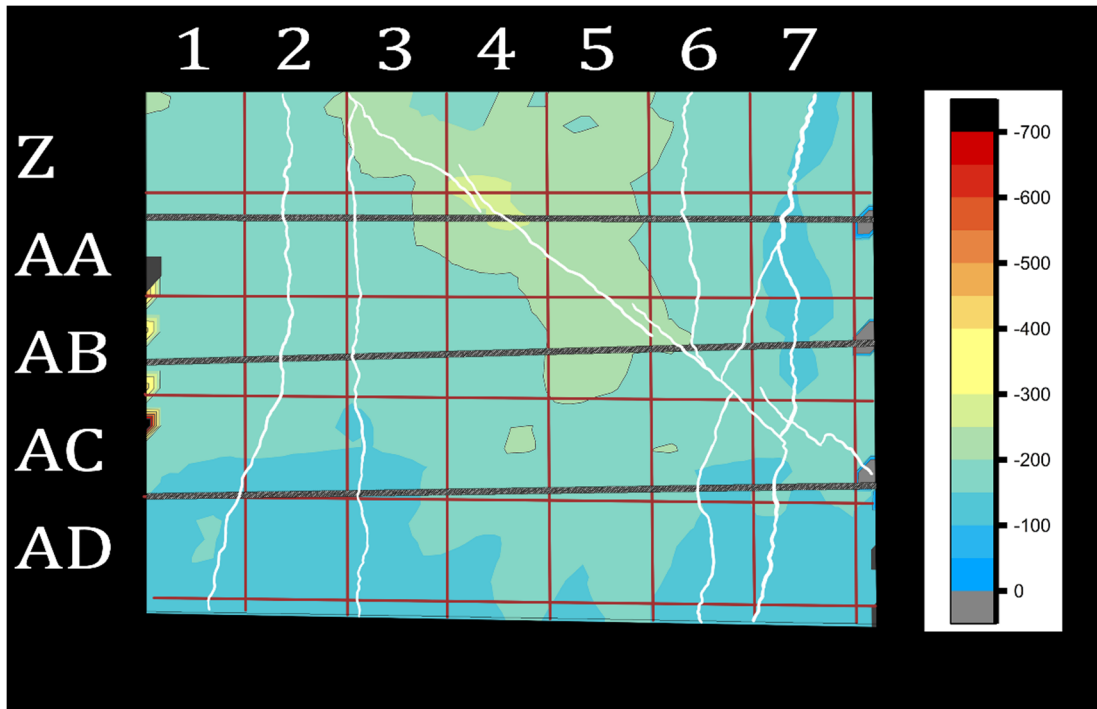
Figure 5.10: Half-Cell Potential Map for Longitudinal Rebar – Slab 6
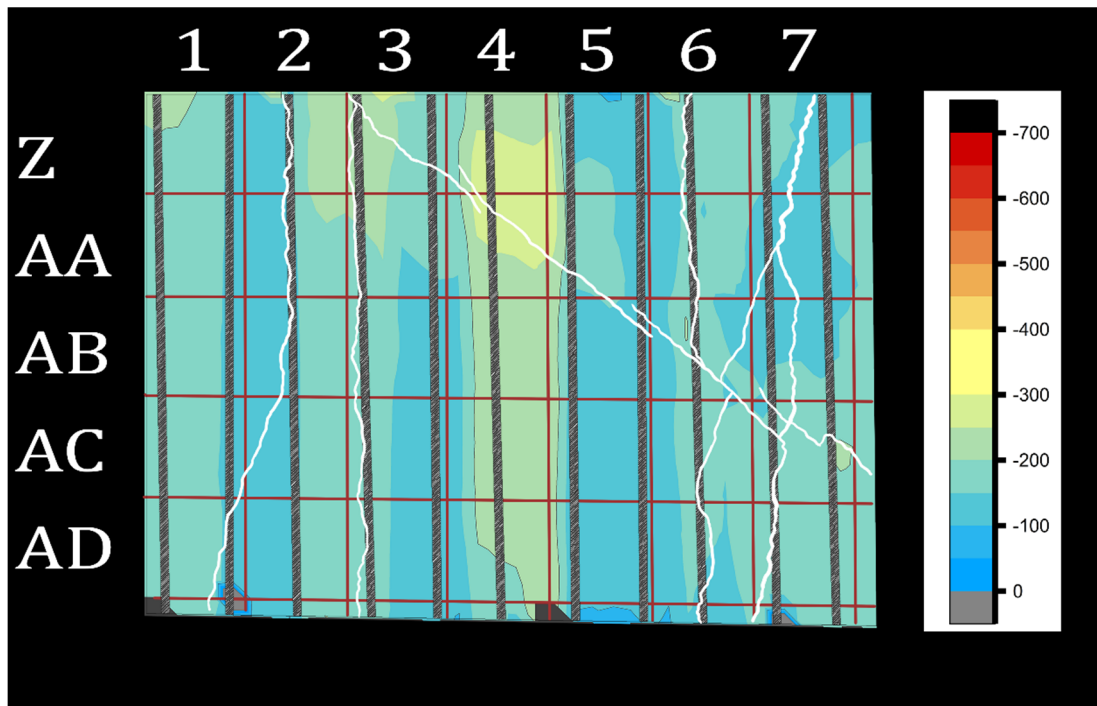
Figure 5.11: Half-Cell Potential Map for Transverse Rebar – Slab 6
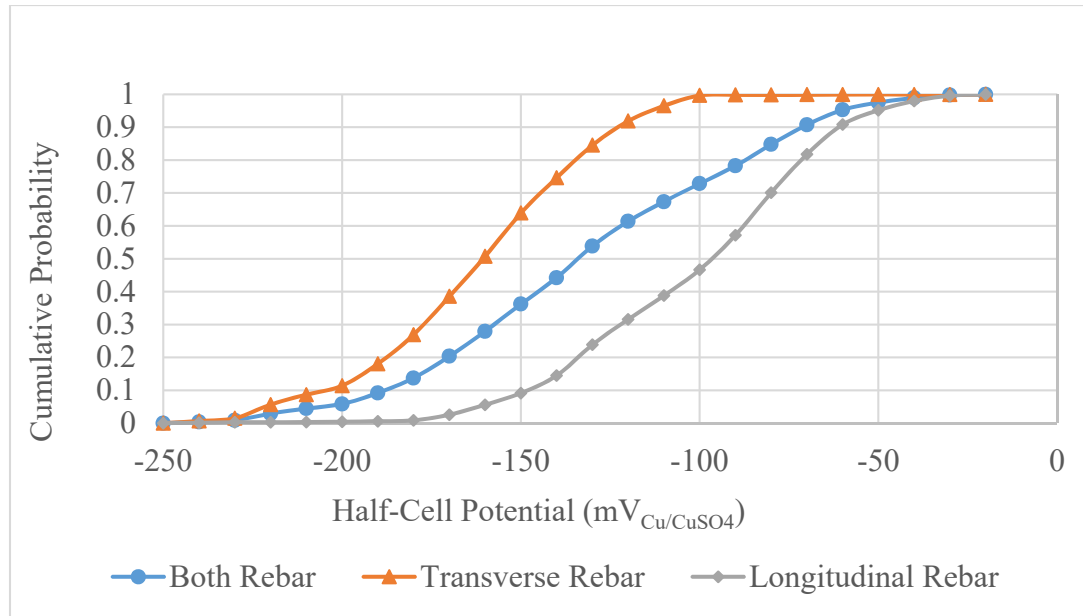
Figure 5.12: Half-Cell Probability Distribution – Slab 6

5.2.4.1 Determination of Coring Locations for Colorimetric Testing

Based on the results of the non-destructive survey, coring locations were determined to further the analysis and identify presence of chlorides and carbonation. The location of what was deemed "poor", AA5/AB5 and AA6/AB6 was mostly determined by the high potential gradients seen in the half cell survey in addition to a high density of cracking in that area. The pulse echo scan, figure 5.8, reveals no clear indication of a back wall presumably from the severe crack located in that area.

The location of good cores located in AD4, was based on the low potential gradient seen in that region for longitudinal rebar and low potential magnitude in the transverse rebar. Additionally, this is the only region in the slab that did not exhibit any cracking and produced a good pulse echo scan indicated in figure 5.9. A summary of core location is provided in Table 5.4.

Table 5.4: Coring Locations for Calorimetric Testing – Slab 6

Grid Box Location	Core Identification	Features/Rebar
Z4	High X-Cell	Rebar + crack
AD3	Low X-Cell	w/ rebar
AA5/AB5	Poor	w/ rebar
AA6/AB6	Poor	None
AD4	Good	w/ rebar
AD4	Good	none

5.3 Non-Destructive Assessment of Panel 7 - Black Rebar

5.3.1 Visual Condition Survey

Figure 5.13 demonstrates a picture of the slab surface along with a sketch highlighting surface distress features.

As seen in Figure 5.13, 2 severe transverse cracks parallel to each other can be seen in addition to the formation of a 2 severe diagonal cracks. The results of the crack index performed is 0.68. The cause of cracking cannot be determined. The entire surface area exhibits moderate to severe deterioration of aggregate and mortar, exposing the coarse aggregate. The reasoning for this deterioration is discussed in section 5.1.1. There is also the presence of a large spall located in AM7 with a depth of 1 inch. Very few construction defects are visible since the surface deterioration is so severe.

5.3.2 Surface Hardness Survey

The resulting rebound number range between 33 and 43, with a fairly normal distribution. No particular correlation was observed between rebound number and distress features, other than the low value in AM6 next to the spall seen in figure 5.14.

5.3.2.1 Determination of Coring Locations for Strength Estimation

Table 5.5 provides the locations for the cores for property analysis.

Table 5.5: Coring Locations for Properties Estimation – Slab 7

RN	33	35	37	39	41	43
Overlay	AN4	AJ9	AN9	AJ4	AL3	AJ2
No Overlay	AJ1	AM4	AN6	AK6	AL2	AJ2

5.3.3 Pulse Echo Survey

Individual pulse echo B scans of prominence are show in figures 5.15 and 5.16. The approximated wave velocities for scan AK and AL are 7467 ft/s and 7054 ft/s respectively. Pulse echo scans for this slab displayed similar characteristics to that of slab 6, discussed in section 4.3.3.

5.3.4 Half-Cell Potential Survey

A half-cell potential survey was performed on slab 7 and the results are shown in Figures 5.17 and 5.18. The recorded potentials ranged between -51 mV and -397 mV (Table 5.13). Because this individual high value would probably be overlooked, the difference in potentials may be more indicative of ongoing corrosion cells. Such is the case for the area surrounding the diagonal crack running from AJ6 to AL7, which exhibits the lowest recorded potentials for both longitudinal and transverse rebar. This crack in particular has an average width of 0.123 inches wide and a depth extending to the bottom of the slab.

The transverse rebar distribution seen in figure 5.19 was used to determine the potential threshold limits shown in table 5.13. The differences in distribution between the transverse and longitudinal rebar shows that the transverse rebar may be at a higher risk of ongoing corrosion, since a majority of the values are more negative than the longitudinal rebar.
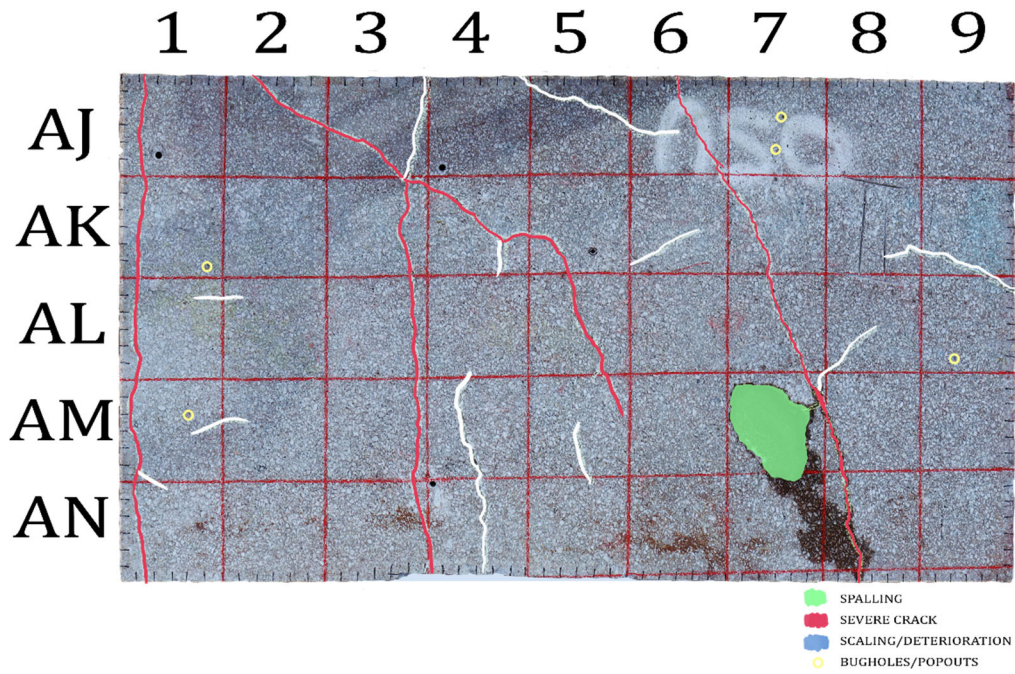
Figure 5.13: Visual Survey – Slab 7

	1	2	3	4	5	6	7	8	9
AJ	33	43	38	39	40	38	36	38	35
AK	39	40	40	38	38	39	39	39	37
AL	38	41	41	37	38	37	39	37	37
AM	42	35	38	35	34	34	39	36	40
AN	39	37	36	33	36	37	36	36	37
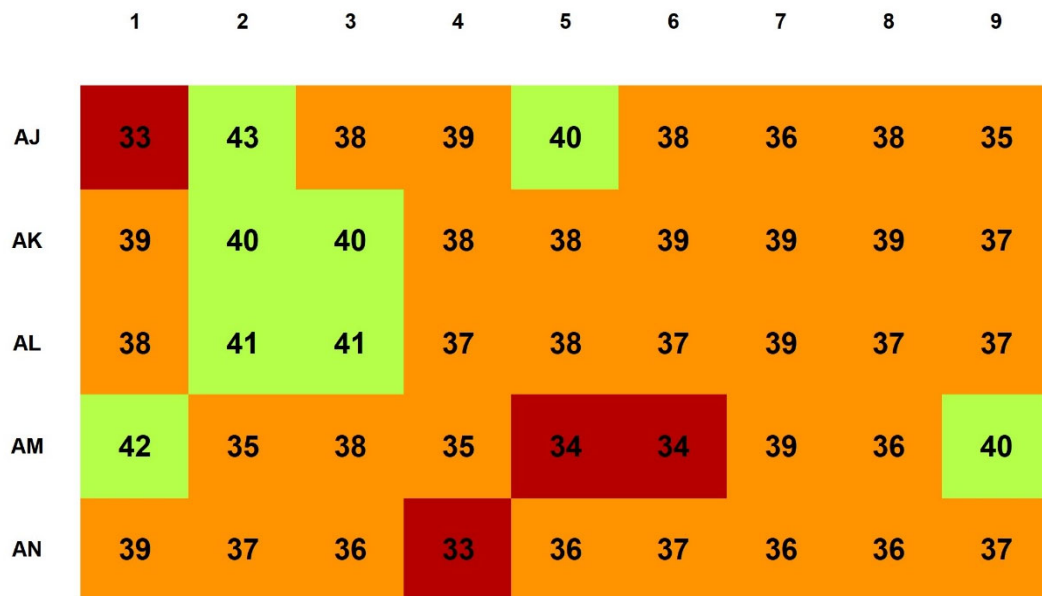
Figure 5.14: Surface Hardness Survey – Slab 7
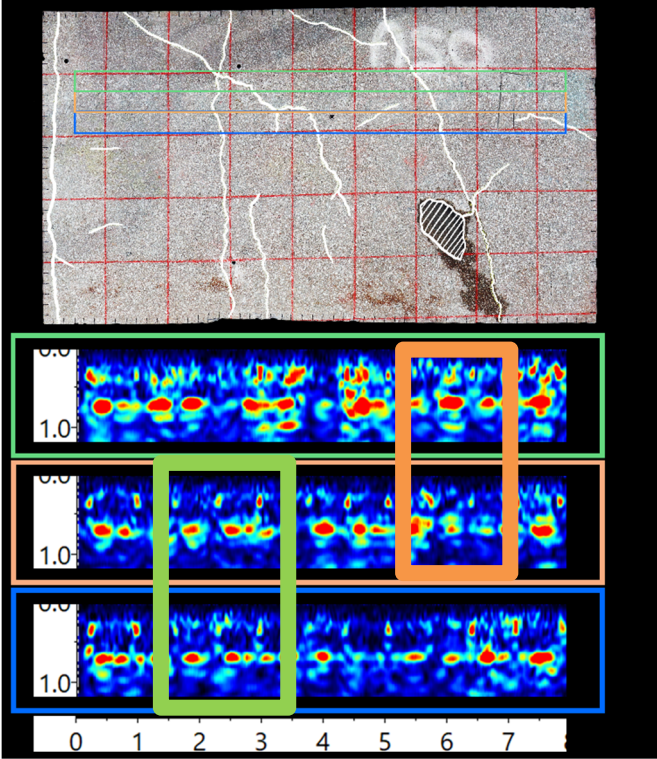
Figure 5.15: Pulse Echo Scan – Slab 7 AK
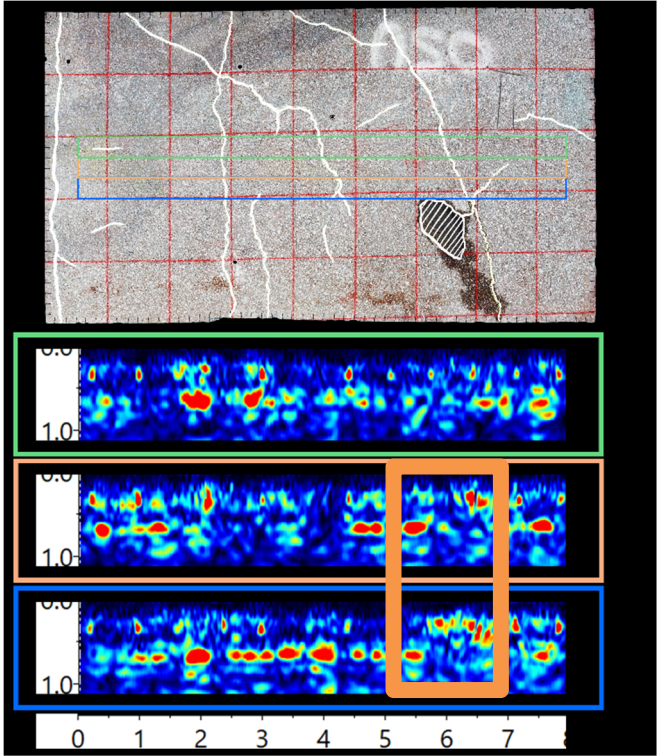
Figure 5.16: Pulse Echo Scan – Slab 7 AL
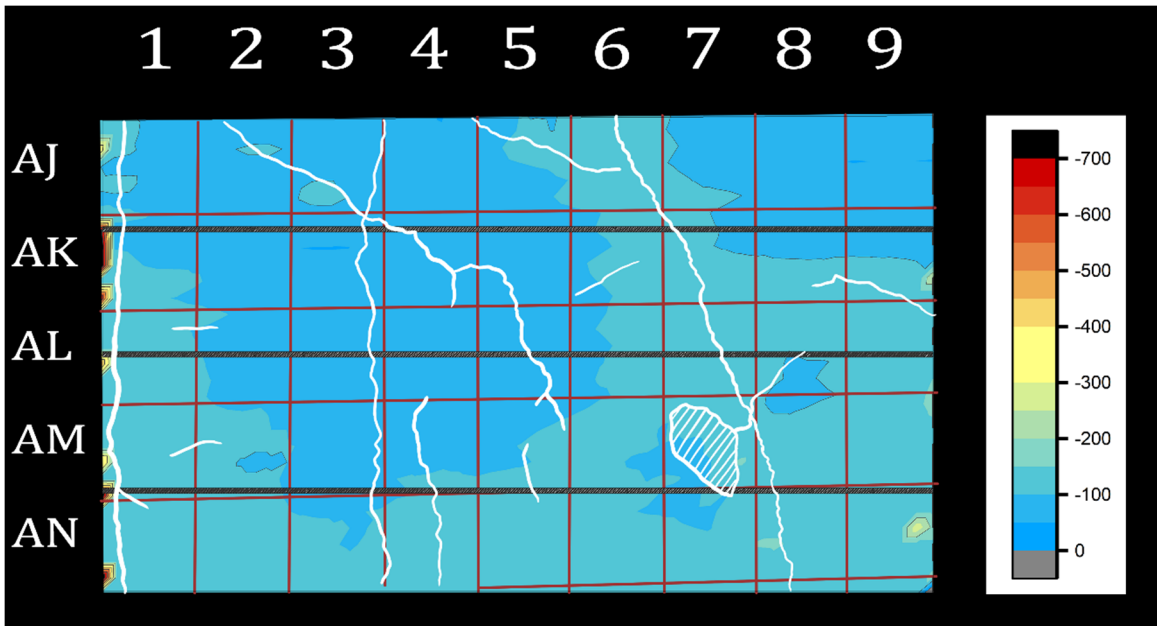
Figure 5.17: Half-Cell Potential Map for Longitudinal Rebar – Slab 7
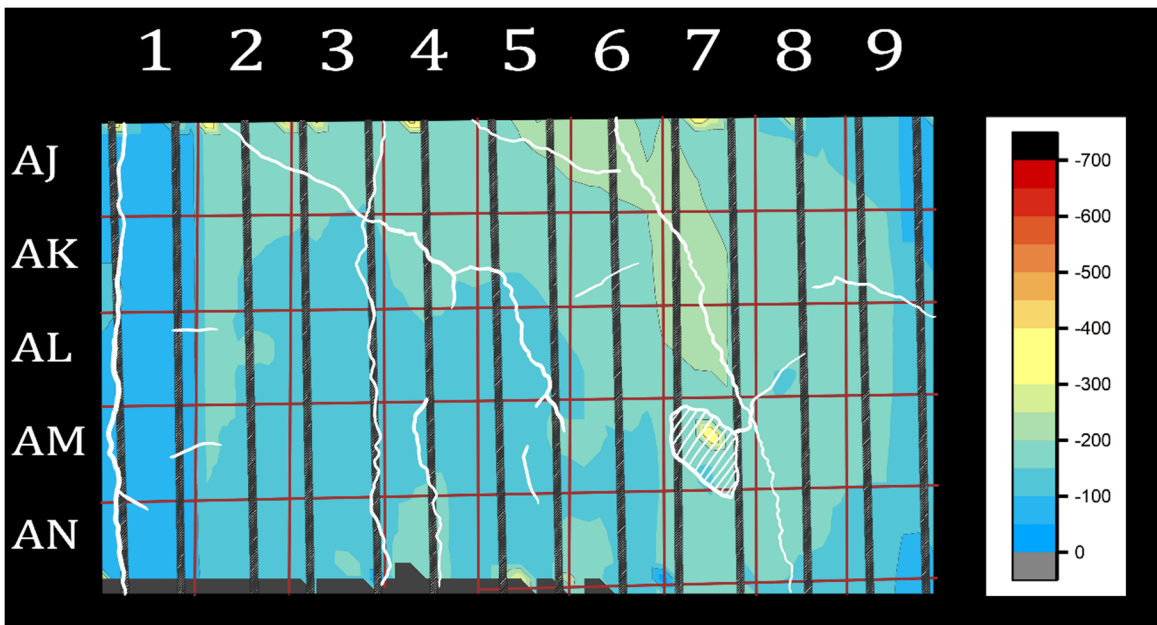
Figure 5.18: Half-Cell Potential Map for Transverse Rebar – Slab 7
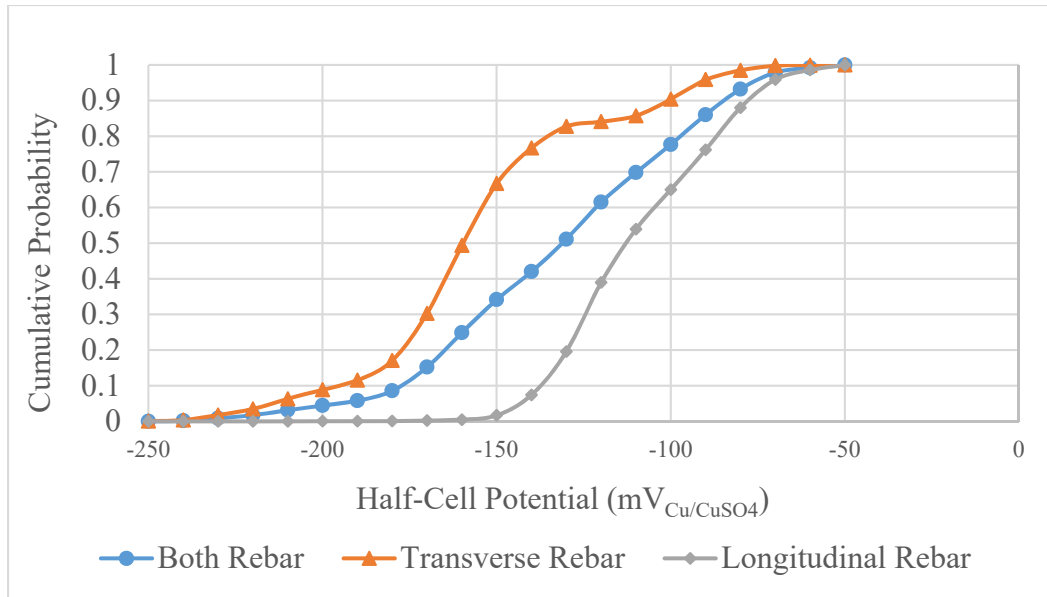
Figure 5.19: Half-Cell Probability Distribution – Slab 7

5.3.4.1 Determination of Coring Locations for Colorimetric Testing

Based on the results of the non-destructive survey, coring locations were determined to further the analysis and identify presence of chlorides and carbonation. The location of what was deemed "poor", AK7 and AL7 was mostly determined by the high potential gradients seen in the half cell survey in addition to the severe crack mentioned previously. Additionally, inhomogeneous material was observed in the pulse echo scans seen in figures 5.15 and 5.16 highlighted in orange. These results might indicate underlying construction defects such as honeycombing or be the result of internal cracking.

The location of good cores located in AL2/AL3 and AK3 was based on the low potential values observed in both transverse and longitudinal rebar. Additionally, this region displayed higher rebound values and low crack density compared to the rest of the slab surface. Figures 5.15 and 5.16, highlight the pulse echo scans from this area and show what would be expected of a good quality material, highlighted in green. A summary of core location is provided in Table 5.6.

Table 5.6: Coring Locations for Calorimetric Testing – Slab 7

Grid Box Location	Core Identification	Features/Rebar
AJ6	High X-Cell	Rebar + crack
AN1	Low X-Cell	w/ rebar
AK7	Poor	w/ rebar
AL7	Poor	crack
AL2/AL3	Good	w/ rebar
AK3	Good	None

5.4 Non-Destructive Assessment of Panel 1 – Epoxy-Coated Rebar

5.4.1 Visual Condition Survey

Figure 5.20 demonstrates a picture of the slab surface along with a sketch highlighting surface distress features.

There are 2 severe transverse cracks that run parallel to each other. The results of the crack index performed is 0.74. The cause of cracking cannot be determined. 37.5% of the surface area appears to have signs of moderate surface disintegration, located in the areas indicated in figure 5.20. The severity of disintegration of the ECR slabs is much less severe than that of the black rebar slabs. Areas indicated as moderate deterioration expose some coarse aggregate, but do not appear to have mortar disintegration surrounding the aggregate. The reasoning for this deterioration is discussed in section 5.1.1.

5.4.2 Surface Hardness Survey

After the visual survey was conducted, a non-destructive surface hardness test was conducted using a Schmidt rebound hammer. The resulting rebound number range between 46 and 56, with a majority between 50 and 54. No observable correlation

between rebound values and distress features can be made. It may be noted, that all values below 49 appear at the edges of the slab, thus indicating that the low value may be due to edge effects.

5.4.2.1 Determination of Coring Locations for Strength Estimation

In order to estimate the mechanical properties of the concrete material for this element, several cores, representative of the range in results, were taken. A total of 3 cores per location were taken for further property analysis (section 4.3). Table 5.7 provides the locations for the cores. Here, care was taken to avoid rebar in the core samples.

Table 5.7: Coring Locations for Properties Estimation – Slab 1

RN	46	48	50	52	54	56
	A8	E1	B3	C4	D2	D4

5.4.3 Pulse Echo Survey

Individual pulse echo B scans of prominence are show in figures 5.22 and 5.23. The approximated wave velocities for scan A and C are 7861 ft/s and 7982 ft/s respectively. The pulse echo survey revealed mostly homogeneous regions, with the exception of columns 1 and 2 where two transverse cracks are spaced closely. The loss of back wall reflections is noticed in areas of severe cracks.

5.4.4 Half-Cell Potential Survey

A half-cell potential survey was performed on slab 1 and the results are shown in Figures 5.24 and 5.25. The recorded potentials ranged between -211 mV and -494 mV (Table 5.14). As previously referenced from ASTM C876, the probability of ongoing corrosion is uncertain to high for all rebar. The low availability of oxygen at the rebar surface due to the epoxy coating may be the reason for higher potential values. Because of this, the use of potential difference and use of cumulative probability may be necessary for locating corrosion cells. High potential gradients are observed at locations where the

tested rebar changes. This is observed in the longitudinal rebar in row E and the transverse rebar in column 1. Based on the visual survey, the severe crack shadows a transverse rebar and yet produces low potential values, this indicates that the crack is not a product of ongoing corrosion and that the rebar may be enact so long as the coating is uncompressed.

The probability distributions shown in figure 5.26, reveal that both transverse and longitudinal rebar would elicit the same potential threshold levels, as seen in table 5.14. The majority of data points fall in the more negative region for both directions of rebar, and would be considered 'high risk' corrosion by the numeric technique alone.
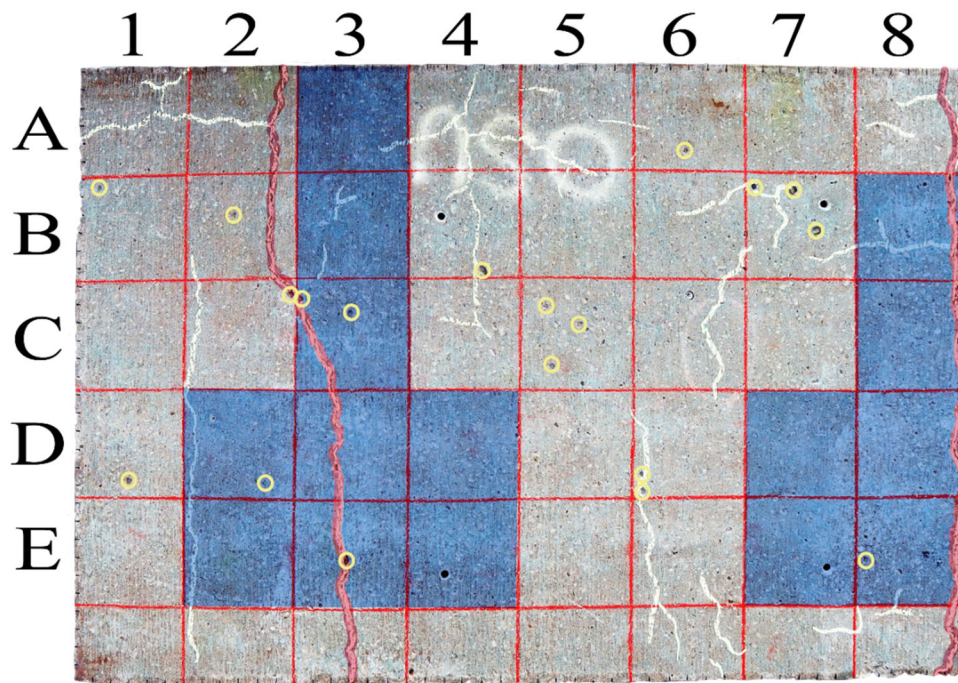
Figure 5.20: Visual Survey – Slab 1

	1	2	3	4	5	6	7	8
A	49	51	50	52	52	54	52	46
B	51	52	50	54	54	54	50	51
C	54	54	55	52	52	54	53	55
D	52	54	56	56	55	55	55	53
E	48	53	50	49	54	52	52	50
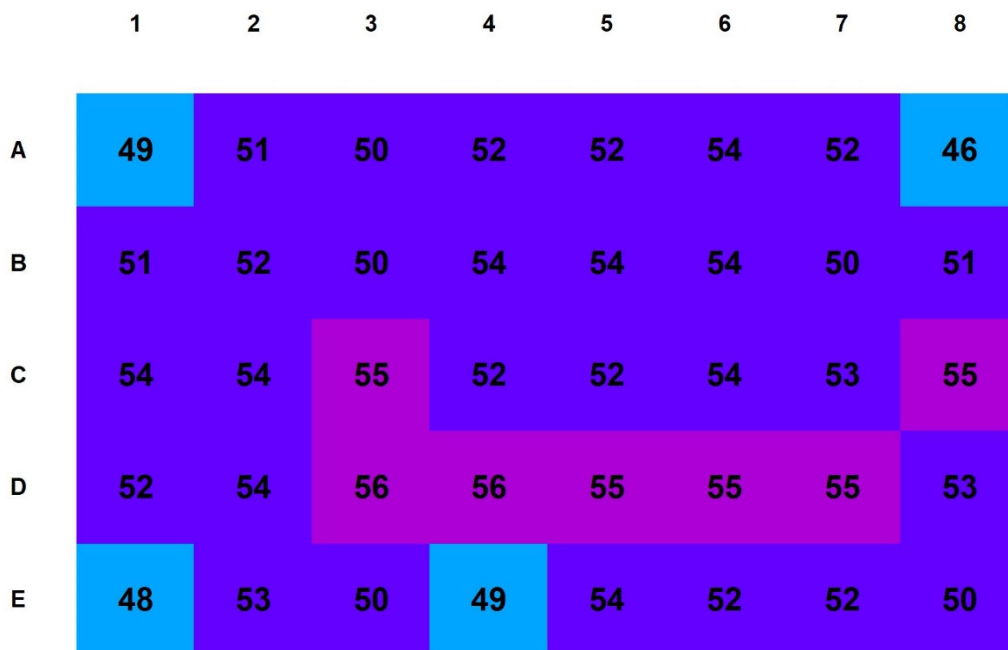
Figure 5.21: Surface Hardness Survey – Slab 1
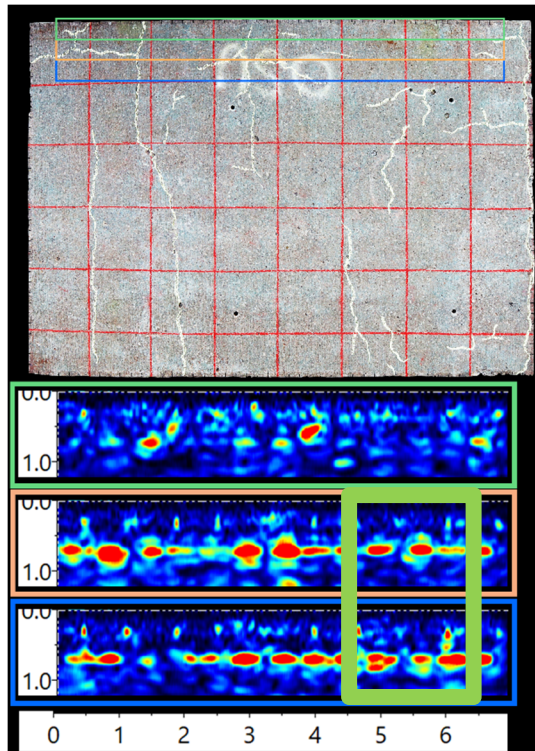
Figure 5.22: Pulse Echo Scan – Slab 1 A
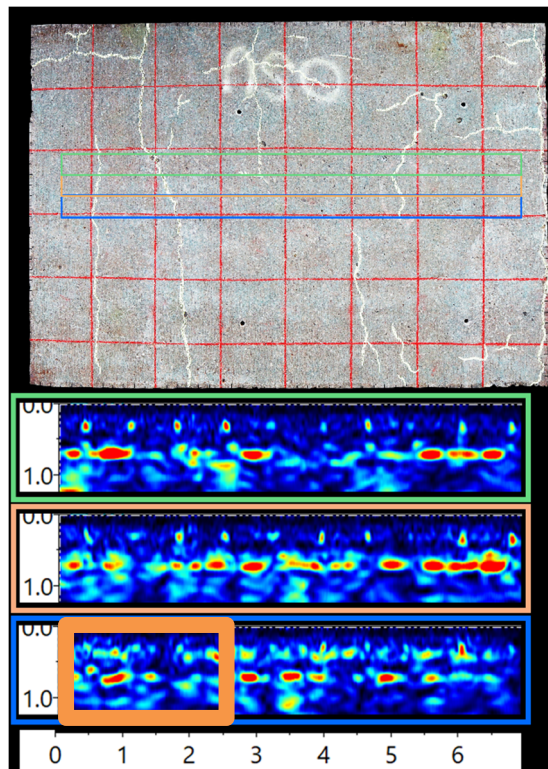
Figure 5.23: Pulse Echo Scan – Slab 1 C

Figure 5.24: Half-Cell Potential Map for Longitudinal Rebar – Slab 1
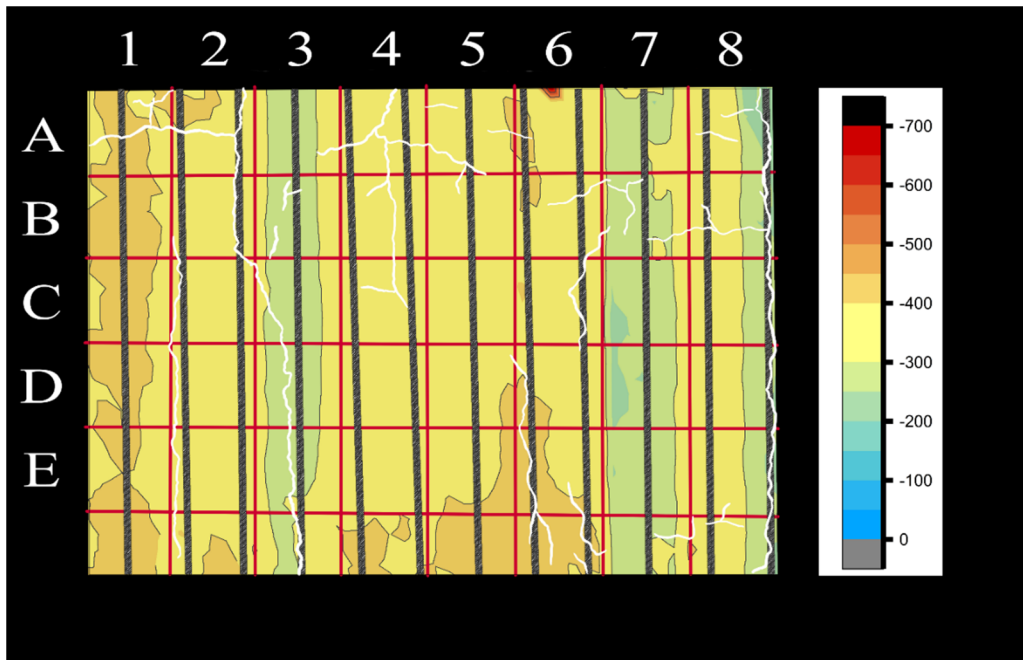
Figure 5.25: Half-Cell Potential Map for Transverse Rebar – Slab 1
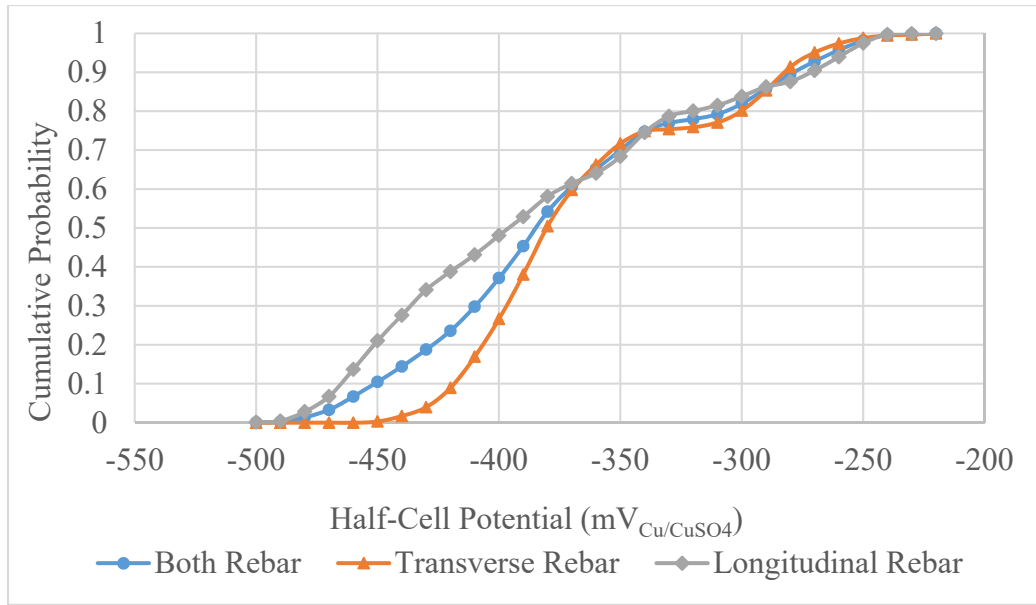
Figure 5.26: Half-Cell Probability Distribution – Slab 1

5.4.4.1 Determination of Coring Locations for Colorimetric Testing

Based on the results of the non-destructive survey, coring locations were determined to further the analysis and identify presence of chlorides and carbonation. The location of what was deemed "poor", B2 and C2 was mostly determined predominantly by the high local potential gradient and presence of cracking at those locations. It can also be seen that moderate surface reflections are present with low indication of the back wall in C2 as seen in figure 5.23, highlighted in orange.

The location of good cores located in A6 and A7 was based on the low potential values observed in the transverse rebar and the absence of cracking, deterioration and voids. The absence of surface distress features may also be the reason for the clear back wall and rebar reflections produced in A6 and A7 as seen in figure 5.22, highlighted in green. A summary of core location is provided in Table 5.8.

Table 5.8: Coring Locations for Calorimetric Testing – Slab 1

Grid Box Location	Core Identification	Features/Rebar
E4	High X-Cell	w/ rebar
C3	Low X-Cell	w/ rebar
B2	Poor	w/ rebar + crack
C2	Poor	none
A6	Good	w/ rebar
A7	Good	None

5.5 Non-Destructive Assessment of Panel 4 - Epoxy-Coated Rebar

5.5.1 Visual Condition Survey

Figure 5.27 shows that there is 1 severe, transverse crack found in column 6 seen in figure 5.27. The results of the crack index performed is 0.42. The cause of cracking cannot be determined. 28.6% of the surface area appears to have signs of moderate surface disintegration. The severity of disintegration is the same as the other ECR slabs as mentioned in section 5.4.1.

5.5.2 Surface Hardness Survey

The resulting rebound number range between 50 and 57 with 90% of the values falling between 51 and 54. No observable correlation between rebound values and distress features can be made because of the small range of values.

5.5.2.1 Determination of Coring Locations for Strength Estimation

In order to estimate the mechanical properties of the concrete material for this element, several cores, representative of the range in results, were taken. A total of 3 cores per

location were taken for further property analysis (section 4.3). Table 5.9 provides the locations for the cores. Here, care was taken to avoid rebar in the core samples.

Table 5.9: Coring Locations for Properties Estimation – Slab 4

RN	50	52	53	54	55	57
	P3	T4	T2	T1	R6	T6

5.5.3 Pulse Echo Survey

Individual pulse echo B scans of prominence are show in figures 5.29 and 5.30. The approximated wave velocities for scan P and T are 7812 ft/s and 7900 ft/s respectively. The pulse echo survey for this slab indicated very clear reflections indicating the continuous location of the back wall in addition to rebar locations. Unlike the other slabs, the presence of cracks did not seem to diminish the pulse echo results in most cases, which may indicate that the cracks do not penetrate as deep into the surface as it may seem.

5.5.4 Half-Cell Potential Survey

A half-cell potential survey was performed on slab 4 and the results are shown in Figures 5.31 and 5.32. The recorded potentials ranged between -119 mV and -584 mV (Table 5.14). The reasoning for this is mentioned in section 5.4.4. Similar results regarding the presence of cracking at low potential areas is observed in slab 1 and discussed in section 5.4.4. Here the difference in potentials along with poles of activity may be more indicative of an ongoing corrosion cell. Such is the case in S7 area, where a pole exhibits the lowest recorded potentials for both transverse and longitudinal rebar.

The probability distributions shown in figure 5.33, is difficult to interpret for potential threshold levels due to the normally distributed results. Threshold levels seen in table 5.14 were determined by the slight point of inflection seen in the combined distribution for both transverse and longitudinal rebar.
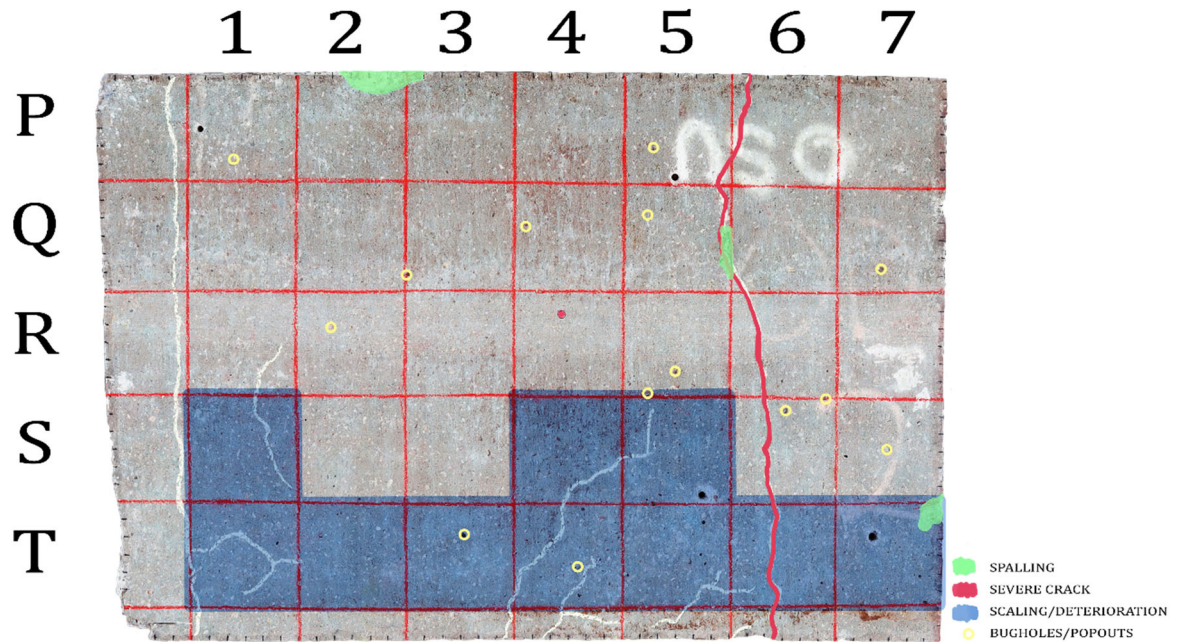
Figure 5.27: Visual Survey – Slab 4

	1	2	3	4	5	6	7
P	52	52	50	51	50	53	52
Q	56	51	54	54	53	53	52
R	54	54	51	52	53	55	52
S	51	53	52	54	53	52	54
T	54	53	54	52	51	57	53
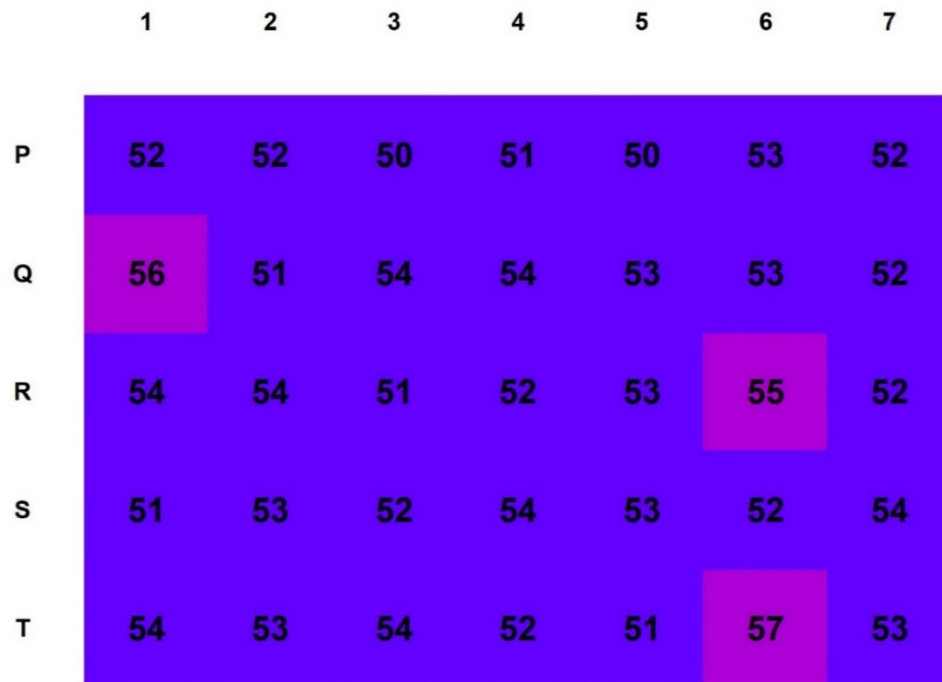
Figure 5.28: Surface Hardness Survey – Slab 4
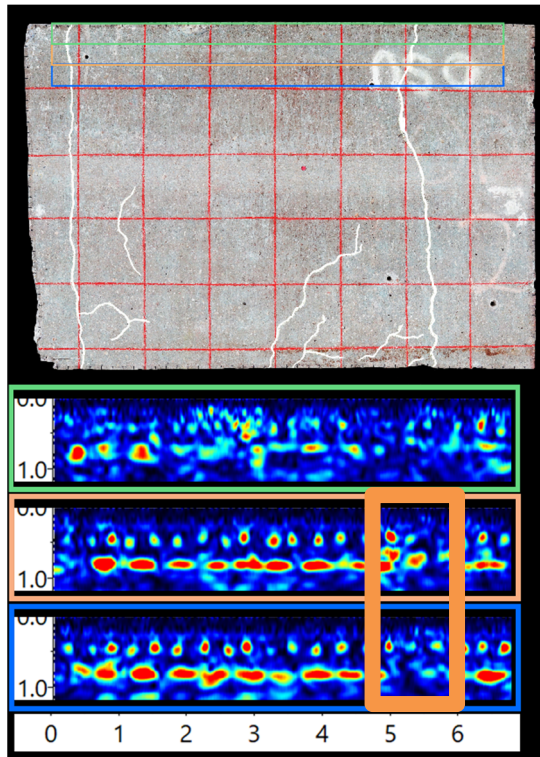
Figure 5.29: Pulse Echo Scan – Slab 4 P
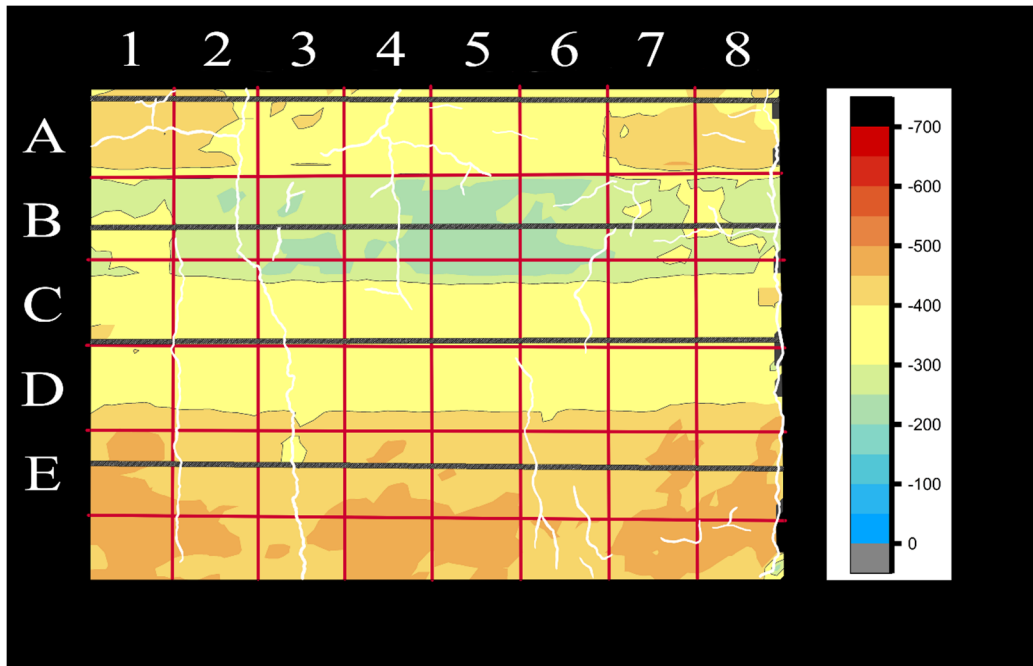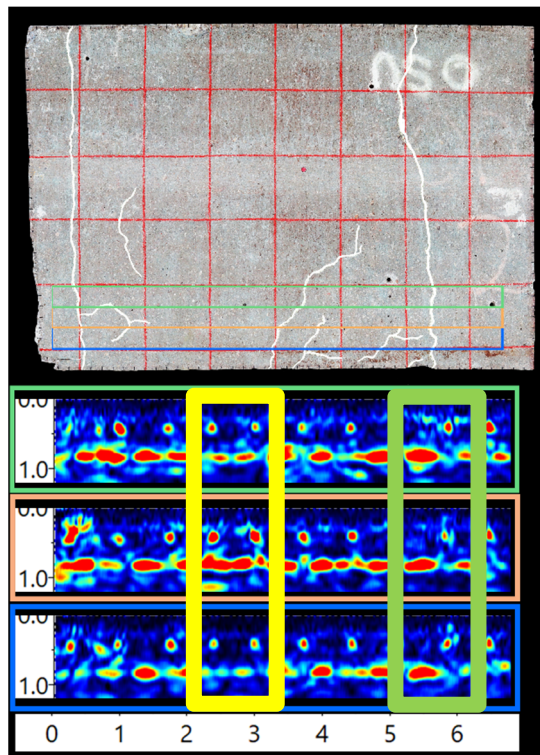

Figure 5.30: Pulse Echo Scan – Slab 4 T
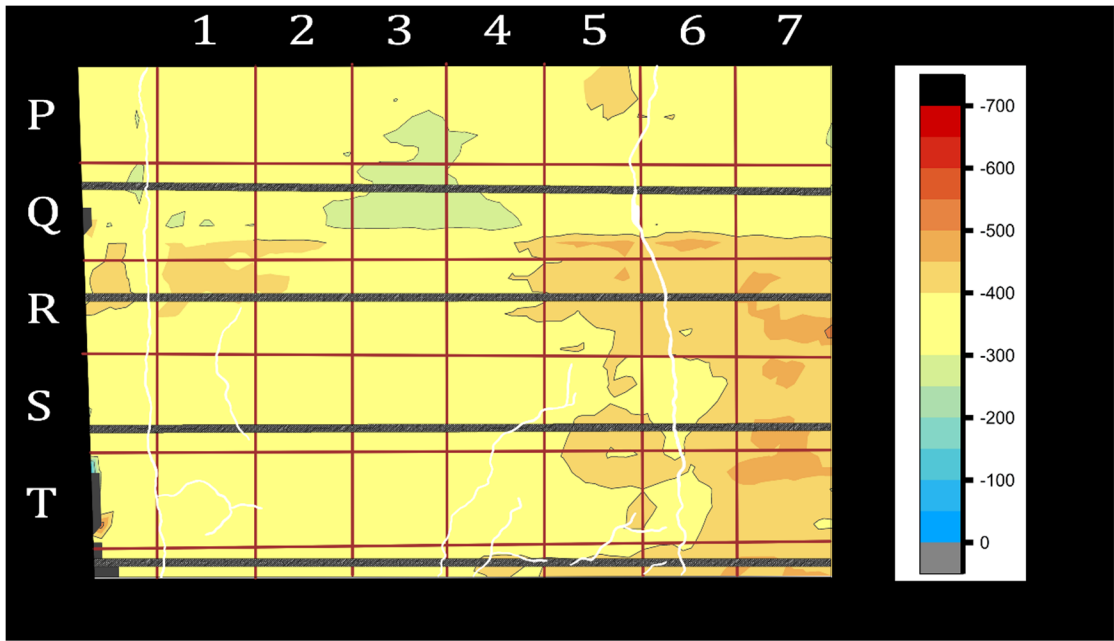
Figure 5.31: Half-Cell Potential Map for Longitudinal Rebar – Slab 4
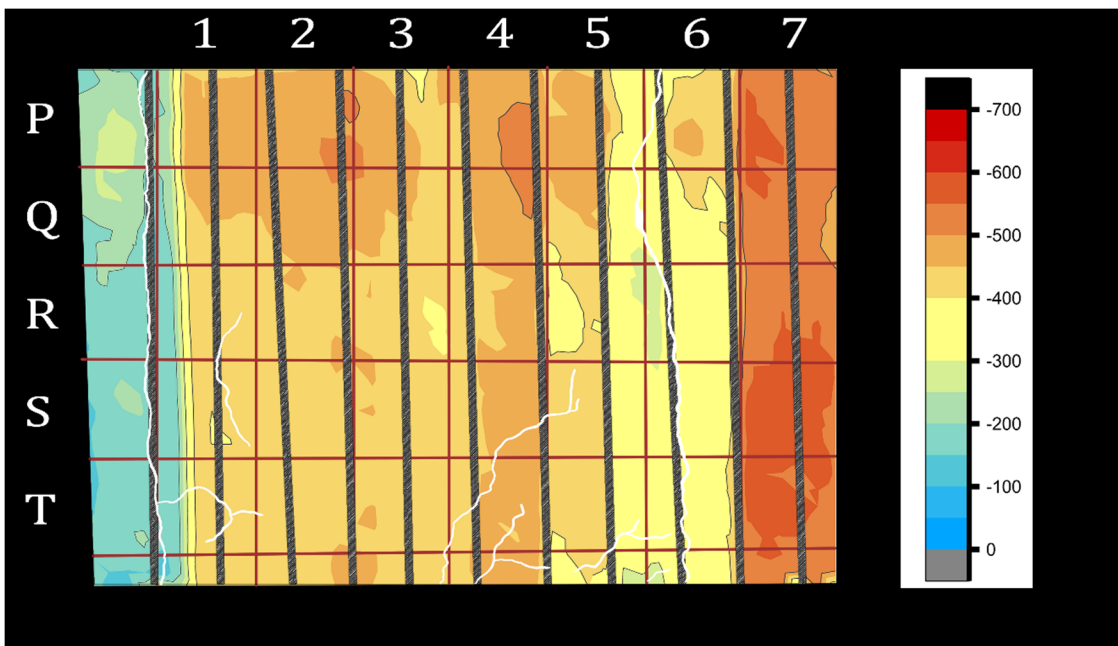
Figure 5.32: Half-Cell Potential Map for Transverse Rebar – Slab 1
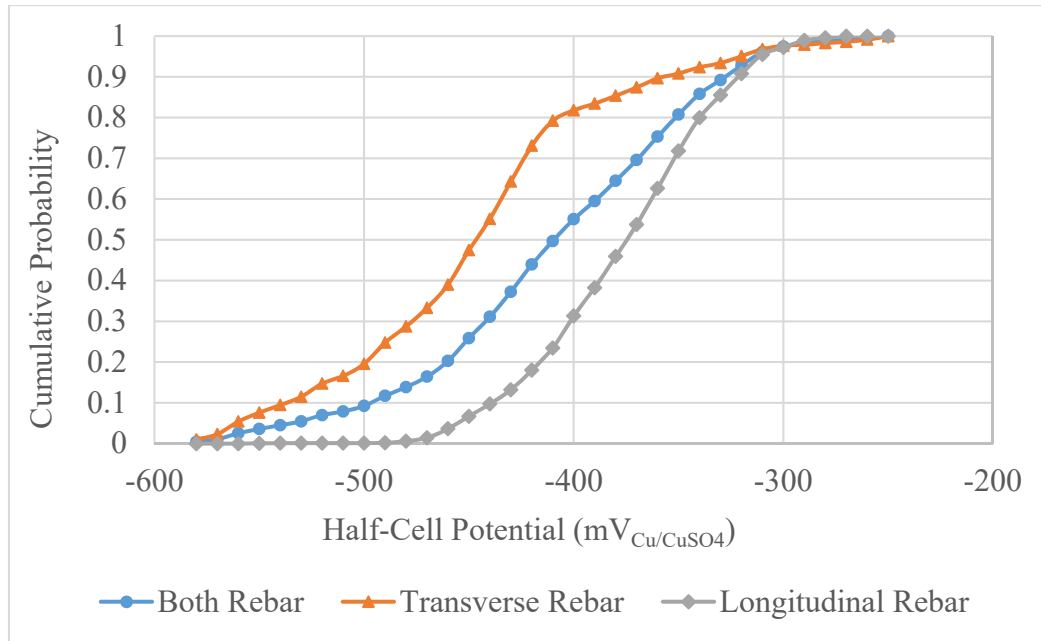
Figure 5.33: Half-Cell Probability Distribution – Slab 4

5.5.4.1 Determination of Coring Locations for Colorimetric Testing

Based on the results of the non-destructive survey, coring locations were determined to further the analysis and identify presence of chlorides and carbonation. The location of what was deemed "poor", P6 was determined by the low local potential value in addition to the presence of a severe crack along the transverse rebar producing that local minima. Additionally, inhomogeneous reflections were observed near the surface in the pulse echo scans for row P as seen in figure 5.29. The loss of back wall reflections may indicate that the crack has become severe at this location, since there is no similar effect from the crack in rows R, S and T as seen in figure 5.30, highlighted in green.

This slab in particular displayed a lot of areas with local, high potential gradients, so the location of good cores S2 and T3 were based on the low potential gradients in the region for both transverse and longitudinal rebar. Additionally, these boxes did not have any cracking present. Figure 5.30 highlights in yellow, the pulse echo scans from this area and show what would be expected of a good quality material. A summary of core location is provided in Table 5.10.

Table 5.10: Coring Locations for Calorimetric Testing – Slab 4

Grid Box Location	Core Identification	Features/Rebar
S7	High X-Cell	w/ rebar
T1	Low X-Cell	w/ rebar + crack
P6	Poor	w/ rebar +crack
P6	Poor	None
S2	Good	w/ rebar
T3	Good	none

5.6 Non-Destructive Assessment of Panel 9 - Epoxy-Coated Rebar

5.6.1 Visual Condition Survey

Figure 5.34 demonstrates a picture of the slab surface along with a sketch highlighting surface distress features.

There is 1 severe transverse crack in column 5 as seen in figure 5.34. The results of the crack index performed is 0.53. The cause of transverse cracks cannot be confirmed. However, a large majority of cracking is the result of plastic shrinkage as indicated by the renowned pattern seen in region AQ4 and AR4. 22.9% of the surface area appears to have signs of moderate surface disintegration. The severity of disintegration of the ECR slabs is much less severe than that of the black rebar slabs. The severity of disintegration is the same as the other ECR slabs as mentioned in section 5.4.1. The reasoning for this deterioration is discussed in section 5.1.1.

5.6.2 Surface Hardness Survey

After the visual survey was conducted, a non-destructive surface hardness test was conducted using a Schmidt rebound hammer. The resulting rebound number range between 50 and 59, with most values tending towards the upper range. No observable

correlation between rebound values and distress features can be made. This slab displayed an excessive amount of voids as compared to the other slabs. These voids were also much more prominent in surface area and depth, with some extending almost an inch into the concrete cover.

5.6.2.1 Determination of Coring Locations for Strength Estimation

In order to estimate the mechanical properties of the concrete material for this element, several cores, representative of the range in results, were taken. A total of 3 cores per location were taken for further property analysis (section 4.3). Table 5.11 provides the locations for the cores. Here, care was taken to avoid rebar in the core samples.

Table 5.11: Coring Locations for Properties Estimation – Slab 9

RN	50	51	53	55	57	59
	AS3	AS1	AO5	AR2	AO6	AQ5

5.6.3 Pulse Echo Survey

Individual pulse echo B scans of prominence are show in figures 5.36 and 5.37. The approximated wave velocities for scan AO and AP are 7740 ft/s and 7884 ft/s respectively. The pulse echo survey produced homogeneous results for all areas without cracking, in the presence of the transverse crack in column 5, the loss of back wall reflection is observed while areas with shrinkage cracking resulted in some areas of reflection loss altogether. In AP2-3, there is a localized area of reflections near the surface as seen in figure 5.37. In this area, there is also a dense grouping of popouts and bug holes in addition to shrinkage cracking which may be the causes of the results obtained in the survey.

5.6.4 Half-Cell Potential Survey

A half-cell potential survey was performed on slab 9 and the results are shown in Figures 5.38 and 5.39. The recorded potentials ranged between -244 mV and -643 mV (Table

5.14). According to the numerical interpretation in ASTM C876, the probability of an ongoing corrosion is high in most areas. As discussed in section 5.4.4, the lack of oxygen may be the cause of this and therefor identification of potential gradients may be more adapt to identifying corrosion cells. Such is the case in box AS6 where a pole exhibits the lowest recorded potentials for transverse rebar but also produces the highest potential gradients between the neighboring rebar in AS5.

The probability distributions for transverse rebar shown in figure 5.40 is the most ideal representation of a bimodal distribution, making the determination of the potential threshold levels found in table 5.14 simple. The transverse rebar also displays a majority of data points falling into the less negative region, while the longitudinal rebar data falls heavily in the intermediate range.
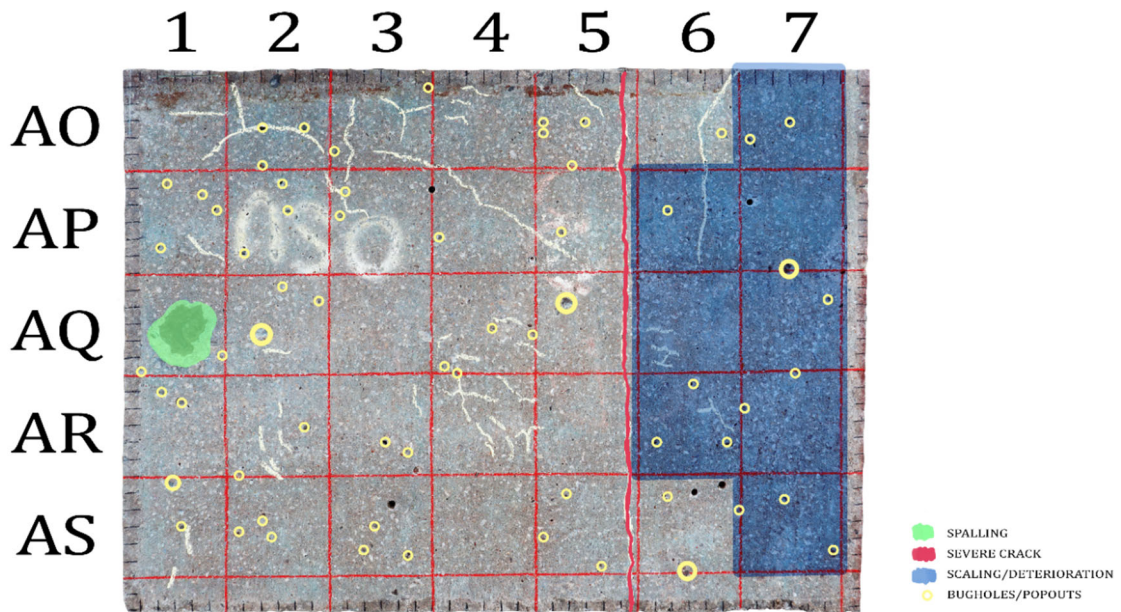
Figure 5.34: Visual Survey – Slab 9
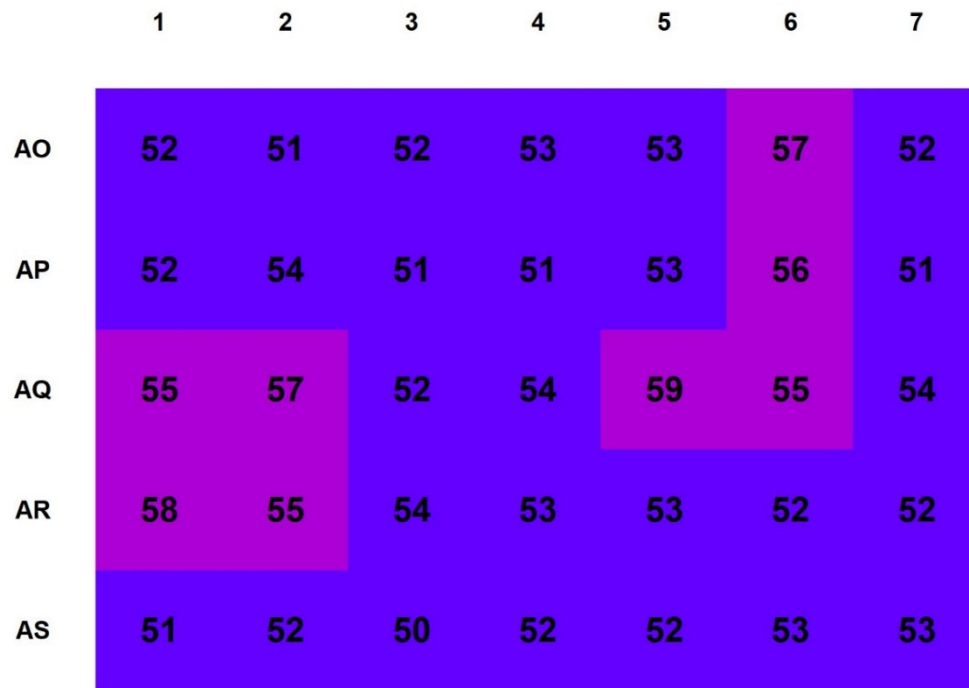
Figure 5.35: Surface Hardness Survey – Slab 9
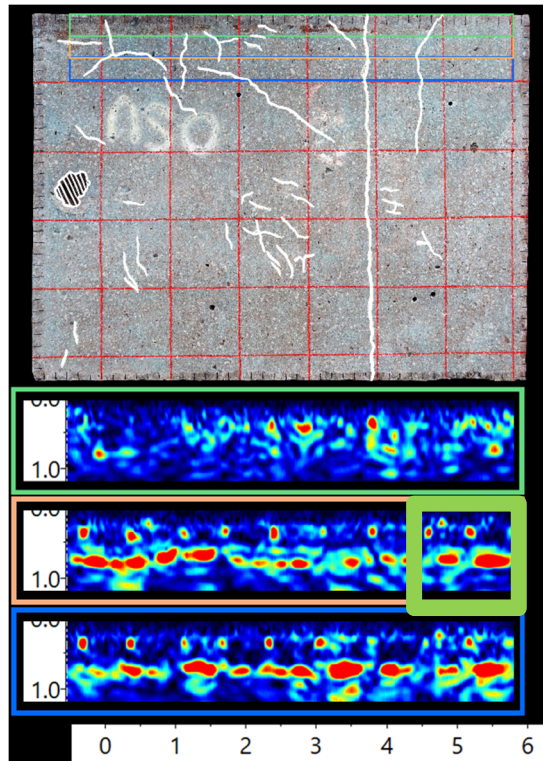
Figure 5.36: Pulse Echo Scan – Slab 9 AO
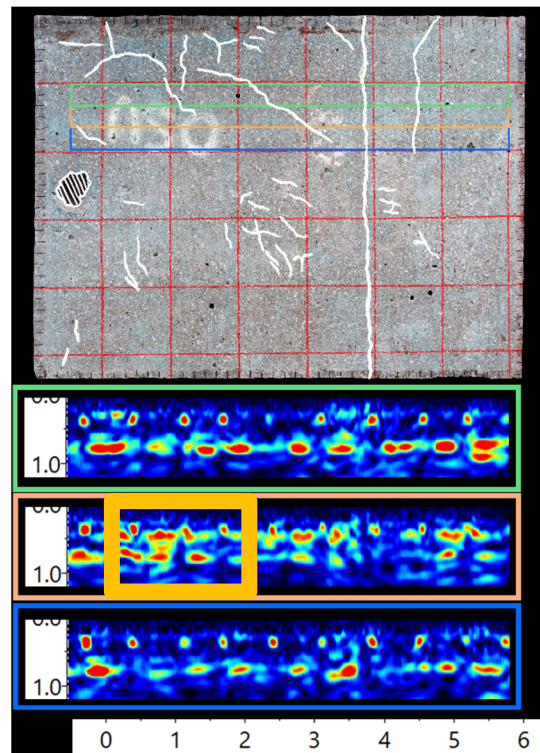
Figure 5.37: Pulse Echo Scan – Slab 9 AP
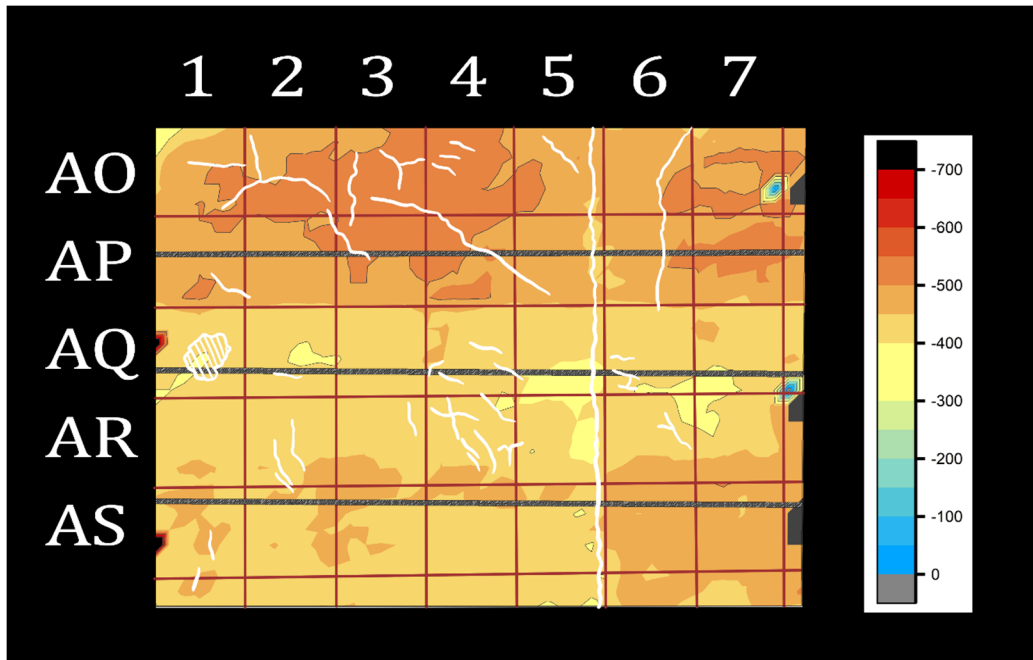
Figure 5.38: Half-Cell Potential Map for Longitudinal Rebar – Slab 9
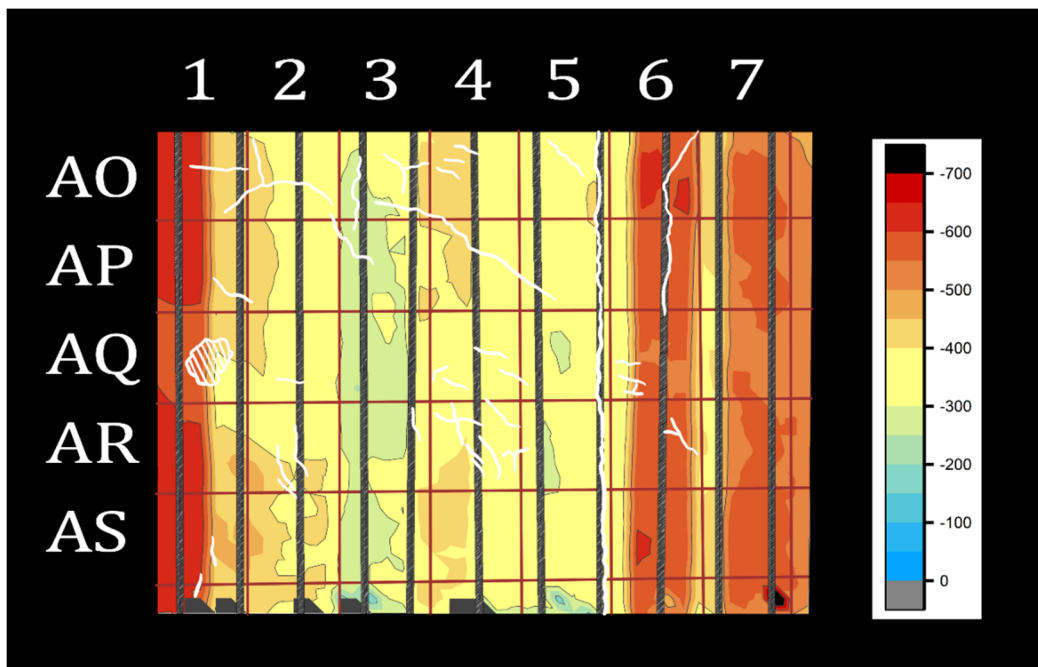
Figure 5.39: Half-Cell Potential Map for Transverse Rebar – Slab 9
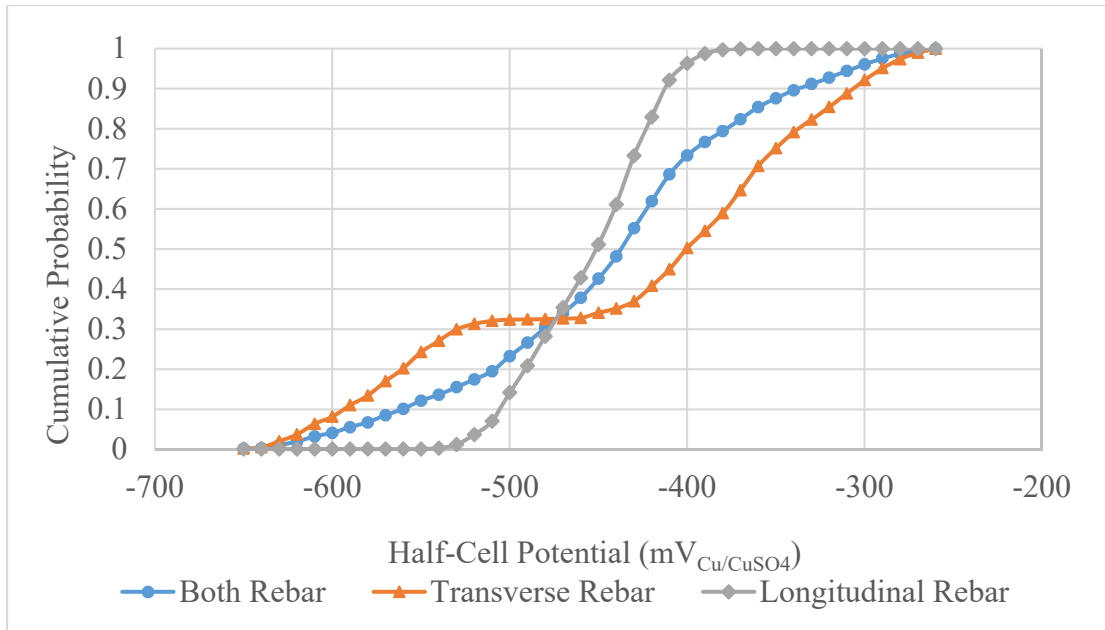
Figure 5.40: Half-Cell Probability Distribution – Slab 9

5.6.4.1 Determination of Coring Locations for Colorimetric Testing

Based on the results of the non-destructive survey, coring locations were determined to further the analysis and identify presence of chlorides and carbonation. The location of what was deemed "poor", AO2 and AP2 was mostly determined by the high potential values seen in the half cell survey in addition to the high crack density caused by plastic shrinkage in that area. The condition of pulse echo in AP2 was mentioned in section 5.6.3, and may allude to underlying construction defects in addition to the observed distress features in the area.

The location of good cores located in AO7 and AP5 was based primarily on the results of pulse echo as compared to the rest of the slab. Figure 5.36, highlights the pulse echo scans from this area and show what would be expected of a good quality material. AO7 displayed one of the lowest potential values, however is in an area with a low potential gradient and no severe cracking. AP5 on the other hand is in an area of highest potential values. Additionally, this region produced the highest rebound values for the slab. A summary of core location is provided in Table 5.12.

Table 5.12: Coring Locations for Calorimetric Testing – Slab 9

Grid Box Location	Core Identification	Features/Rebar
AS6	High X-Cell	w/ rebar + crack
AR3	Low X-Cell	w/ rebar
AO2	Poor	none
AP2	Poor	w/ rebar
AO7	Good	none
AP5	Good	w/ rebar + crack

5.7 Non Destructive Results Summary

A summary of non-destructive test results mentioned in sections 5.1 through 5.6 are shown in tables 5.13 and 5.14. Preliminary comparisons between individual slabs and rebar types can be made when observing this information. Black rebar slabs resulted in significantly lower RN values compared to ECR slabs, which could be indicative of more material degradation due to corrosion or the distress features observed in the visual and pulse-echo surveys. On the other hand, the high rebound values observed in the ECR slabs may be an indication of carbonation ingress from hardening as the result of the process described in section 2.3.2. The potential ranges for all ECR slabs are higher than those of the black rebar slabs, and based on the low percentage of active potential in slabs 4 and 9 it can be presumed that the high potential values are the result of an external condition and not necessarily indicating a high probability of corrosion for the entire slab surface.

Table 5.13: Non-Destructive Summary of Black Rebar

Slab	Crack Density (ft/ft²)	RN Range	Potential Range (mV)	Active Potential	Passive Potential	% Active Potential	% Passive Potential
3	0.46	33 - 42	79-265	<-170	>-140	16	58
6	0.86	30 - 41	90-294	<-140	>-100	44	33
7	0.68	33 - 43	51-397	<-140	>-100	42	30

Table 5.14: Non-Destructive Summary of Epoxy-Coated Rebar

Slab	Crack Density (ft/ft²)	RN Range	Potential Range (mV)	Active Potential	Passive Potential	% Active Potential	% Passive Potential
1	0.74	46 - 56	211-494	<-380	>-300	54	21
4	0.42	50 - 57	119-584	<-500	>-450	9	80
9	0.53	50 - 59	244-643	<-530	>-410	16	17

5.8 Destructive Assessment- Black Rebar

Based on visual observation, an overlay of approximately 4" was present for the entire slab surface. Since the core properties will be correlated to the NDT survey performed previously, it was deemed imperative to isolate the new overlay properties from the old concrete representing the original construction. As such a total of 36 cores were taken from slabs 3, 6 and 7 to evaluate the concrete properties. As previously stated in section 4.3, six sets of three sample cores representative of the range in NDT measurements obtained (range/5), for a total of 18, were taken to evaluate overlay properties and similarly to evaluate the original concrete properties. For each increment level, both sample pairs (overlay and no overlay) were obtained from each grid box identified in the

original surface hardness survey. With overlay cores were prepared for analysis by sawing them from the bottom producing a 2" x 4" cylinder core; while, the other set was sawed from the top removing the overlay and producing a 2" x 4" cylinder core. Here, this will better isolate the effect that the overlay may have on mechanical properties of the concrete and corrosion assessment.

The five concrete properties which are investigated for each slab are ultrasonic pulse velocity (UPV), bulk resistivity, dynamic and static modulus of elasticity, and compression strength.

5.8.1 Results Core Properties for Panel 3

The results of the destructive survey are presented in Appendix A, Tables A.1 to A.5. It can be seen that only UPV and compression strength produced p-values that resulted in no significant difference between sample sets for both overlay and no overlay cores. Static modulus of elasticity on the other hand, is the only property that resulted in a significant difference between both core types.

Appendix A, table A.1 shows that UPV produced extremely low coefficient of variations (COV) for all sample sets and therefore it can be said that the test produces accurate results for all cores. In a case such as this, any correlations that can be made between UPV (dependent variable) and RN (independent variable) are justified. The mean UPV for non-overlay cores is 15,432 ft/s and 14,991 ft/s for overlay cores. The means are not significantly different and thus it can be stated that the overlay material does not affect the UPV of the concrete.

Bulk resistivity of non-overlay samples produced a p-value of 0.004 indicating that there is a significant difference between sample set means, while the p-value for overlay cores was 0.5, indicating that there is no significant difference. As seen in table A.2, the COV for non-overlay cores was relatively low, but extremely high for overlay samples. The mean for non-overlay cores is 20.1 kΩ*cm and 161.8 for overlay cores. The significant difference between these two means shows that the overlay does have an effect on resistivity. The variability seen in the samples with overlays, may be due individual

overlay depths for each core, since it is shown that the overlay significantly increases resistivity.

Appendix A, table A.4 shows that the p-value produced for static modulus of elasticity is extremely low, indicating that there is a significant difference between sample sets for both non-overlay and overlay cores. The low COV can be attributed to the method of testing described in section 4.7; the variances are expected to be low since only one core is tested for modulus.

The COV produced for compression testing is high, and despite the ANOVA results stating that there is no significant difference between groups, this does not necessarily mean that the compression strength is not dependent on rebound value. The mean compression strength for non-overlay cores is 4,631 psi and 4,562 for overlay cores. Especially with the high variations for both groups, it is uncertain whether the overlay material has an effect on the compression strength.

5.8.2 Results Core Properties for Panel 6

The results of the destructive survey are presented in Appendix B, Tables B.1 to B.5. All properties exhibited high ANOVA p-values with the exception of static modulus of elasticity.

The results obtained for UPV and compression strength display the same characteristics as those seen in slab 3 and are discussed in section 1.1.1.

As seen in table B.4, both types of cores produced high p-values unlike the results discussed for slab 3, indicating that both non-overlay and overlay sample sets displayed no significant difference between individual sample sets. The mean resistivity for non-overlay cores is 18.1 kΩ*cm and 104.3 for overlay cores, therefor there is a significant difference between the two core types as seen in all other slab samples. Similar to the results discussed in section 1.1.1, the COV is higher for overlay samples.

5.8.3 Results Core Properties for Panel 7

The results of the destructive survey are presented in Appendix C, Tables C.1 to C.5. The results of all properties for this slab follow the same pattern as those discussed for slab 6 in section 1.1.2.

5.8.4 Compressive Strength Estimation for Black Rebar Slabs

As previously discussed, the formation of corrosion products will cause implications regarding the concrete quality and bond between the concrete and reinforcement. The correlation between strength and corrosion has been researched at length and determined to be inversely related. The sampling method used to determine coring locations for mechanical properties was based on the surface hardness survey in order to derive RN-strength relationships for estimation of concrete strength without further coring. The use of estimated concrete strength can be used in combination with other NDT tests to provide a better corrosion assessment.

The results of the surface hardness surveys for black rebar slabs are inadequate as they do not reflect the bulk material to any degree. The presence of the overlay heavily affected the rebound results and thus no correlation between strength and rebound were achievable. The average R^2 values for the linear regression models are shown in table 5.15. As seen in figure 5.44, the presence of overlay within the core, influenced compression to an extent where it can be derived that the variability in RN is strictly related to the difference between the overlay and bulk material. Although the coefficient of variation is unacceptable, it is worth mentioning that the cores which contained the overlay material exhibited an increasing relationship between RN and strength as compared to the cores with no overlay, which exhibited no discernable pattern.

Individual linear relationships for each black rebar slab are presented in Appendix G, figures G.1 to G.6.

Table 5.15: Rebound-Strength Linear Correlation for Black Rebar Slabs

Cores - No Overlay	R^2	Cores – Overlay	R^2
Slab 3	0.0221	Slab 3	0.3838
Slab 6	0.0119	Slab 6	0.00004
Slab 7	0.0015	Slab 7	0.4126
Average	0.0118	Average	0.2655

5.8.5 Influence of Overlay

As shown in figure 5.41, there is no significant effect on UPV created by the overlay, except for in slab 6. As mentioned in section 1.1.1, the low COV for all samples means that the significant difference seen in slab 6 may be indicative of a lesser quality bulk material as compared to the rest of the slabs.
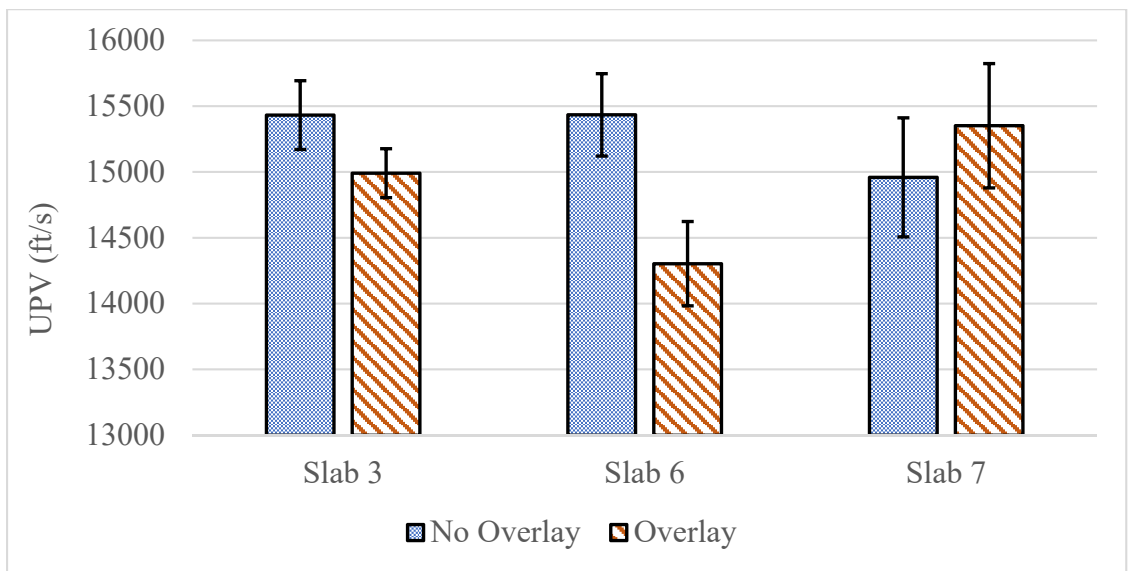
Figure 5.41: Effect of Overlay on UPV

The most apparent of dissimilarities caused by the overlay is seen in the bulk resistivity, figure 5.42. In increase in resistance with the overlay was expected, as the concrete is newer and will exhibit less material deterioration with lessened negative exposure conditions to that of the bulk material underneath. The resistivity increase is drastic and certainly would influence the half-cell potential results observed in the black rebar panels. As mentioned in section 1.1.1, the COV for overlay samples is high and probably influenced by the variability in overlay depth and quality between cores. Despite this, it is apparent that the influence of the overlay material on resistivity is significant.
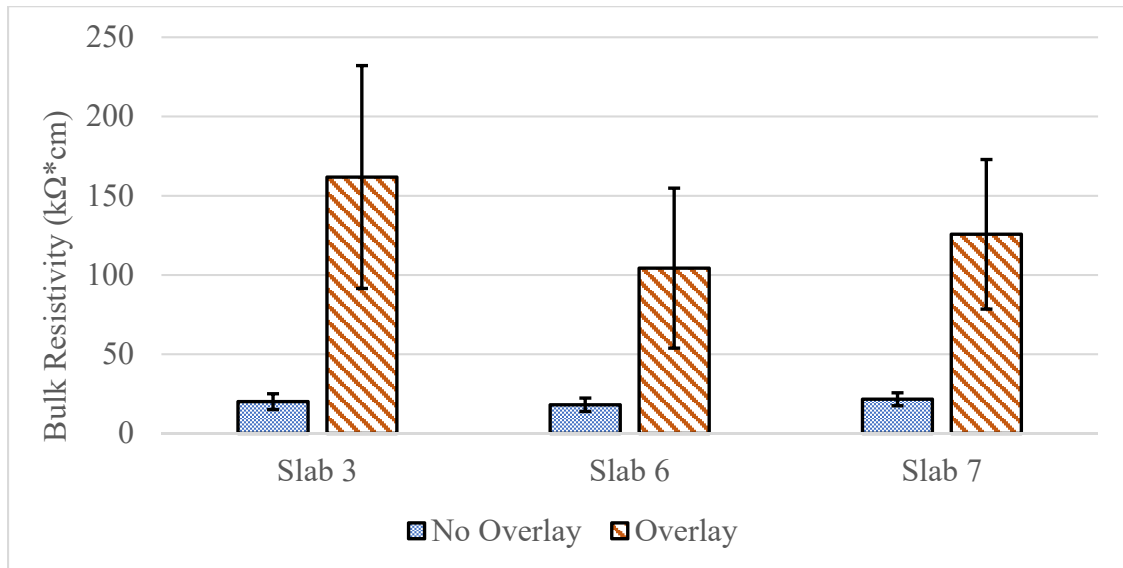
Figure 5.42: Effect of Overlay on Bulk Resistivity

It can be observed in figure 5.43, that there exists no significant relationship between static modulus of elasticity and the presence of an overlay material. The variances observed for the overlay cores are much higher than those of the non-overlay cores, which is presumably the result of having two very different concrete materials in each core. Specifically, the coarse aggregate content and size in the overlay material is much smaller than in the bulk concrete. In this case, the change in coarse aggregate size will have a large effect on small cores (3") since the size effect of the cores is prevalent in compression testing.
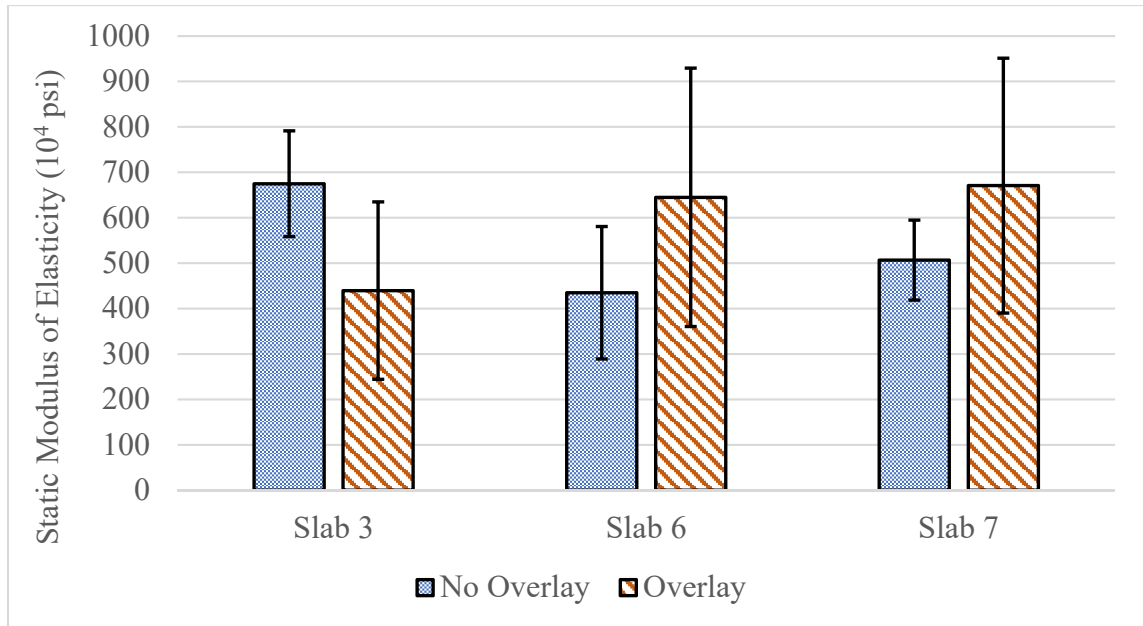
Figure 5.43: Effect of Overlay on Static Modulus of Elasticity

As observed in figure 5.44, the presence of the overlay induced an increase in core compression strength. The effects are considerably lower than that of bulk resistivity, but it can be inferred that the increase in strength can be attributed, in part, to the less deteriorated overlay material within the core. If this is the case, then the reduced effect can be explained by the combined strength of both materials, since the compression failure mechanism occurs in the middle of the core where the transition between the overlay and bulk material takes place. This strength increase along with the increase in bulk resistivity suggests that the overlay material is composed of a concrete mixture with a low w/cm ratio, designed to reduce permeability into the concrete surface. The large variances observed for all compression testing is probability the result of the small core size as compared to the coarse aggregate size in the bulk material. The location of coarse aggregate in relation to the core failure type, will therefor determine the core compression strength. In some cases, the inclusion of coarse aggregate for a core is low and produced a double cone failure type and significantly increasing the core compression strength, thus being the cause of large variations within each sample set.
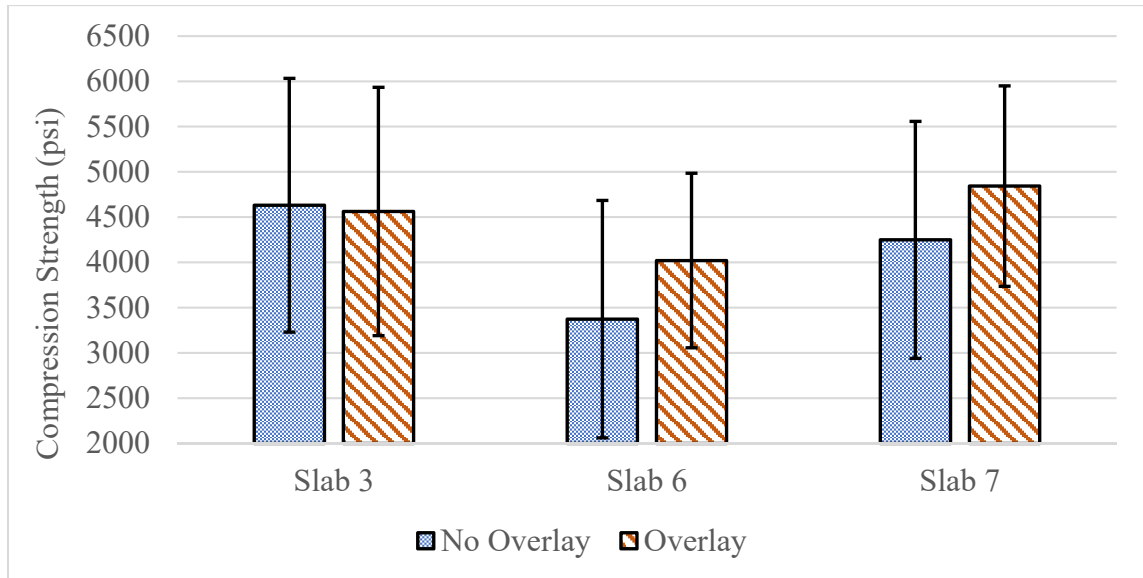
Figure 5.44: Effect of Overlay on Compression Strength

5.8.6 Results from Stain Testing for Black Rebar Panels

It is observed in black rebar samples that surface carbonation depth and chloride penetration are small. The exceptions to this are seen in cores L8, N7 and AL7 which can be seen in table 5.16 and 5.18. Two of the three were located at a crack and thus chloride ingress can be attributed to this. In most samples, the carbonation depth is negligible in part to the overlay material being newer and in part to having a better quality than that of the bulk material. As seen in the results for dye penetration in all samples, the presence of silane treatment is apparent and also successful. The lack of chloride penetration may be in part to the ability of the silane treatment to divert liquid from entering the concrete surface. There is no strong correlation between corrosion products and carbonation or chloride depth and so it could be interpreted that the inclusion of the overlay and silane treatment were measures that ultimately stopped the ongoing corrosion cells at the time of repair. It is important to note that the carbonation depth from the bottom of the slab with no repair never reaches the bottom layer of rebar indicating that the cover thickness may be enough in deterring carbonation induced corrosion in this study.

Table 5.16: Calorimetric Tests Results for Black Rebar – Slab 3

Core Class	Carbonation Depth from Top (in)	Carbonation Depth from Bottom (in)	Chloride Penetration (in)	Dye Penetration (in)	Rebar
N3/O3 High X-Cell	0.394	1.378	0	0	
N6/M6 Low X-Cell	0.098	0.787	0	0	
K2 Poor	0.098	0.984	0	0	NA
K3 Poor	0	0.591	0	0	
L8 Poor w/ Crack	0.591	0.984	1.772	0.009	
N7 Good	0.295	0.689	1.969	0	

Table 5.17: Calorimetric Tests Results for Black Rebar – Slab 6
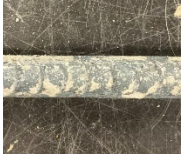
Core Class	Carbonation Depth from Top (in)	Carbonation Depth from Bottom (in)	Chloride Penetration (in)	Dye Penetration (in)	Rebar
Z4 High X-Cell w/ Crack	0	0.787	0	0	
AD3 Low X-Cell	0	0.886	0	0	
AA5/AB5 Poor	0.098	0.984	0	0	
AA6/AB6 Poor	0	0.394	0	0	NA
AD4 Good	0.591	1.378	0	0	

Table 5.18: Calorimetric Tests Results for Black Rebar – Slab 7

Core Class	Carbonation Depth from Top (in)	Carbonation Depth from Bottom (in)	Chloride Penetration (in)	Dye Penetration (in)	Rebar
AJ6 High X-Cell w/Crack	0	1.181	0	0	
AN1 Low X-Cell	0.098	1.181	0	0	
AL7 Poor w/ Crack	0	0.984	2.165	0	NA
AK7 Poor	0.886	0.787	0	0	
AL2/AL3 Good	0	0	0	0	
AK3 Good	0.197	0.197	0	0	NA

5.9 Destructive Assessment – Epoxy-Coated Rebar

5.9.1 Results Core Properties for Panel 1

The results of the destructive survey are presented in Appendix D, Tables D.1 to D.5. It can be seen that bulk resistivity and compression strength produced p-values greater than 0.05, resulting in no significant difference between RN groups. UPV and static modulus of elasticity on the other hand, both resulted in significant differences between groups.

 The COV of UPV tests are low and thus similar to those seen in the black rebar samples discussed in sections 5.8.1 through 5.8.3. The mean UPV was determined to be 15,527 ft/s.

As shown in table D.2, bulk resistivity testing produced a p-value of 0.477 and therefor displayed no statistically different means between RN groups, like the black rebar samples. The COV is noticeably less than those seen for both non-overlay and overlay black rebar samples.

Appendix D, table D.4 shows that the p-value produced for static modulus of elasticity is extremely low, indicating that there is a significant difference between sample sets. In addition to the low COVs for each sample set, it can be inferred that the modulus of elasticity is influenced by the surface hardness results.

Appendix D, table D.5 shows that the compression results produce both high COV and a high p-value similar to all other slab results. As mentioned in section 5.8.1, these results may not indicate that compression strength is not related to RN values.

5.9.2 Results Core Properties for Panel 4

The results of the destructive survey for slab 4 are presented in Appendix E, Tables E.1 to E.5.

 The UPV results of slab 4 are unlike in slab 1, as can be seen in table E.1. The p-value produced by ANOVA was 0.461 which means there is no significant difference between

groups. This is the same outcome as seen in all the black rebar slabs discussed in sections 5.8.1 through 5.8.3.

As shown in table E.2, bulk resistivity testing produced a p-value of 0.001 and thus has a significant difference between sample sets. The COV for slab 9 are the lowest observed between all slabs for both black and ECR samples and is the reason for the low p-value produced.

Appendix E, table E.4 shows that the p-value produced for static modulus of elasticity is 0.08, just slightly higher than the other slabs, resulting in no significant differences between sample sets. The increase in p-value is most likely the result of a high COV produced by the 57 rebound sample set.

The same results as all other slabs for compression strength can be observed in table E.5. As mentioned in section 5.8.1, these results may not indicate that compression strength is not related to RN values.

5.9.3 Results Core Properties for Panel 9

The results of the destructive survey for slab 4 are presented in Appendix F, Tables F.1 to F.5.

 The p-value produced by ANOVA for UPV is 0.149 which means there is no significant difference between groups. This is the same outcome as seen in all the black rebar slabs discussed in sections 5.8.1 through 5.8.3 and ECR slab 4 discussed in section 5.9.2.

As shown in table F.2, bulk resistivity testing produced a p-value of 0.0005 and thus has a significant difference between sample sets. The COV for slab 9 is noticeably less than the other slabs and is the cause for the low p-value as seen in slab 6 as well.

Appendix F, table F.4 shows that the p-value produced for static modulus of elasticity is 0.76, which is the highest p-value produced among all slabs for modulus. The increase is the result of several high COV among the sample sets which may be the result of internal fractures caused during loading and unloading during testing.

The same results for p-value and COV as all other slabs hold true for slab 9 as seen in table F.5. As mentioned in section 5.8.1, these results may not indicate that compression strength is not related to RN values.

5.9.4 Compressive Strength Estimation for ECR Slabs

The linear correlations between RN and strength of cores obtained from the ECR slabs are summarized in table 5.19. The linear correlation between RN and strength were acceptable in the case of ECR slabs with no overlay. The strength equations derived from the linear line of best fit, can be used to estimate compression strength for the entire slab surface.

Individual linear relationships for each ECR slab is presented in Appendix G, figures G.7 to G.9.

Table 5.19: Rebound-Strength Linear Correlation for ECR Slabs

Slab Number	Strength Equation	R^2
Slab 1	$Y = 128.34x - 1761.2$	0.8091
Slab 4	$Y = 184.61x - 5266.3$	0.8473
Slab 9	$Y = 103.02x - 1617.2$	0.6075

5.9.5 Results of Stain Testing for ECR Panels

The results of carbonation penetration are similar to those seen in the black rebar samples while the chloride penetration is much higher. The presence of observable dye penetration in all samples indicates that the silane treatment is not present in the ECR slabs as it is in the black rebar slabs. It can be observed that the locations of highest chloride ingress coincide with crack locations as seen in core B2 in table 5.20, cores T2 and P6 in table 5.21 and cores AS6 and AP5 in table 5.22. Additionally, the cores which exhibited these depths of chloride penetration also produced more corrosion products as seen primarily in sample P6 where the chloride depth reached the top layer of rebar and induced corrosion despite the epoxy-coating.

Observation of S7 in table 5.21 shows that the results of a high half-cell measurement did not necessarily result in corrosion of the ECR rebar. However, excessive corrosion can be seen in the black rebar in the bottom mat. This may indicate the presence of a macrocell between the top and bottom rebar mats, since the top rebar would act as the cathode and therefor result in a severe half-cell potential reading.

Table 5.20: Calorimetric Tests Results for Epoxy-Coated Rebar – Slab 1

Core Class	Carbonation Depth from Top (in)	Carbonation Depth from Bottom (in)	Chloride Penetration (in)	Dye Penetration (in)	Rebar Condition
E4 High X-Cell	0.295	0.787	1.378	0.034	
C3 Low X-Cell	0.197	0.984	1.378	0.054	
B2 Poor w/ Crack	0.098	1.969	1.969	0.038	
C2 Poor	0.197	0.787	0.984	0.044	NA
A6 Good	0	4.0	3.0	0.066	
A7 Good	0.591	0.984	1.772	0.032	NA

Table 5.21: Staining Results for Epoxy-Coated Rebar – Slab 4
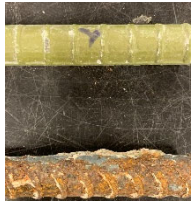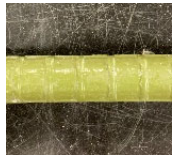
Core Class	Carbonation Depth from Top (in)	Carbonation Depth from Bottom (in)	Chloride Penetration (in)	Dye Penetration (in)	Rebar
S7 High X-Cell	1.378	0.591	0.394	0.026	
T1 Low X-Cell w/ Crack	0	1.378	1.575	0.031	
P6 Poor w/ Crack	0.098	0	2.362	0.064	
P6 Poor	0	1.181	0.197	0.059	NA
S2 Good	0.098	0.197	1.181	0.049	
T3 Good	0.197	0	1.575	0.074	NA

Table 5.22: Staining Results for Epoxy-Coated Rebar – Slab 9

Core Class	Carbonation Depth from Top (in)	Carbonation Depth from Bottom (in)	Chloride Penetration (in)	Dye Penetration (in)	Rebar
AS6 High X-Cell w/ Crack	0.197	1.476	2.362	0.207	
AR3 Low X-Cell	0.984	0.197	1.969	0.192	
AP2 Poor	0.098	0.787	1.083	0.074	
AP5 Good w/ Crack	0.098	0.984	2.362	0.059	

5.9.6 Colorimetric Results Summary

Comparing the staining results between ECR and black rebar samples indicates a significant difference for chloride penetration depth and dye penetration as displayed in table 5.23. These differences can be attributed to the overlay material which has shown significantly higher resistivity than that of the bulk material. In addition to this, the implementation of an overlay involves removing surface material which depending on

the time of removal, can eliminate all chloride penetration at that time; the new material will exhibit no chloride penetration and will be free of carbonation products upon placement. Additionally, based on the dye penetration results it is observed that the black rebar slabs have some silane treatment which is not observed in the ECR and may have been applied at the same time as the overlay repair. Based on the lack of carbonation depth from the bottom of the slab with presumably no repair or loss of material, it can be presumed that the cause of corrosion in this study is through chloride induced passivation of the steel. The mean of chloride penetration for ECR depicts that there is not a widespread corrosion problem as the penetration depth has not reach the top layer of rebar in all cases. This is observed in tables 5.20 through 5.22 and mentioned in section 5.9.5.

Table 5.23: Mean Staining Results for ECR and Black Rebar

	Carbonation Depth from Top (in)	Carbonation Depth from Bottom (in)	Chloride Penetration Depth (in)	Dye Penetration (in)
Black Rebar	0.197	0.886	0.346	0
ECR	0.283	0.867	1.484	0.069

5.10 Factors that Influence Corrosion Assessment Using Non-Destructive Tests

This section aims to identify the most influential factors when conducting an accurate corrosion assessment, using the NDT methods in this study. Correlations between NDT results and mechanical properties will be explored to derive reasoning behind the results obtained for each slab. A better understanding of these relationships will aid in forming a reliable interpretation of NDT data regarding corrosion.

5.10.1 Influence of Interpretation Method for Half-Cell Potential

As discussed in section 2.7.1.2, there are two primary methods for interpretation of half-cell potential results (1) the numeric method and (2) the potential difference method. Despite the common knowledge that the numeric method is unsuitable in most cases, it is

the only method that has any standardized relationship between potential and corrosion probability. The use of a cumulative probability distribution has been suggested when accompanying the numeric approach. The frequency distribution is used to visually assign a threshold level for both passive and active corrosion zones, these zones are then used to identify at-risk locations. Results for all three of these methods were included in the previous sections.

In order to verify which method is most suited for corrosion assessment, the results from each method will be compared to the visually obtained corrosion results from sampled rebar based on the NDT survey.

The maximum potential for each rebar orientation within each slab was calculated and plotted against the potential difference. The results in figure 5.45, indicate a linear relationship with the most outlying data points belonging to the ECR samples. This relationship may indicate that there is a strong correlation between the numeric method and potential difference method, under certain conditions. If this is the case, the potential difference method would be superior to the numeric method as it will eliminate misinterpretations of half-cell data on the premise of magnitude alone. Further explanation of the complications of using the numeric method are discussed in following sections.
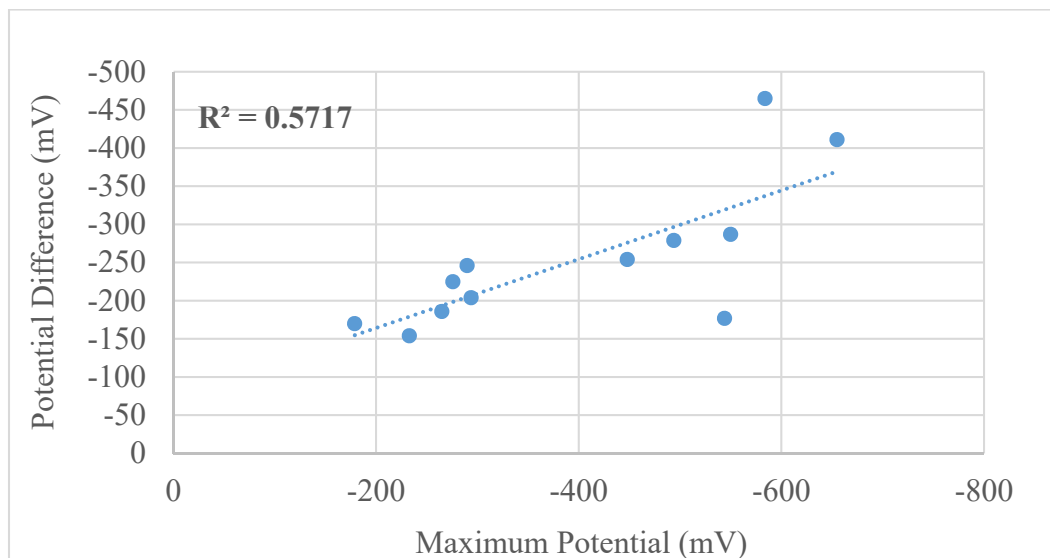
Figure 5.45: Numeric Method vs. Potential Difference for each Slab

To see if this relationship holds true on a smaller scale, the potential difference within each 1'x1' grid box was calculated and plotted against the associated maximum potential for each rebar orientation. The results are shown in figure 5.46 and indicate the same trend with an increasing variance at higher levels of half-cell potential.
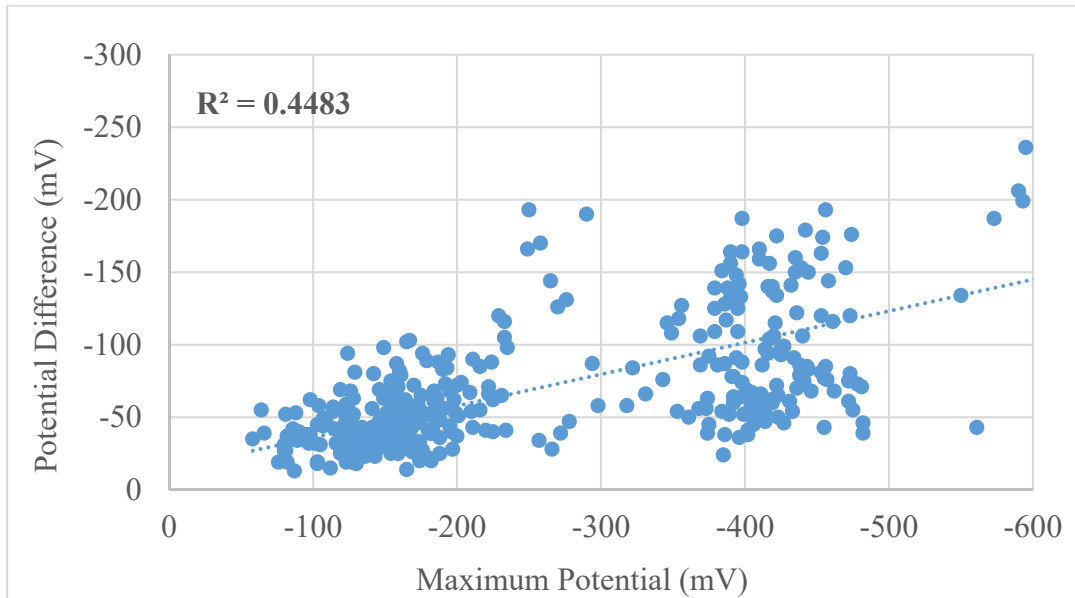
Figure 5.46: Numeric Method vs. Potential Difference for each Grid Box

Furthermore, to test if the variance differs between rebar types results were split up for each slab. Figure 5.47 shows results for a black rebar slab and the linear relationship is strong while figure 5.48 shows results for an ECR slab and the linear relationship becomes less reliable. The linear relationship observed in the standard rebar confirms that the potential difference test would produce the same corrosion assessment as the numeric method. Because of this, the variances observed in ECR could be justified and the potential difference method in this case, might be giving more accurate readings than that of the numeric method.
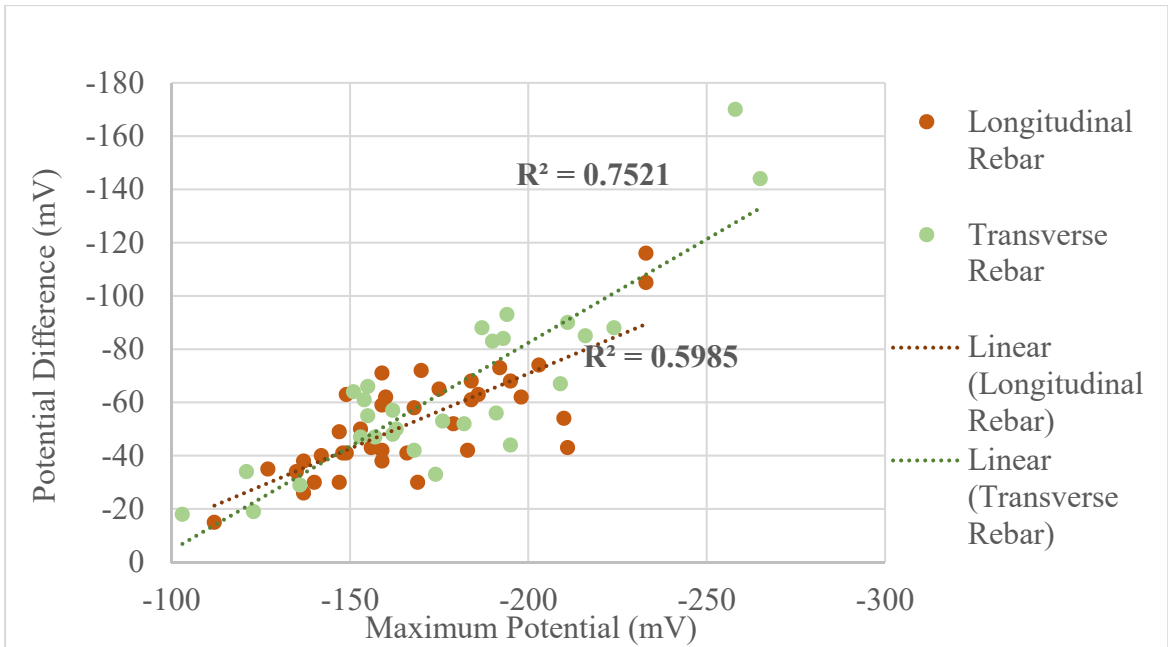
Figure 5.47: Numeric Method vs. Potential Difference for Black Rebar
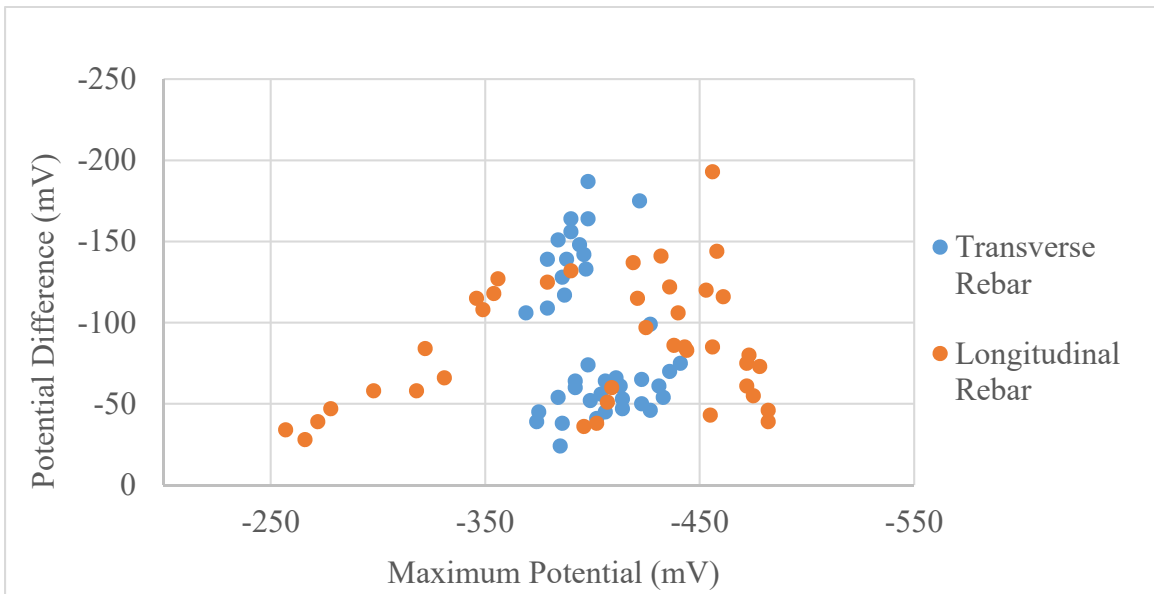
Figure 5.48: Numeric Method vs. Potential Difference for ECR

5.10.2 Influence of Resistivity on Half-Cell Potential

In order to better understand the relationship between corrosion potential of black rebar and ECR, primary influencing factors must first be assessed. The effect of resistivity on half-cell potential has been studied at length and it is known that there is an inverse relationship between the two. To observe the effects that resistivity might have had on these samples, the average bulk resistivity of the three cores obtained from a single grid box was plotted versus the average half-cell within that same box for both directions of rebar. Only non-overlay core samples were used in order to eliminate the effects observed in section 5.3.1.1. The results demonstrate the expected relationship between potential and resistivity. Therefore, it is possible that an overestimation of potential in ECR slabs and an underestimation in black rebar slabs is merely the product of the concrete resistivity. Because of this uncertainty it is even more apparent that the potential difference method would provide a better corrosion assessment, as it will eliminate variations created by concrete parameters such as resistivity.
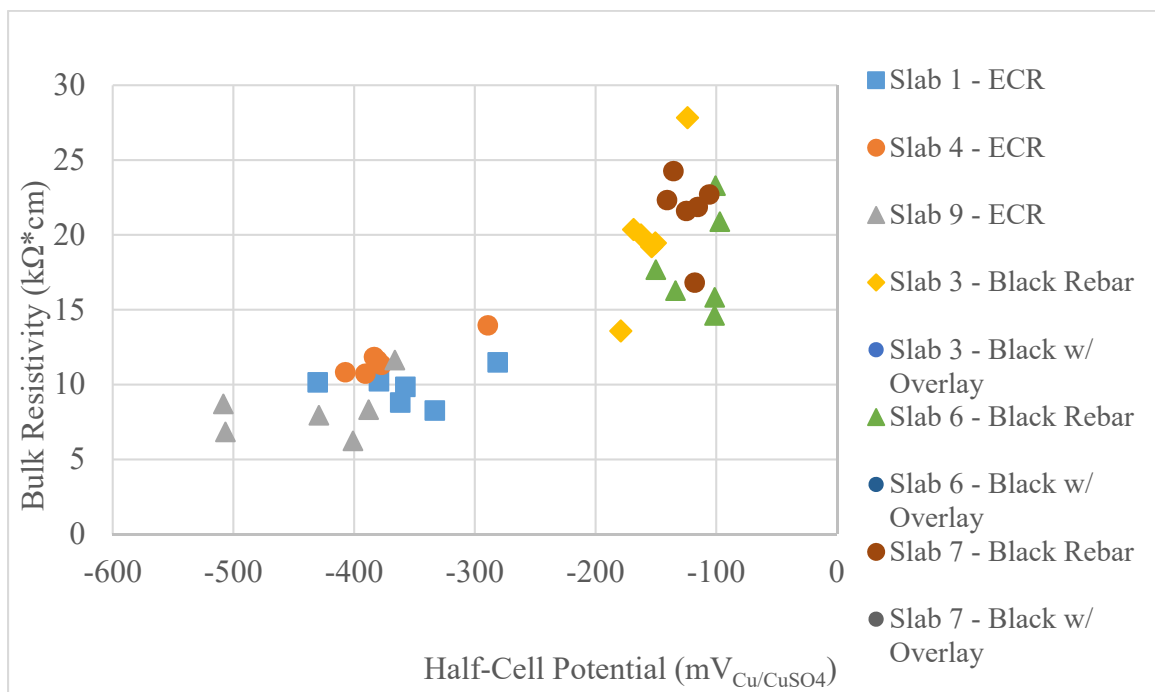
Figure 5.49: Influence of Resistivity on Half-Cell Potential

5.11 Performance Assessment of ECR and Black Rebar Using Half-Cell Potential

If the results from the half-cell potential survey are representative of the ongoing corrosion cells, then it can be expected that there also is a correlation between half-cell and mechanical properties of the surrounding concrete. Both previously discussed interpretation methods (1) cumulative frequency and (2) potential difference, will be used to identify the possibility of these correlations.

It can be observed in figure 5.50, that no correlation between the chosen corrosion levels and UPV exist. Additionally, two-way ANOVA test indicates that there are no significant differences between the corrosion levels or rebar types. Samples from black rebar slabs included both non-overlay and overlay cores as it has been determined that there are no significant differences between samples for UPV as discussed in sections 5.8.1 through 5.8.3. This indicates that while UPV is a good property for bulk quality assessment, it may not relate to corrosion for either black or epoxy-coated rebar.
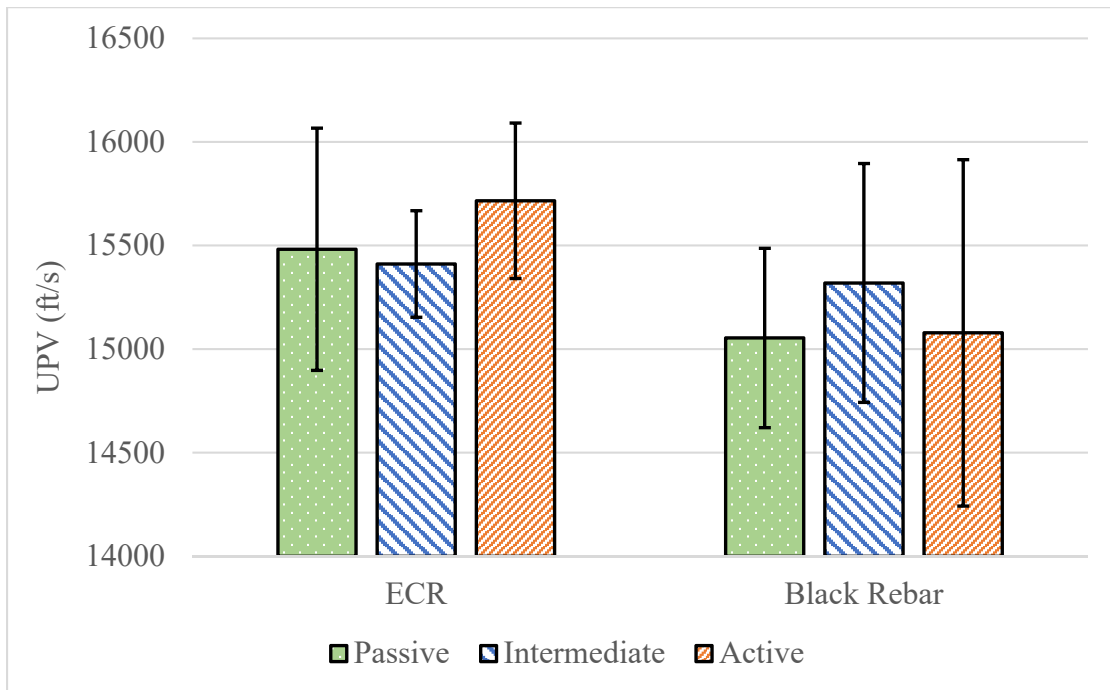
Figure 5.50: UPV of ECR and Black Rebar Based on Passive and Active Corrosion Zones Determined by Cumulative Probability

A clear distinction between rebar types is observed for bulk resistivity in figure 5.51. Samples selected for black rebar did not include the overlay samples since it was determined that there was a significant difference between overlay and non-overlay samples. A two-way ANOVA test resulted in a p-value of 0.02 between rebar types, meaning that there is a statistically significant difference for bulk resistivity among the two types of rebar. This result can be an indication of better quality bulk material in the black rebar slabs or is merely the product of a difference between material deterioration near the surface. The latter would be caused because the ECR cores were cut from the bottom and all properties will be the result of material found at the top of the slab, whereas the non-overlay samples in rebar slabs indicate properties found at least 3 inches below the slab surface.

The relationship between concrete resistivity and corrosion severity has been proven to have an inverse relationship by multiple studies. One such study presented that resistivity levels below 10 kΩcm produced a high probability of active corrosion while resistivity values above 30 kΩcm produce a low probability of corrosion (Morris et al. 2002). Using these ranges for the data presented in figure 5.51, depicts that regardless of the influence of the overlay, the black rebar slabs exhibit a much lower corrosion risk than the ECR.

The results of statistical analysis between corrosion levels did not produce significantly different results and so it can be concluded that, in this study, the bulk resistivity cannot be used as an indication for corrosion severity. However, the expected decrease in resistivity with corrosion severity is observed. This at least gives some indication that there may exist a relationship between the two, but provided the variances is not deemed statistically related.
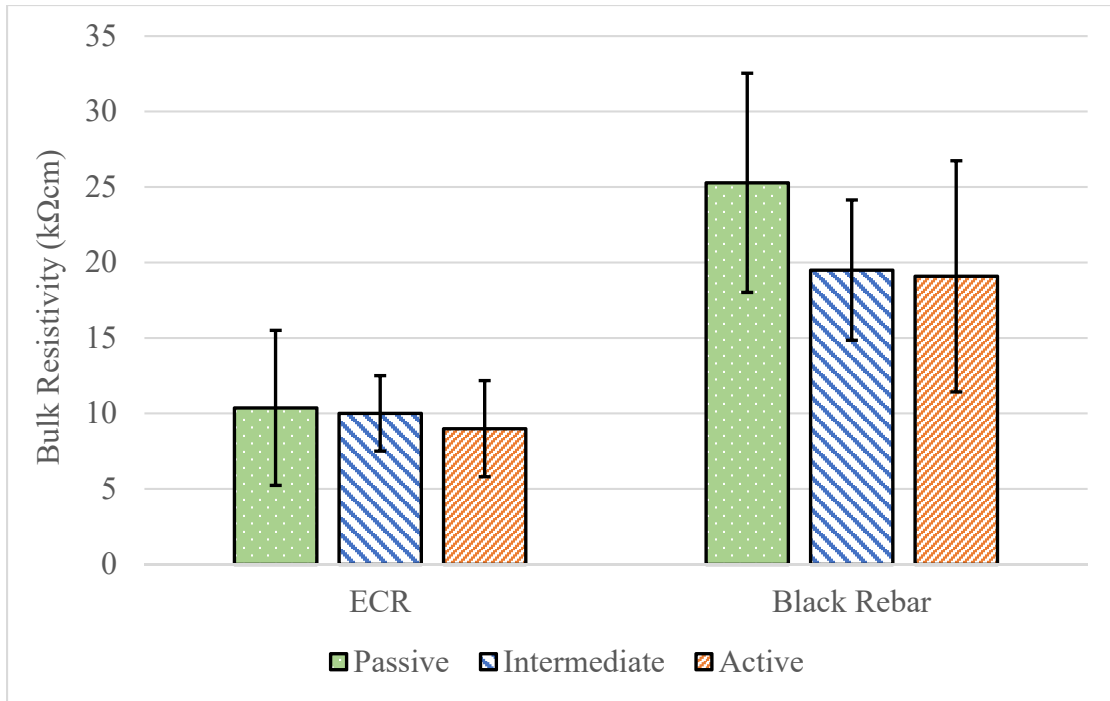
Figure 5.51: Bulk Resistivity of ECR and Black Rebar Based on Passive and Active Corrosion Zones Determined by Cumulative Probability

The comparison of static modulus of elasticity between corrosion levels and rebar types can be seen in figure 5.52. The results of two-way ANOVA indicate that neither rebar type nor corrosion level are statistically significant in regards to modulus. It would be expected that there would be an increase in modulus with an increase in corrosion severity due to the internal cracking caused by expansion, which would increase the allowable strain in the material under loading. This relationship is observed for the 'active' corrosion level in a lot of samples. The high variances for the means represented in figure 5.52, indicate that there do exist some cores with extremely high modulus in the most severe corrosion category. The cause for this may be due to the local distance to the rebar for each individual core. If a core is closer to the rebar causing the 'active' corrosion condition, then the presence of internal cracking will be more prevalent in the core properties. This means that although it is not proven statistically in this data set, there may be a correlation between modulus and corrosion severity.
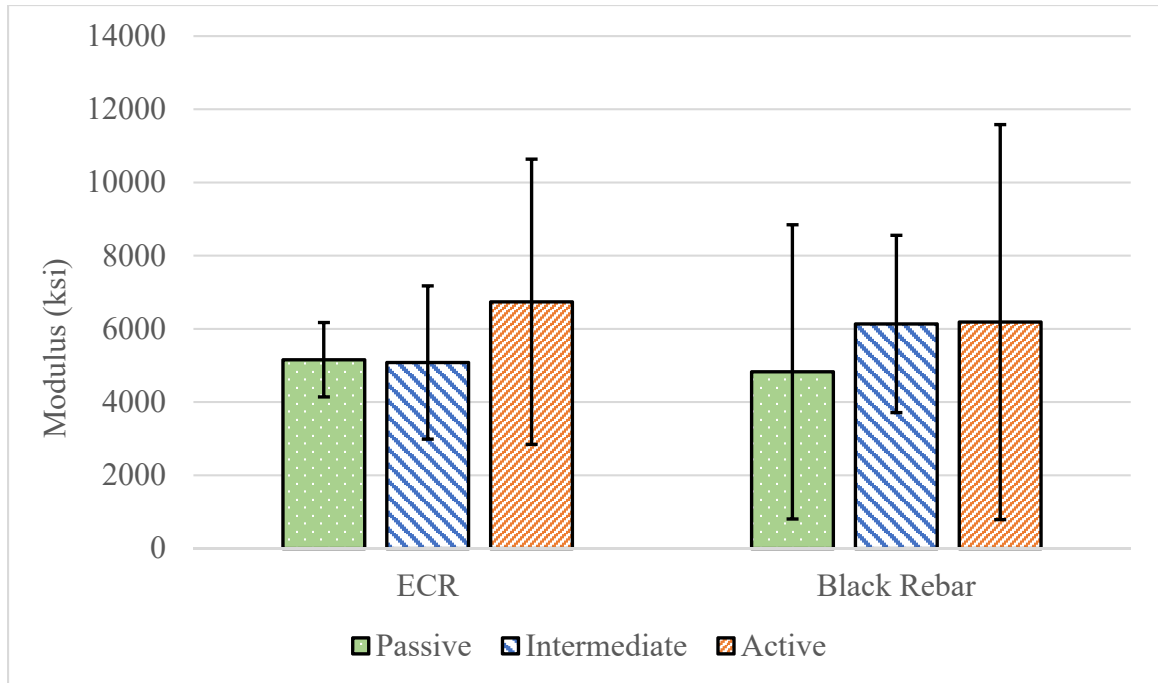
Figure 5.52: Modulus of ECR and Black Rebar Based on Passive and Active Corrosion Zones Determined by Cumulative Probability

The results of compression testing in regards to corrosion level and rebar type are shown in figure 5.53. There is an observed inverse relationship between compression strength and corrosion severity in black rebar samples, which would be the anticipated relationship. A two-way ANOVA test indicates that neither rebar type nor corrosion severity level have significantly different compression strengths. This means that there does not exist a relationship between compression strength and corrosion severity in this case. As mentioned previously, the effect of core location in regards to corrosion product may be the cause for this result. The cores were sampled in a manner, specifically avoiding rebar which in this case may be the reason for no clear evidence to back the hypothesis that corrosion will impact the compression strength of surrounding concrete.
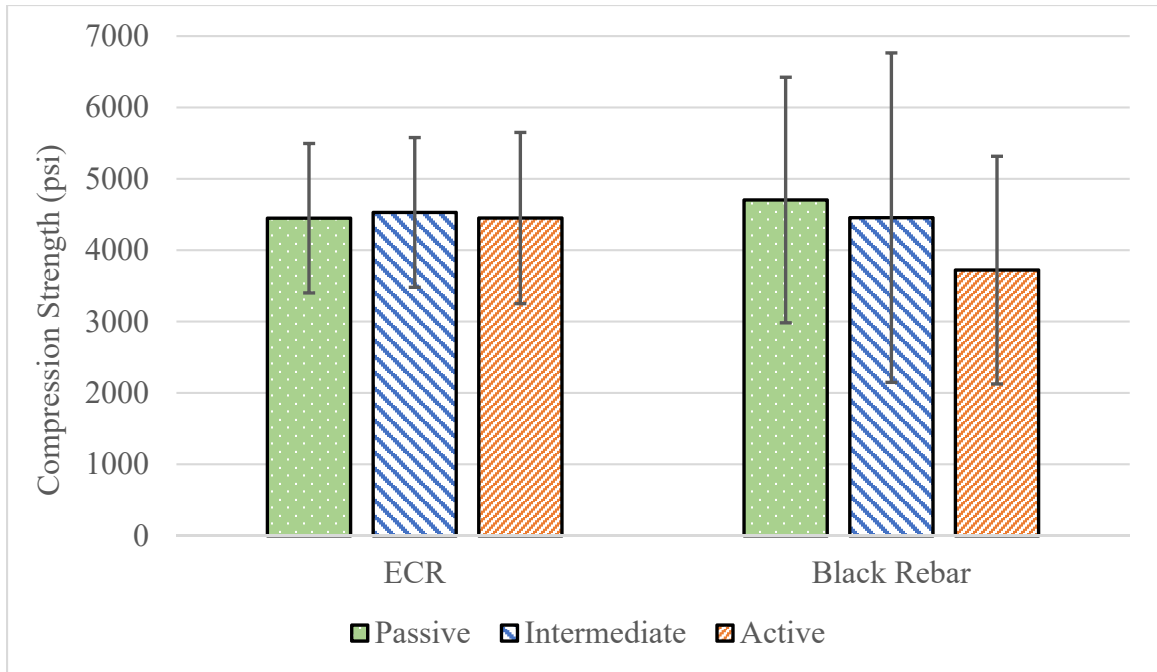
Figure 5.53: Compression Strength of ECR and Black Rebar Based on Passive and Active Corrosion Zones Determined by Cumulative Probability

These same material properties were analyzed in relation to potential difference in the 1 ft^2 area surrounding each core in question and plotted in figures 5.54, 5.55, 5.56 and 5.57. It can be observed that there is no strong linear correlation between potential difference and concrete properties in any case. This means that the use of potential difference in a small area is not a sufficient means to estimating concrete properties.
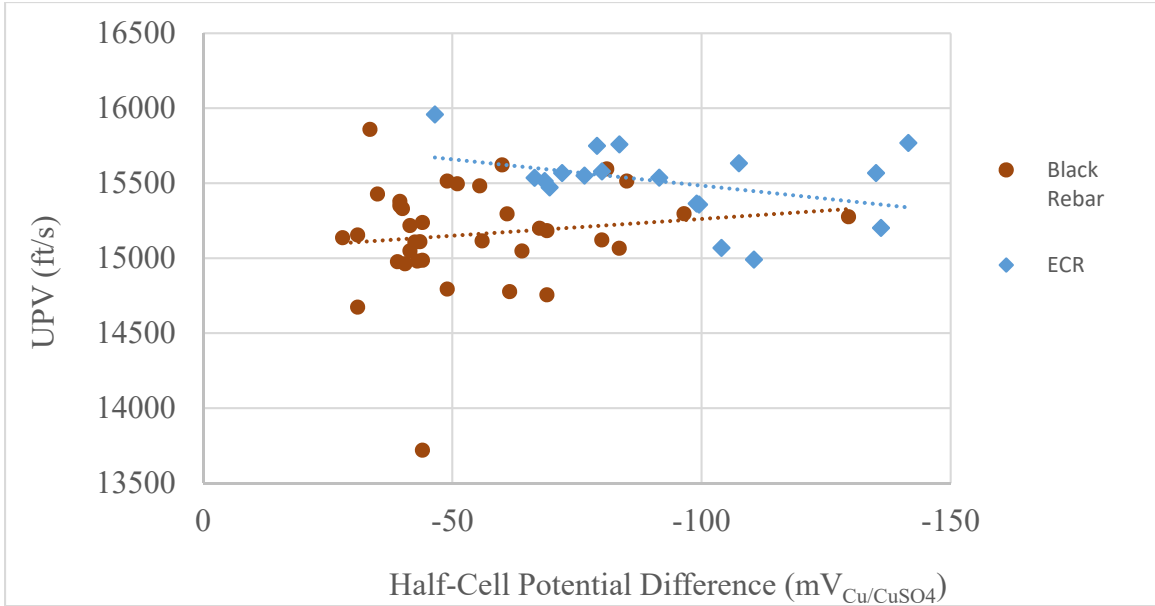
Figure 5.54: UPV of ECR and Black Rebar Based on Potential Difference Method
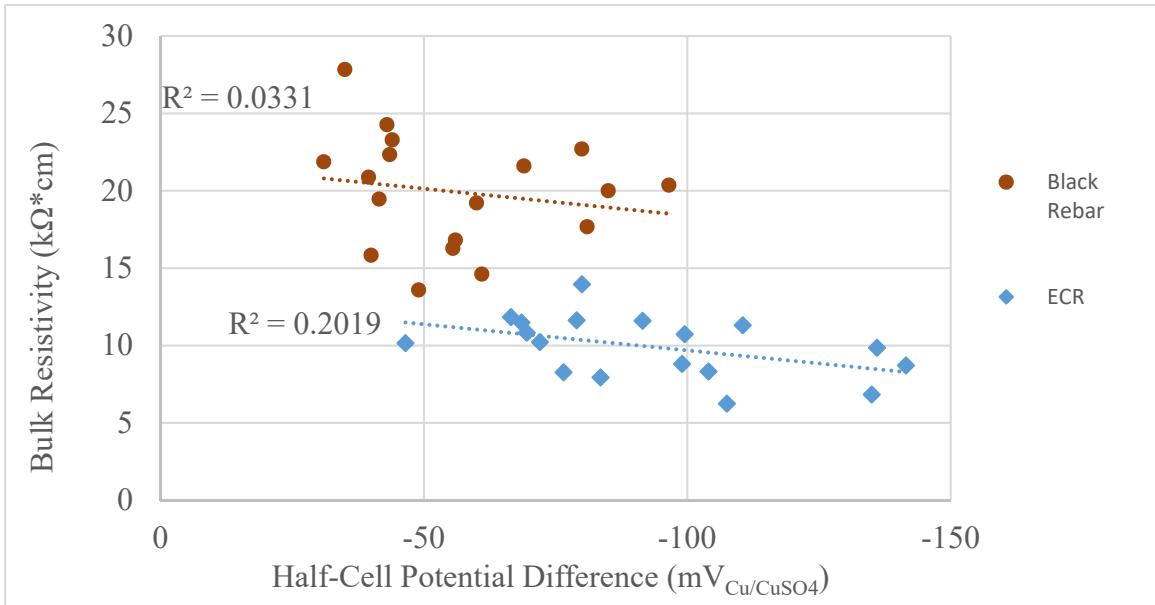
Figure 5.55: Bulk Resistivity of ECR and Black Rebar Based on Potential Difference Method
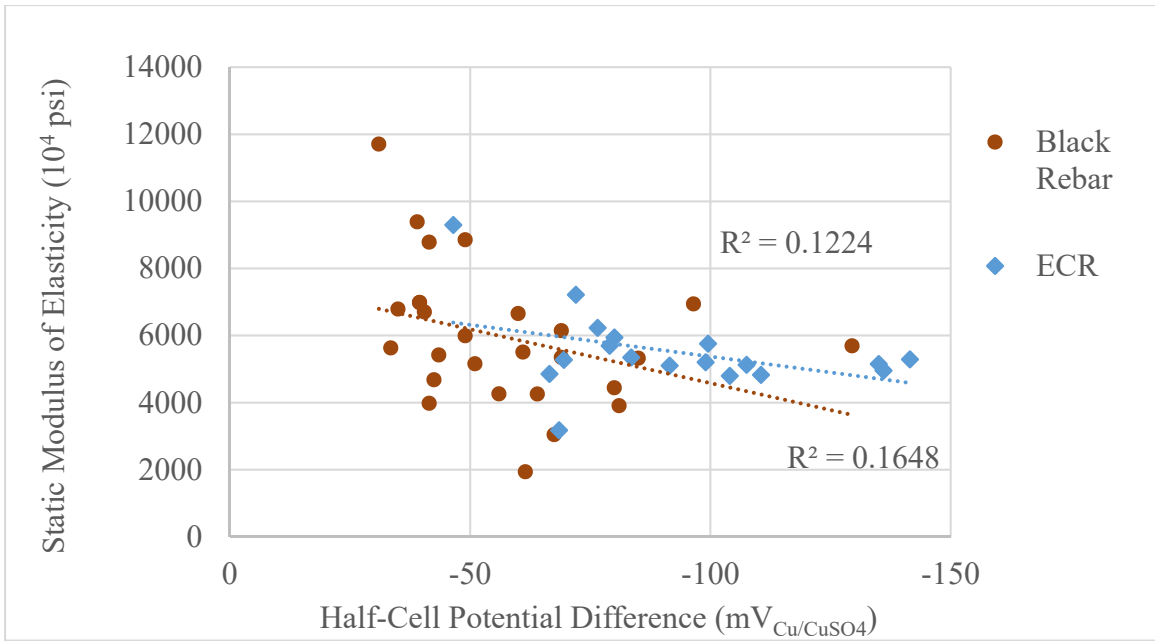
Figure 5.56: Modulus of Elasticity of ECR and Black Rebar Based on Potential Difference Method
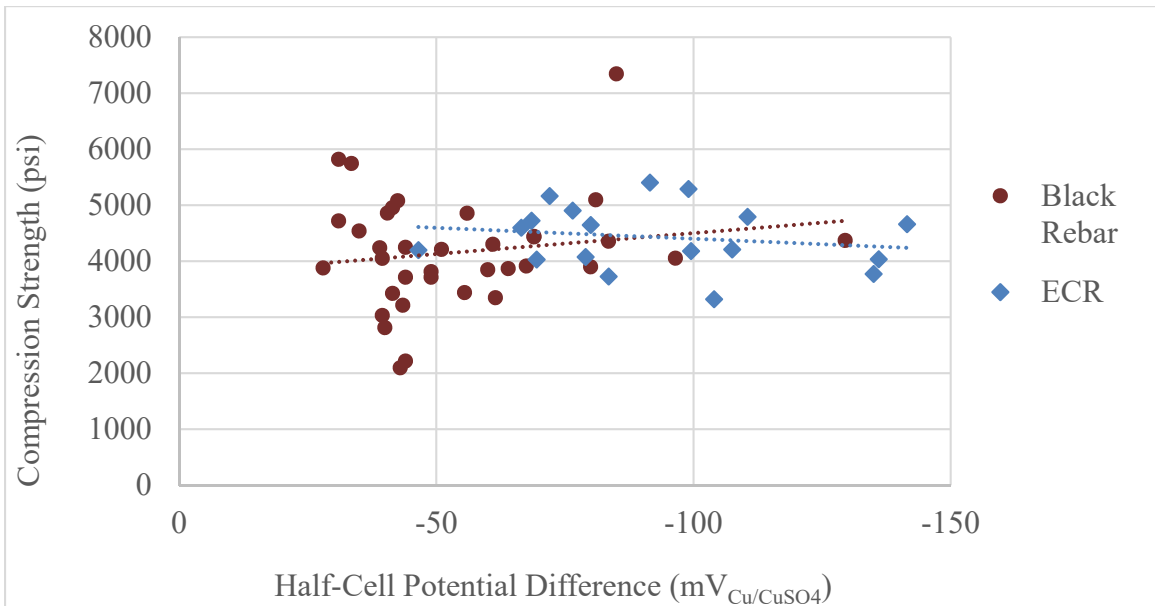
Figure 5.57: Compression Strength of ECR and Black Rebar Based on Potential Difference Method

5.12 Efficacy of Corrosion Assessment of Epoxy-Coated Rebar

The primary basis for evaluating the efficacy of NDT tests for ECR assessment is through the means of visual assessment of the rebar and classifying it into a 'corrosion severity' class. Three classes were used to represent different corrosion conditions for black rebar (1) no visible corrosion (2) visible corrosion on surface and (3) visible corrosion and loss of material. Three classes were used to represent different corrosion conditions for ECR (1) no visible corrosion, no compromise of coating (2) coating defects and visible corrosion product underneath and (3) coating defects and corrosion products visible on surrounding concrete.

Table 5.24: Corrosion Severity Index for Black Rebar

Class 1	*Class 2*	*Class3*
• *No visible corrosion*	• *Visible corrosion on surface*	• *Visible corrosion* • *corrosion product on surrounding concrete* • *loss of material*

Table 5.25: Corrosion Severity Index for ECR

Class 1	Class 2	Class 3
• *No visible corrosion* • *No coating defects*	• *Visible corrosion in defects* • *Coating defects*	• *Corrosion product on surrounding concrete* • *Debonded coating*

Comparisons between concrete material properties and NDT results on the basis of corrosion severity classification will be explored in the following subsections.

5.12.1 Half-Cell Potential Method

As section 5.1.1. discusses, the variability surrounding the differences between the numeric method and potential difference method for ECR, suggests that one method might be better than the other at assessing true corrosion severity. To assess this theory, potential values in each corrosion class were averaged and plotted in figures 5.58 and 5.59.

Both methods displayed an increase in potential with corrosion severity for both types of rebar. This is promising, since it is generally understood that half-cell potential cannot be adequately performed on ECR. This comparison also indicates the prominence of the potential difference method by resulting in a significant difference between results from class 2 and class 3. This is a critical distinction since the difference in corrosion between class 3 and class 2 is drastic, in this case. The radical difference in potential would also

decrease the likelihood of a misdiagnosis, especially since it is common practice to use a range of values to indicate corrosion probability. This interpretation technique may lead to the blending of corrosion classes in the numeric method, because the difference between classes is small, around 50 to 100 mV.
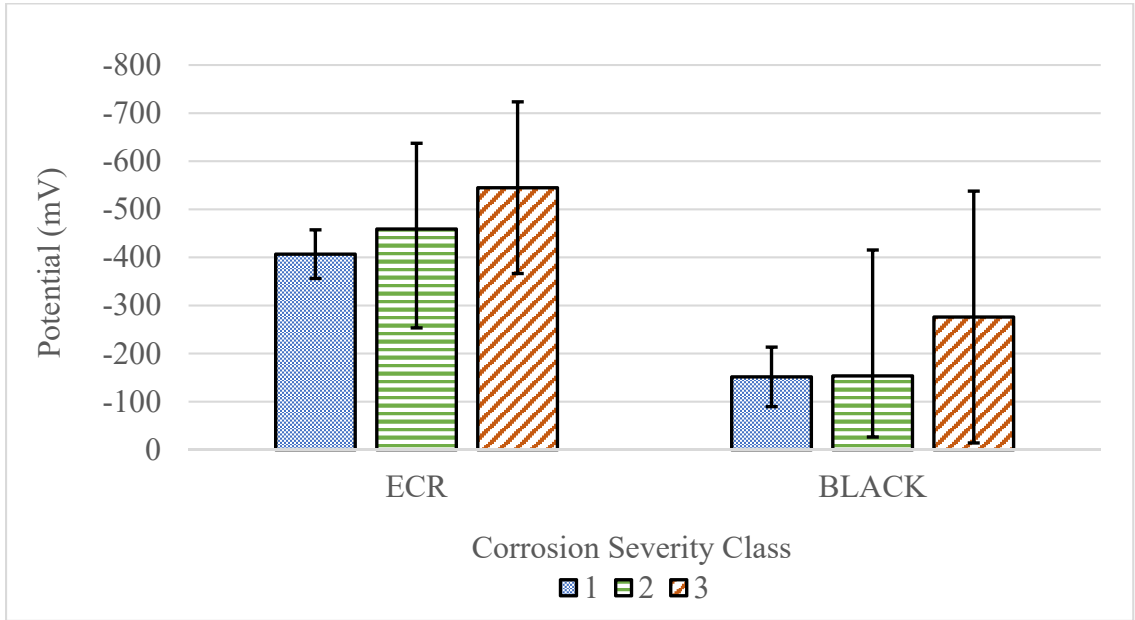
Figure 5.58: Average Potential Based on Corrosion Severity Class
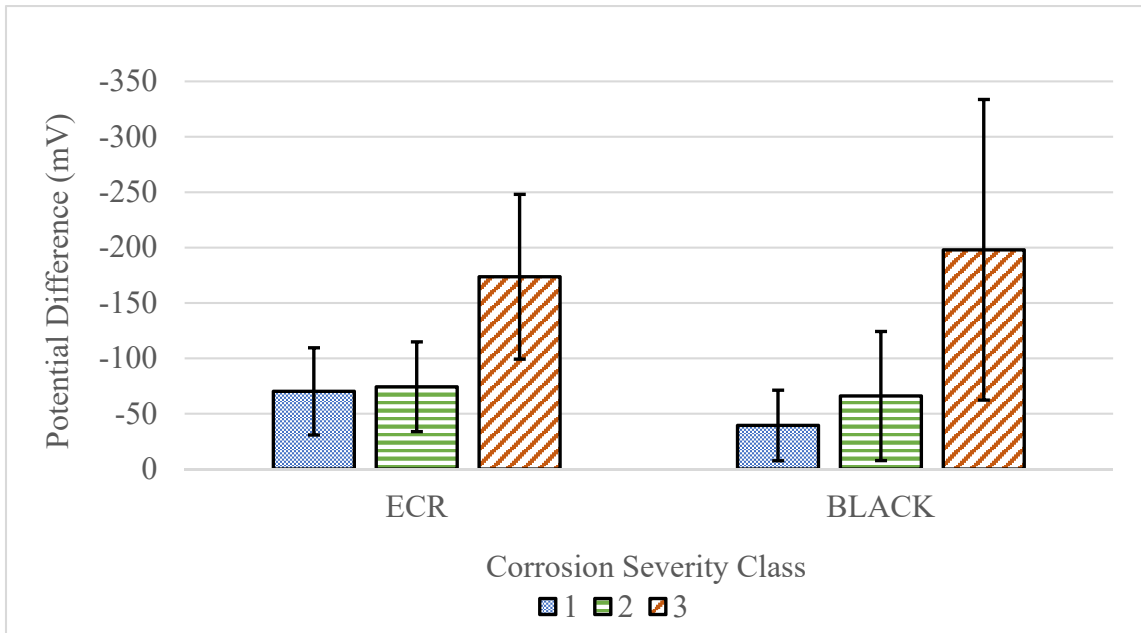
Figure 5.59: Average Potential Difference Based on Corrosion Severity Class

5.12.2 Compression Strength

In theory, the formation of corrosion products should result in micro cracking and a reduction in compression strength of the surrounding concrete material. In order to see the effect that corrosion severity has on concrete strength, an average compression strength was calculated for both ECR and black rebar and graphed according to the associated corrosion class. The linear equations derived from the RN-strength relationships were used to estimate the concrete strength at each coring location. This was necessary since these cores were split for staining purposes, thus restricting the ability to obtain an exact core compression.

Figure 5.60 indicates that the relationship holds true in this case for both types of rebar. In the case of ECR, this is extremely useful because of the strong linear relationship between RN and strength. This means that the use of the rebound hammer to aid in corrosion assessment of ECR is practical.
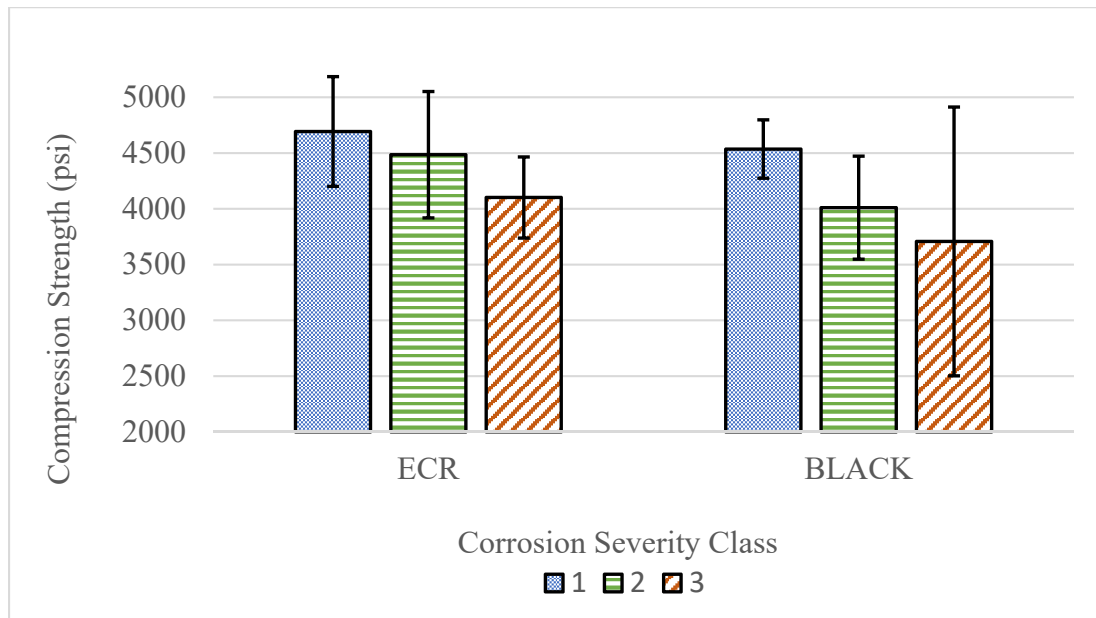
Figure 5.60: Average Compression Strength Based on Corrosion Severity Class

5.12.3 Combined NDT Method

In order to validate the process described in section 5.1 for determining coring locations, the corrosion severity class frequency was plotted in regards to 'bad' and 'good' cores. In this case, high half-cell cores were included in the bad category while low half-cell cores were included in the good category.
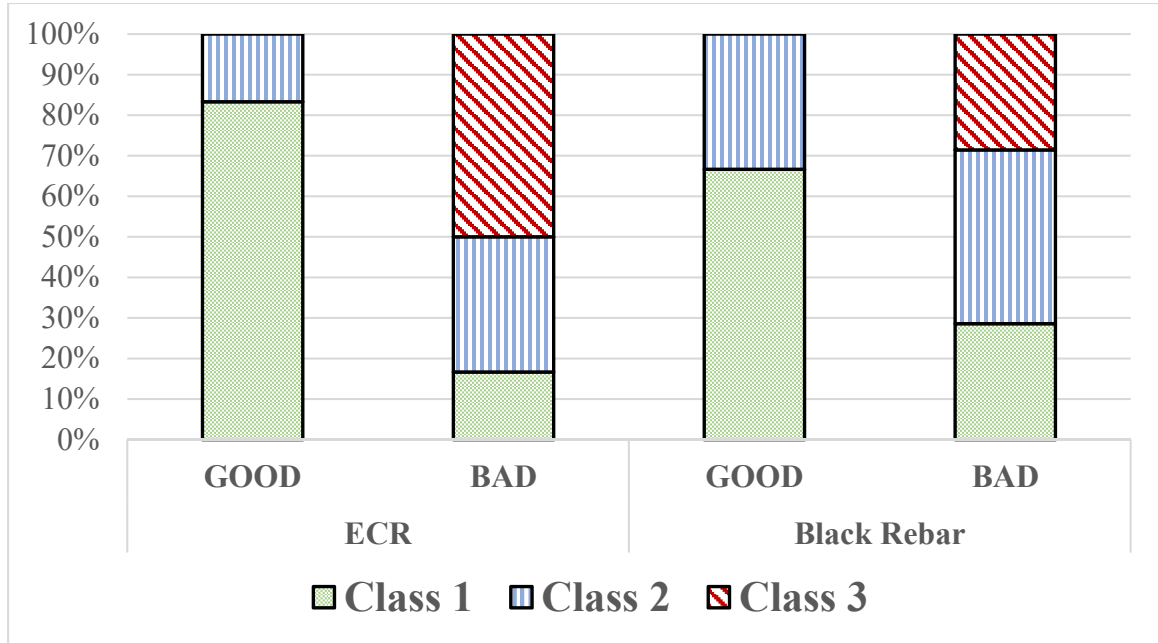
Figure 5.61: Corrosion Class Frequency for Good and Bad Cores

The results indicate proficiency in identifying high and low corrosion areas on the premise of half-cell potential, pulse echo, surface hardness and UPV. Although some samples were misdiagnosed as 'bad' it is important to note that all class 3 samples were correctly diagnosed as high-corrosion risk areas.

Although the classification of corrosion severity is on the basis of visual inspection alone, it can be stated that corrosion assessment of ECR is possible with careful evaluation of NDT results.

CHAPTER VI

CONCLUSION

The purpose of this investigation was to better understand the limitations of using nondestructive tests as a means to identify critical and non-critical areas for corrosion assessment and provide insight on the effectiveness of epoxy-coated rebar in comparison to black rebar. This included exploration of the viability of corrosion assessment using half-cell potential on ECR, which is currently regarded as unfeasible.

General conclusions derived from the results are:

1. For black rebar, the potential difference technique was more successful at identifying corrosion than the numeric technique by eliminating misinterpretations caused by external factors such as moisture condition and concrete resistivity.

2. A surface hardness survey cannot be used for estimation of mechanical properties or determination of coring locations if there is an overlay present.

3. Potential difference interpretation method is suitable for corrosion assessment of ECR when paired with visual assessment, chloride penetration analysis, and estimated compression strength.

4. The combined NDT methodology used in this study, proved to be the best method for identifying corrosion of ECR

5. The combination of visual, surface hardness, pulse-echo and half-cell potential surveys is capable of identifying high and low risk corrosion zones.

The use of only half-cell potential using the numeric technique is not suitable for corrosion assessment in either case. The inclusion of an overlay masked the effects of corrosion products seen in the black rebar slabs, despite the numeric approach suggesting that there was less than a 10% probability of corrosion at most locations. However, the numeric method becomes more reliable when analyzed using a cumulative probability distribution. The clear disadvantage of this, is that a small range of potential values can easily result in a normal distribution, thus making the decision of threshold levels difficult. Due to these factors, the potential difference technique is most reliable for corrosion assessment.

Based on the concrete mechanical properties of both rebar types and condition of the rebar, it can be concluded that the ECR did outperform the black rebar. The exception to this, is seen in the bulk resistivity and lack of chloride penetration seen in black rebar slabs. These results are presumably the effect of the application of the overlay and not indicative of the condition of the concrete as it was at the time of repair. Despite the effectiveness of the overlay, some locations produced concerning amounts of ongoing corrosion (visible, liquefied corrosion product). Even more concerning, is the fact that the overlay concealed these conditions in the half-cell potential, thus illuminating the serious need for an experienced engineer and in-depth assessment of corrosion of in-service structures.

Although ECR performed considerably better than black rebar, there should be a raised concern for the potential of macrocell formation as discussed in section 5.9.5. The results of the half-cell potential survey of ECR slabs may be indicative of macrocells occurring due to the combination of chloride contaminated concrete and uncoated black rebar in the bottom mat (Hansson et al. 2006). Structurally, the loss of rebar cross sectional area in bottom steel is not as serious, however the production of corrosion products can lead to spalling and falling debris from the underside of the bridge.

REFERENCES

Akashi, T. and Amasaki, S. (1984). "Study of the Stress Waves in the Plunger of a Rebound Hammer at the Time of Impact." ACI Spec. Publication, SP-82.

American Association of State Highway and Transportation Officials (AASHTO). (2011). "Standard Method of Test for Surface Resistivity Indication of Concrete's Ability to Resist Chloride Ion Penetration." T 358, Washington, DC.

American Concrete Institute (ACI). (2008). "Building Code Requirements for Structural Concrete and Commentary." ACI 318R-08, Farmington Hills, MI.

American Concrete Institute (ACI). (2007). "Causes, Evaluation, and Repair of Cracks in Concrete Structures." ACI 224-07, Farmington Hills, MI.

American Concrete Institute (ACI). (2019). "Guide for Evaluation of Concrete Structures Prior to Rehabilitation." ACI 364-19, Farmington Hills, MI.

American Concrete Institute (ACI). (2008). "Guide for Conducting a Visual Inspection of Concrete in Service." ACI 201.1R-08, Farmington Hills, MI.

American Concrete Institute (ACI). (2013). "Report on Nondestructive Test Methods for Evaluation of Concrete in Structures." ACI 228.2R-13, Farmington Hills, MI.

American Society for Testing and Materials (ASTM). (2019). "Standard Test Method for Bulk Electrical Resistivity or Bulk Conductivity of Concrete." ASTM C1876-19, West Conshohocken, PA.

American Society for Testing and Materials (ASTM). (2020). "Standard Test Method for Compressive Strength of Cylindrical Concrete Specimens." ASTM C39/C39M-20, West Conshohocken, PA.

American Society for Testing and Materials (ASTM). (2015). "Standard Test Method for Corrosion Potentials of Uncoated Reinforcing Steel in Concrete." ASTM C876-15, West Conshohocken, PA.

American Society for Testing and Materials (ASTM). (2017). "Standard Practice for Examination and Sampling of Hardened Concrete in Constructions." ASTM C823/C823M-12, West Conshohocken, PA.

American Society for Testing and Materials (ASTM). (2019). "Standard Test Method for Fundamental Transverse, Longitudinal, and Torsional Resonant Frequencies of Concrete Specimens." ASTM C215-19, West Conshohocken, PA.

American Society for Testing and Materials (ASTM). (2014). "Standard Test Method for Modulus of Elasticity and Poisson's Ratio of Concrete in Compression." ASTM C469/C469M-14, West Conshohocken, PA.

American Society for Testing and Materials (ASTM). (2016). "Standard Test Method for Pulse Velocity Through Concrete." ASTM C597-16, West Conshohocken, PA.

American Society for Testing and Materials (ASTM). (2018). "Standard Test Method for Rebound Number of Hardened Concrete." ASTM C805/C805M-18, West Conshohocken, PA.

American Society for Testing and Materials (ASTM). (2004). "Standard Test Method for Splitting Tensile Strength of Cylindrical Concrete Specimens." ASTM C496, West Conshohocken, PA.

Beddoe, R.E. (2010). "Determination of Chlorides in Concrete Structures." Non-Destructive Evaluation of Reinforced Concrete Structures, C. Maierhofer H. Reinhardt G. Dobmann, U.K.: Woodhead Publishing, 198-216.

Bertolini, L., Elsener, B., Pedeferri, P., and Polder, R. (2004). Corrosion of Steel in Concrete, WILEY-VCH, KGaA, Weinheim.

Breysse, D. (2010). "Deterioration Processes in Reinforced Concrete: an Overview."
Non-Destructive Evaluation of Reinforced Concrete Structures, C. Maierhofer H.
Reinhardt G. Dobmann, U.K.: Woodhead Publishing, 28-54.

Breysse, D., Soutsos, M., and Lataste, J.F. (2008). "Assessing Stiffness and Strength in
Reinforced Concrete Structures: Added Value of Combination of Non Destructive
Techniques." 1st Medachs Conf., Lisbon, 27-30.

Breysse, D., Yotte, S., Salta, M., Pereira, E., Ricardo, J., Povoa, A. (2007). "Influence of
spatial and temporal variability of the material properties on the assessment of a
RC corroded bridge in marine environment." 7th ICASP Conference, Tokyo.

Broomfield, J.P. (1994). "Assessing Corrosion Damage on Reinforced Concrete
Structures." Proc., Int. Conference, University of Sheffield, U.K., 1-25.

Broomfield, J.P. (1997). Corrosion of Steel in Concrete: Understanding, Investigation
and Repair, Chapman & Hall, New York, NY.

Cabrera, J.G. (1996). "Deterioration of Concrete Due to Reinforcement Steel Corrosion."
Cement and Concrete Composites, 18(1), 47-59.

Carino, N. J. (1999). "Nondestructive Techniques to Investigate Corrosion Status in
Concrete Structures." Journal of Performance of Constructed Facilities, 13(3), 96–
106.

Elsener, B., Andrade, C., Guilikers, J., Polder, R., and Raupach, M. (2003). "Half-Cell
Potential Measurements – Potential Mapping on Reinforced Concrete Structures."
Materials and Structures, 36(7), 461-471.

Elsener, B. and Bohni, H. (1997). "Understanding Corrosion Mechanisms of Metals in
Concrete – A Key to Improving Infrastructure Durability." Proc. Int. Conference,
MIT Cambridge, USA, 27-31.

Federal Highway Administration (FHWA). (2002). "Corrosion Costs and Preventative
Strategies in the United States." Report from CC technologies Laboratories, Inc.
FHWA and NACE, Dublin, OH.

Gu, P., and Beaudoin, J.J. (1998). "Obtaining Half-Cell Potential Measurements in Reinforced Concrete Structures." Institute for Research in Construction, 4.

Hansson, C.M., Poursaee, A., and Laurent, A. (2006). "Macrocell and Microcell Corrosion of Steel in Ordinary Portland Cement and High Performance Concretes." Cement and Concrete Research, 36(11), 2098-2102.

Hellier, C.J. (2001). Handbook of Nondestructive Evaluation, McGraw-Hill, New York, NY.

Jones, R. (1954). "Testing of Concrete by an Ultrasonic Pulse Technique." RILEM Int. Symp. on Nondestructive Testing Materials and Structures, RILEM, Paris, 137.

Jones, R. and Facaoaru, I. (1969). "Recommendations for Testing Concrete by the Ultrasonic Pulse Method." Mater. Struct. Res. Testing, 2(19), 275.

Kolek, J. (1969). "Non-destructive Testing of Concrete by Hardness Methods." Proc. Symp. on Non-destructive Testing of Concrete and Timber, Institution of Civil Engineers, London, 15.

Layssi, H., Ghods, P., Alizadeh, A. R., and Salehi, M. (2015). "Electrical Resistivity of Concrete." ACI, 37(5), 41-46.

Malhotra, V. M. and Carino, N.J. (2004). *Handbook on Nondestructive Testing of Concrete,* CRC Press LLC, Boca Raton, FL.

Meng, D., Lin, S., and Azari, H. (2020). "Nondestructive Corrosion Evaluation of Reinforced Concrete Bridge Decks with Overlays: An Experimental Study." *Journal of Testing and Evaluation,* 48(1), 516-537.

Mitchell, M., R. & Yu, Myoung-Youl & Lee, Jae-Yong & Chung, Chul-Woo. (2010). "The Application of Various Indicators for the Estimation of Carbonation and pH of Cement Based Materials." *JTE*, 38.

Morris, W., Vico, A., Vazquez, M., and Sanchez, S.R. (2002). "Corrosion of Reinforcing Steel Evaluated by Means of Concrete Resistivity Measurements." *Corrosion Science,* 44(1), 81-99.

Oudar, J. and Marcus, P. (1995). *Corrosion Mechanisms in Theory and Practice,* Marcel Dekker, Inc., New York, NY.

Raupach, M., Reichling, K., Broomfield, J., Gulikers, J., Schneck, U., Serdar, M., and Pepenar, I. (2013). "Inspection Strategies for Reinforcement Corrosion Surveys." *Materials and Corrosion,* 64(2), 111-115.

Real, L. V., Oliveira, D. R. B., Soares, T., and Medeiros, F. (2015). "AgNO3 Spray Method for Measurement of Chloride Penetration: the State of Art." *ALCONPAT Journal,* 5(2), 141-151.

Sadowski, L. (2013). "Methodology for Assessing the Probability of Corrosion in Concrete Structures on the Basis of Half-Cell Potential and Concrete Resistivity Measurements." *The Scientific World Journal,* 2013, 1-8.

Shaikh, F. U. A. (2018). "Effect of Cracking on Corrosion of Steel in Concrete." *Int. Journal of Concrete Structures and Materials,* 12(1), 3.

Shreir, L.L., Jarman, R.A., and Burstein, G.T. (1994). *Corrosion: Metal/Environment Reactions,* Butterworth-Heinemann Ltd, Oxford.

Toongoenthong, K and Maekawa, K. (2005). "Simulation of Coupled Corrosive Product Formation, Migration into Crack and Propagation in Reinforced Sections." *Journal of Advanced Concrete Technology,* 3(2), 253-265.

Tran, K. K., Nakamura, H., Kawamura, K., and Kunieda, M. (2011). "Analysis of Crack Propagation Due to Rebar Corrosion Using RBSM." *Cement and Concrete Composites,* 33(9), 906-917.

Val, D., Chernin, L., and Stewart, M. (2009). "Experimental and Numerical Investigation of Corrosion-Induced Cover Cracking in Reinforced Concrete Structures." *Journal of Structural Engineering,* 135(4), 376-385.

Vries, J. (1997). "Hydrophobic Treatment of Concrete." *Construction and Building Materials,* 11(4), 259-265.

Yodsudjai, W. and Pattarakittam, T. (2017). "Factors Influencing Half-Cell Potential Measurements and its Relationship with Corrosion Level." *Measurement,* 104(2017), 159-168.

Zoldners, N.G. (1957). "Calibration and Use of Impact Test Hammer." *ACI Journal Proc.,* 54(2), 161.

Zou, Z. H., Wu, J., Wang, Z., & Wang, Z. (2016). "Relationship Between Half-Cell Potential and Corrosion Level of Rebar in Concrete." *Corrosion Engineering, Science and Technology*, 51(8), 588–595.

APPENDICES

Appendix A

Table A.1 Results Ultrasonic Pulse Velocity - Slab 3

Core Sample Set (RN)	Average (ft/s)	Standard Deviation (ft/s)	Coefficient of Variation (%)	Average (ft/s)	Relative Range (%)	Anova (ρ)
No Overlay						
34	15296	254	1.7	15432	7.1	4.50E-01
36	15514	228	1.5			
38	15514	97	0.6			
39	15217	152	1.0			
40	15622	450	2.9			
41	15428	233	1.5			
With Overlay						
34	14986	56	0.4	14991	4.8	3.25E-01
36	14777	179	1.2			
38	15066	310	2.1			
39	15048	82	0.5			
40	14962	110	0.7			
41	15107	199	1.3			

Table A.2 Results Bulk Electrical Resistivity - Slab 3

Core Sample Set (RN)	Average (kO*cm)	Standard Deviation (kO*cm)	Coefficient of Variation (%)	Average (kO*cm)	Relative Range (%)	Anova (ρ)
No Overlay						
34	20.4	3.0	14.8	20.1	94.0	4.05E-03
36	13.6	4.8	35.2			
38	20.0	2.2	11.2			
39	19.5	3.2	16.3			
40	19.2	1.3	6.5			
41	27.8	3.1	11.1			
With Overlay						
34	131.8	103.1	78.2	161.8	146.8	5.64E-01
36	194.5	32.9	16.9			
38	141.2	80.2	56.8			
39	219.1	54.4	24.9			
40	159.4	91.5	57.4			
41	124.5	43.4	34.9			

Table A.3 Results Dynamic Modulus of Elasticity - Slab 3

Core Sample Set (RN)	Average (ksi)	Standard Deviation (ksi)	Coefficient of Variation (%)	Average (ksi)	Relative Range (%)	Anova (ρ)
No Overlay						
34	12295	1291	10.5			
36	12852	647	5.0			
38	12918	515	4.0			
39	12080	174	1.4			
40	12399	1293	10.4			
41	13178	48	0.4	12620	20.7	5.71E-01
With Overlay						
34	11673	449	3.8			
36	11683	619	5.3			
38	13233	930	7.0			
39	12593	448	3.6			
40	11833	332	2.8			
41	12554	325	2.6	12262	26.1	2.56E-02

Table A.4 Results Static Modulus of Elasticity - Slab 3

Core Sample Set (RN)	Average (ksi)	Standard Deviation (ksi)	Coefficient of Variation (%)	Average (ksi)	Relative Range (%)	Anova (ρ)
No Overlay						
34	6810	501	7.4			
36	6138	287	4.7			
38	5382	435	8.1			
39	8784	200	2.3			
40	6657	488	7.3			
41	6582	110	1.7	6725	59.6	2.94E-06
With Overlay						
34	-	-	-			
36	1940	305	15.7			
38	-	-	-			
39	4363	440	10.1			
40	6650	335	5.0			
41	4681	73	1.6	4409	120.8	7.50E-07

Table A.5 Results Compressive Strength - Slab 3

Core Sample Set (RN)	Average (psi)	Standard Deviation (psi)	Coefficient of Variation (%)	Average (psi)	Relative Range (%)	Anova (ρ)
No Overlay						
34	4055	1605	39.6			
36	3714	956	25.7			
38	6667	1259	18.9			
39	4958	1498	30.2			
40	3849	269	7.0			
41	4541	487	10.7	4631	111.4	6.35E-02
With Overlay						
34	5163	1585	30.7			
36	3348	96	2.9			
38	5053	1892	37.4			
39	3868	52	1.3			
40	4860	1713	35.2			
41	5079	1603	31.6	4562	89.7	5.10E-01

Appendix B

Table B.1 Results Ultrasonic Pulse Velocity - Slab 6

Core Sample Set (RN)	Average (ft/s)	Standard Deviation (ft/s)	Coefficient of Variation (%)	Average (ft/s)	Relative Range (%)	Anova (ρ)
No Overlay						
30	15379	19	0.1			
32	15331	540	3.5			
34	15595	392	2.5			
37	15482	332	2.1			
39	13720	3158	23.0			
41	15295	276	1.8	15119	39.5	5.24E-01
With Overlay						
30	15350	419	2.7			
32	14794	389	2.6			
34	15199	109	0.7			
37	15049	360	2.4			
39	15238	212	1.4			
41	14976	229	1.5	15101	8.2	3.30E-01

Table B.2 Results Bulk Electrical Resistivity - Slab 6

Core Sample Set (RN)	Average (kO*cm)	Standard Deviation (kO*cm)	Coefficient of Variation (%)	Average (kO*cm)	Relative Range (%)	Anova (ρ)
No Overlay						
30	20.9	3.2	15.5			
32	15.8	0.6	3.6			
34	17.7	4.5	25.7			
37	16.3	2.7	16.5			
39	23.3	5.2	22.5			
41	14.6	0.6	4.4	18.1	88.7	5.49E-02
With Overlay						
30	85.5	70.7	82.7			
32	62.8	18.9	30.1			
34	173.8	46.2	26.6			
37	96.0	48.8	50.8			
39	84.5	4.3	5.1			
41	123.4	13.8	11.1	104.3	158.5	6.94E-02

Table B.3 Results Dynamic Modulus of Elasticity - Slab 6

Core Sample Set (RN)	Average (ksi)	Standard Deviation (ksi)	Coefficient of Variation (%)	Average (ksi)	Relative Range (%)	Anova (ρ)
No Overlay						
30	8973	4385	48.9			
32	11425	2048	17.9			
34	11778	1172	10.0			
37	12558	512	4.1			
39	7229	5203	72.0			
41	10908	304	2.8	10478	107.9	3.01E-01
With Overlay						
30	11787	640	5.4			
32	11110	1076	9.7			
34	12054	1134	9.4			
37	11174	1241	11.1			
39	12022	240	2.0			
41	12272	736	6.0	11736	29.5	5.39E-01

Table B.4 Results Static Modulus of Elasticity - Slab 6

Core Sample Set (RN)	Average (ksi)	Standard Deviation (ksi)	Coefficient of Variation (%)	Average (ksi)	Relative Range (%)	Anova (ρ)
No Overlay						
30	6983	432	6.2			
32	-	-	-			
34	3908	259	6.6			
37	2473	1009	40.8			
39	-	-	-			
41	5505	23	0.4	4717	125.3	5.41E-05
With Overlay						
30	6983	432	6.2			
32	8852	167	1.9			
34	3043	2207	72.5			
37	3980	141	3.5			
39	-	-	-			
41	9387	2278	24.3	6449	165.6	8.39E-04

Table B.5 Results Compressive Strength - Slab 6

Core Sample Set (RN)	Average (psi)	Standard Deviation (psi)	Coefficient of Variation (%)	Average (psi)	Relative Range (%)	Anova (ρ)
No Overlay						
30	2257	1365	60.5			
32	2814	356	12.7			
34	4322	2439	56.4			
37	3440	654	19.0			
39	2217	493	22.3			
41	4302	1297	30.1	3225	199.2	2.37E-01
With Overlay						
30	4050	1154	28.5			
32	4678	1495	32.0			
34	4010	165	4.1			
37	3425	970	28.3			
39	3714	483	13.0			
41	4241	1317	31.0	4020	94.6	7.60E-01

Appendix C

Table C.1 Results Ultrasonic Pulse Velocity - Slab 7

Core Sample Set	Average (ft/s)	Standard Deviation (ft/s)	Coefficient of Variation (%)	Average (ft/s)	Relative Range (%)	Anova (ρ)
With Overlay						
33	15136	379	2.5			
35	15496	500	3.2			
37	15276	324	2.1			
39	15154	588	3.9			
41	15859	481	3.0			
43	15183	45	0.3	15351	11.4	3.30E-01
No Overlay						
33	15121	513	3.4			
35	14673	276	1.9			
37	14981	414	2.8			
39	15110	789	5.2			
41	15115	440	2.9			
43	14755	339	2.3	14959	10.1	5.24E-01

Table C.2 Results Bulk Electrical Resistivity - Slab 7

Core Sample Set	Average (kΩ*cm)	Standard Deviation (kΩ*cm)	Coefficient of Variation (%)	Average (kΩ*cm)	Relative Range (%)	Anova (ρ)
With Overlay						
33	193.3	35.2	18.2			
35	130.8	15.9	12.2			
37	126.9	39.7	31.3			
39	117.4	31.8	27.1			
41	73.2	32.9	45.0			
43	112.7	48.6	43.1	125.7	149.7	6.94E-02
No Overlay						
33	22.7	4.2	18.3			
35	21.9	4.9	22.5			
37	24.3	3.1	12.7			
39	22.3	5.4	24.3			
41	16.8	1.0	5.7			
43	21.6	3.3	15.1	21.6	59.0	5.49E-02

Table C.3 Results Dynamic Modulus of Elasticity - Slab 7

Core Sample Set	Average (ksi)	Standard Deviation (ksi)	Coefficient of Variation (%)	Average (ksi)	Relative Range (%)	Anova (ρ)
With Overlay						
33	12260	377	3.1			
35	12427	686	5.5			
37	12196	350	2.9			
39	13021	673	5.2			
41	13431	661	4.9			
43	12255	117	1.0	12598	17.3	5.39E-01
No Overlay						
33	12375	273	2.2			
35	11896	323	2.7			
37	11979	410	3.4			
39	12376	1012	8.2			
41	12757	132	1.0			
43	11818	250	2.1	12200	15.9	3.01E-01

Table C.4 Results Static Modulus of Elasticity - Slab 7

Core Sample Set	Average (ksi)	Standard Deviation (ksi)	Coefficient of Variation (%)	Average (ksi)	Relative Range (%)	Anova (ρ)
With Overlay						
33	-	-	-			
35	5156	914	17.7			
37	5690	37	0.7			
39	11708	2348	20.1			
41	5632	227	4.0			
43	4259	110	2.6	6489	151.9	7.98E-05
No Overlay						
33	4441	141	3.2			
35	-	-	-			
37	-	-	-			
39	5420	688	12.7			
41	4259	110	2.6			
43	6146	65	1.1	5067	39.9	6.06E-04

Table C.5 Results Compressive Strength - Slab 7

Core Sample Set	Average (psi)	Standard Deviation (psi)	Coefficient of Variation (%)	Average (psi)	Relative Range (%)	Anova (ρ)
With Overlay						
33	4928	2017	40.9			
35	4861	1198	24.7			
37	4370	651	14.9			
39	4719	409	8.7			
41	5745	1418	24.7			
43	4435	688	15.5	4843	86.4	7.60E-01
No Overlay						
33	3901	603	15.5			
35	5820	492	8.5			
37	3258	2143	65.8			
39	3214	631	19.6			
41	4856	243	5.0			
43	4444	1161	26.1	4249	117.4	8.17E-02

Appendix D

Table D.1 Results Ultrasonic Pulse Velocity - Slab 1

Core Sample Set	Average (ft/s)	Standard Deviation (ft/s)	Coefficient of Variation (%)	Average (ft/s)	Relative Range (%)	Anova (ρ)
No Overlay						
46	15202	69	0.45	15527	5.7	5.13E-03
48	15959	54	0.34			
50	15515	146	0.94			
52	15551	199	1.28			
54	15568	325	2.09			
56	15365	131	0.85			

Table D.1 Results Bulk Electrical Resistivity - Slab 1

Core Sample Set	Average (kΩ*cm)	Standard Deviation (kΩ*cm)	Coefficient of Variation (%)	Average (kΩ*cm)	Relative Range (%)	Anova (ρ)
No Overlay						
46	9.9	0.3	3.4	9.8	92.9	4.77E-01
48	10.2	1.4	13.7			
50	11.5	1.6	14.3			
52	8.3	4.2	50.8			
54	10.2	1.2	11.7			
56	8.8	0.4	4.8			

Table D.3 Results Dynamic Modulus of Elasticity – Slab 1

Core Sample Set	Average (ksi)	Standard Deviation (ksi)	Coefficient of Variation (%)	Average (ksi)	Relative Range (%)	Anova (ρ)
No Overlay						
34	11370	309	2.7	12043	20.7	1.13E-03
36	13255	332	2.5			
38	11911	407	3.4			
39	12103	569	4.7			
40	12037	261	2.2			
41	11583	363	3.1			

Table D.4 Results Static Modulus of Elasticity – Slab 1

Core Sample Set	Average (ksi)	Standard Deviation (ksi)	Coefficient of Variation (%)	Average (ksi)	Relative Range (%)	Anova (ρ)
No Overlay						
46	4956	86	1.7	6076	97.3	3.92032E-07
48	9296	299	3.2			
50	3883	180	4.6			
52	6107	1144	18.7			
54	7106	424	6.0			
56	5105	37	0.7			

Table D.5 Results Compressive Strength – Slab 1

Core Sample Set	Average (psi)	Standard Deviation (psi)	Coefficient of Variation (%)	Average (psi)	Relative Range (%)	Anova (ρ)
No Overlay						
46	4036	802.02	19.9	4784	66.7	7.23E-01
48	4199	604.44	14.4			
50	5106	1561.34	30.6			
52	4906	879.67	17.9			
54	5167	1610.20	31.2			
56	5292	1488.53	28.1			

Appendix E

Table E.1 Results Ultrasonic Pulse Velocity - Slab 4

Core Sample Set	Average (ft/s)	Standard Deviation (ft/s)	Coefficient of Variation (%)	Average (ft/s)	Relative Range (%)	Anova (ρ)
No Overlay						
50	15358	215	1.40	15412	12.1	4.61E-01
52	15472	297	1.92			
53	15536	473	3.04			
54	15579	102	0.65			
55	14991	677	4.52			
57	15537	225	1.45			

Table E.2 Results Bulk Electrical Resistivity - Slab 4

Core Sample Set	Average (kΩ*cm)	Standard Deviation (kΩ*cm)	Coefficient of Variation (%)	Average (kΩ*cm)	Relative Range (%)	Anova (ρ)
No Overlay						
50	10.7	0.9	8.5	11.7	44.0	1.64E-03
52	10.8	0.7	6.7			
53	11.8	0.2	1.9			
54	14.0	0.8	5.8			
55	11.3	0.6	5.0			
57	11.6	0.9	7.6			

Table E.3 Results Dynamic Modulus of Elasticity - Slab 4

Core Sample Set	Average (ksi)	Standard Deviation (ksi)	Coefficient of Variation (%)	Average (ksi)	Relative Range (%)	Anova (ρ)
No Overlay						
50	11605	20	0.2	11864	21.3	9.89E-01
52	11876	701	5.9			
53	11891	639	5.4			
54	11814	1440	12.2			
55	12032	598	5.0			
57	11965	657	5.5			

Table E.4 Results Static Modulus of Elasticity - Slab 4

Core Sample Set	Average (ksi)	Standard Deviation (ksi)	Coefficient of Variation (%)	Average (ksi)	Relative Range (%)	Anova (ρ)
No Overlay						
50	5378	246	4.6	5230	39.6	0.084582671
52	5277	70	1.3			
53	4856	445	9.2			
54	5999	136	2.3			
55	4767	90	1.9			
57	5104	1047	20.5			

Table E.5 Results Compressive Strength - Slab 4

Core Sample Set	Average (psi)	Standard Deviation (psi)	Coefficient of Variation (%)	Average (psi)	Relative Range (%)	Anova (ρ)
No Overlay						
50	4184	1308.700559	31.3	4517	97.3	8.01E-01
52	4030	194.8230364	4.8			
53	4600	1261.720777	27.4			
54	4093	1236.534255	30.2			
55	4793	1473.146278	30.7			
57	5406	2002.423847	37.0			

Appendix F

Table F.1 Results Ultrasonic Pulse Velocity - Slab 9

Core Sample Set	Average (ft/s)	Standard Deviation (ft/s)	Coefficient of Variation (%)	Average (ft/s)	Relative Range (%)	Anova (ρ)
No Overlay						
50	15069	304	2.02	15591	8.7	1.49E-01
51	15568	208	1.34			
53	15759	415	2.63			
55	15633	290	1.86			
57	15769	339	2.15			
59	15750	369	2.34			

Table F.2 Results Bulk Electrical Resistivity - Slab 9

Core Sample Set	Average (kΩ*cm)	Standard Deviation (kΩ*cm)	Coefficient of Variation (%)	Average (kΩ*cm)	Relative Range (%)	Anova (ρ)
No Overlay						
50	8.3	0.8	9.6	8.3	84.6	4.54E-04
51	6.8	0.6	8.8			
53	8.0	1.4	18.2			
55	6.2	0.7	10.9			
57	8.7	0.6	6.7			
59	11.6	1.5	12.6			

Table F.3 Results Dynamic Modulus of Elasticity - Slab 9

Core Sample Set	Average (ksi)	Standard Deviation (ksi)	Coefficient of Variation (%)	Average (ksi)	Relative Range (%)	Anova (ρ)
No Overlay						
50	11488	262	2.3	11298	46.9	2.61E-01
51	10110	2247	22.2			
53	12185	628	5.2			
55	10323	1949	18.9			
57	12123	87	0.7			
59	11557	335	2.9			

Table F.4 Results Static Modulus of Elasticity - Slab 9

Core Sample Set	Average (ksi)	Standard Deviation (ksi)	Coefficient of Variation (%)	Average (ksi)	Relative Range (%)	Anova (ρ)
No Overlay						
50	4692	930	19.8	5230	57.3	0.7563858
51	5153	495	9.6			
53	5349	1533	28.7			
55	5131	514	10.0			
57	5356	321	6.0			
59	5699	60	1.1			

Table F.5 Results Compressive Strength - Slab 9

Core Sample Set	Average (psi)	Standard Deviation (psi)	Coefficient of Variation (%)	Average (psi)	Relative Range (%)	Anova (ρ)
No Overlay						
50	4120	1388.648157	33.7	3967	94.2	2.54E-01
51	4389	1373.694189	31.3			
53	2781	885.8166819	31.8			
55	3982	433.0269084	10.9			
57	4663	220.4884937	4.7			
59	3869	360.2117077	9.3			

Appendix G
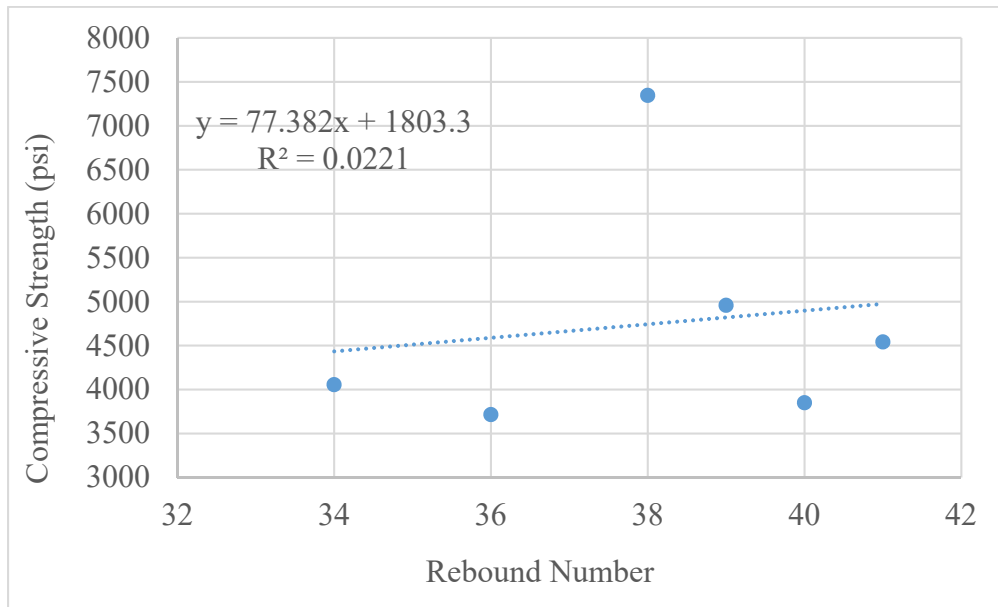
Figure G.1: Rebound-Strength Relationship for Slab 3 with No Overlay
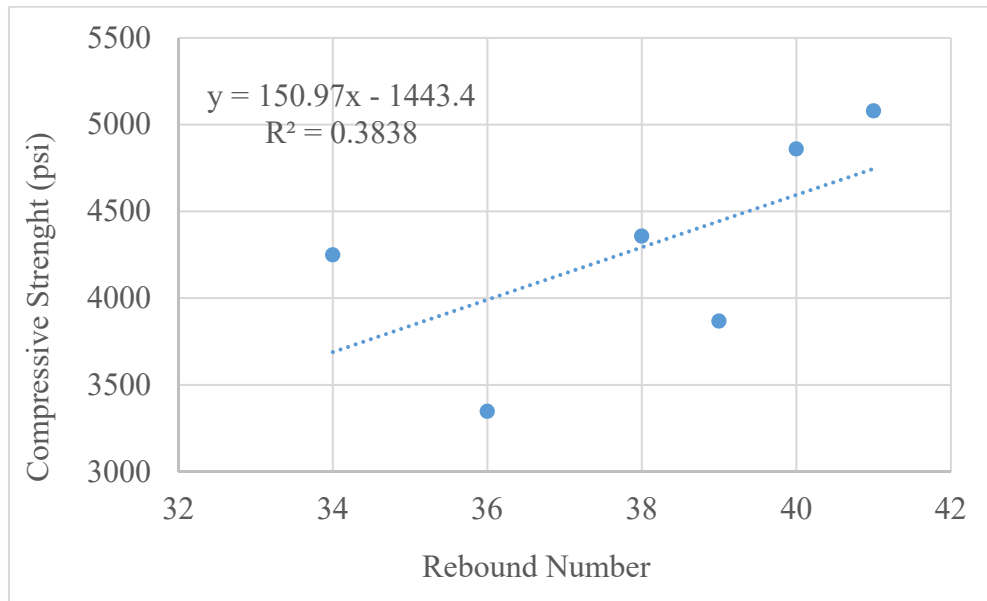
Figure G.2: Rebound-Strength Relationship for Slab 3 with Overlay
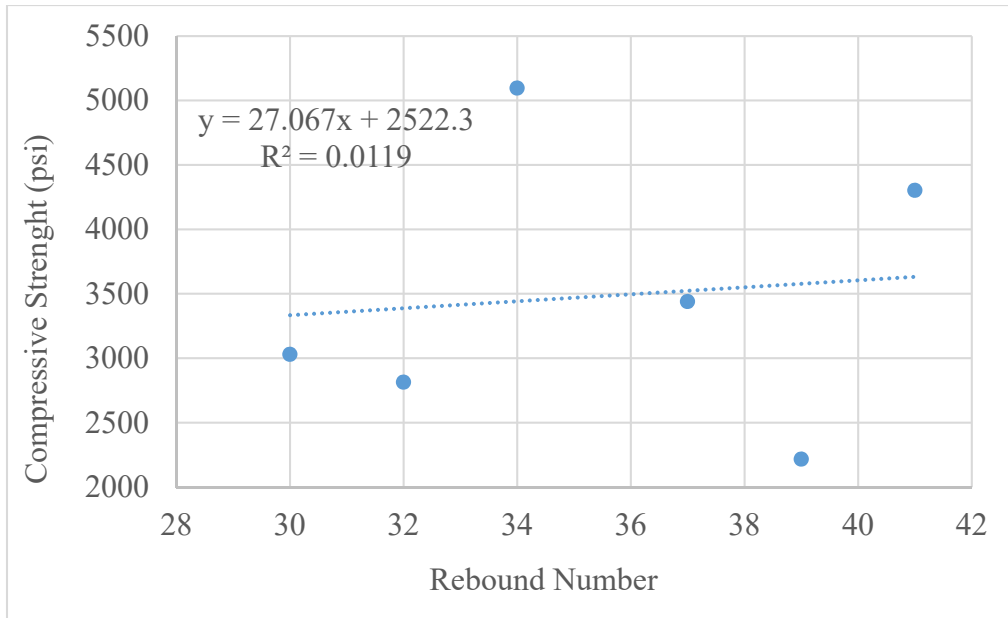
Figure G.3: Rebound-Strength Relationship for Slab 6
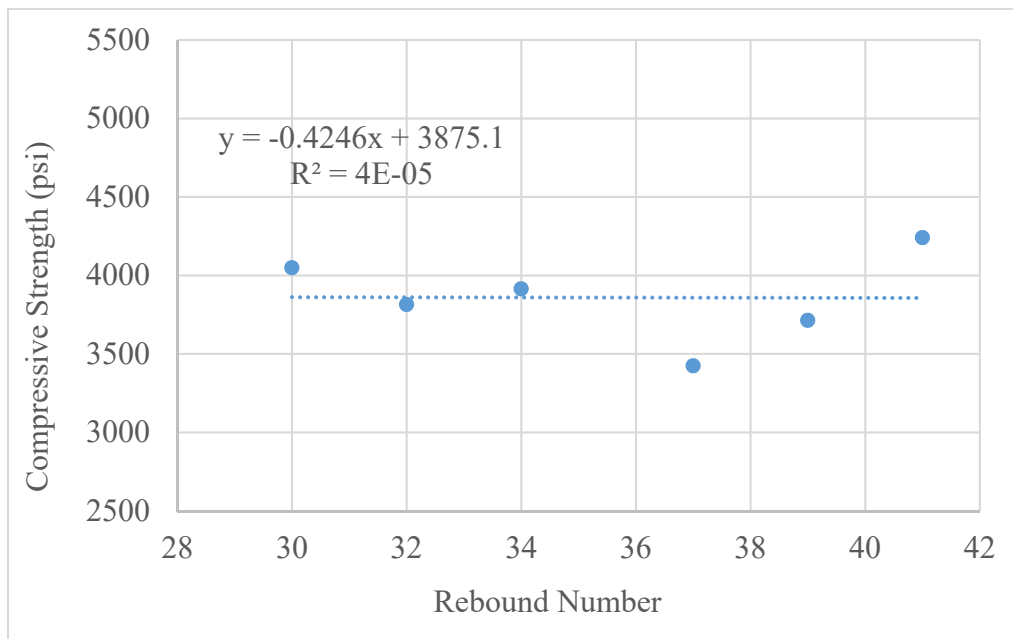
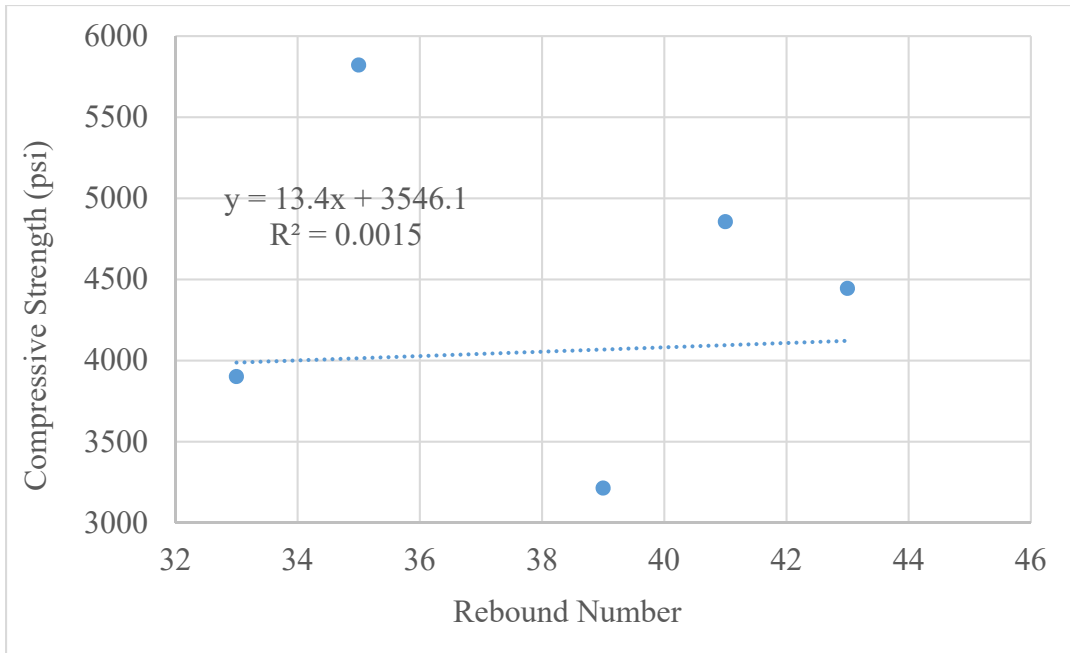Figure G.4: Rebound-Strength Relationship for Slab 6 with Overlay

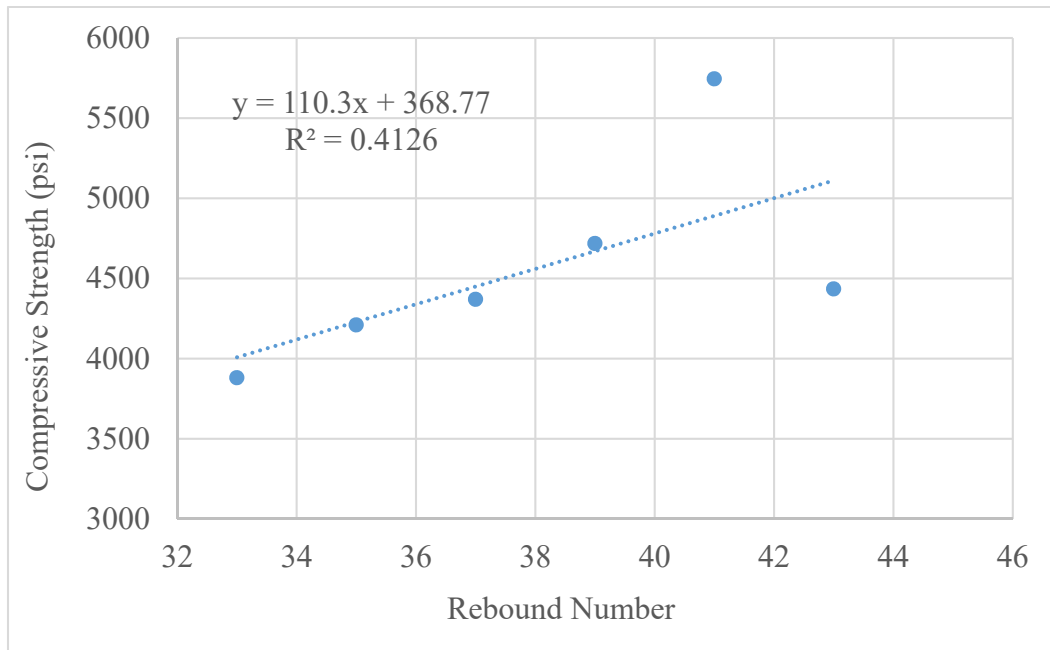Figure G.5: Rebound-Strength Relationship for Slab 7

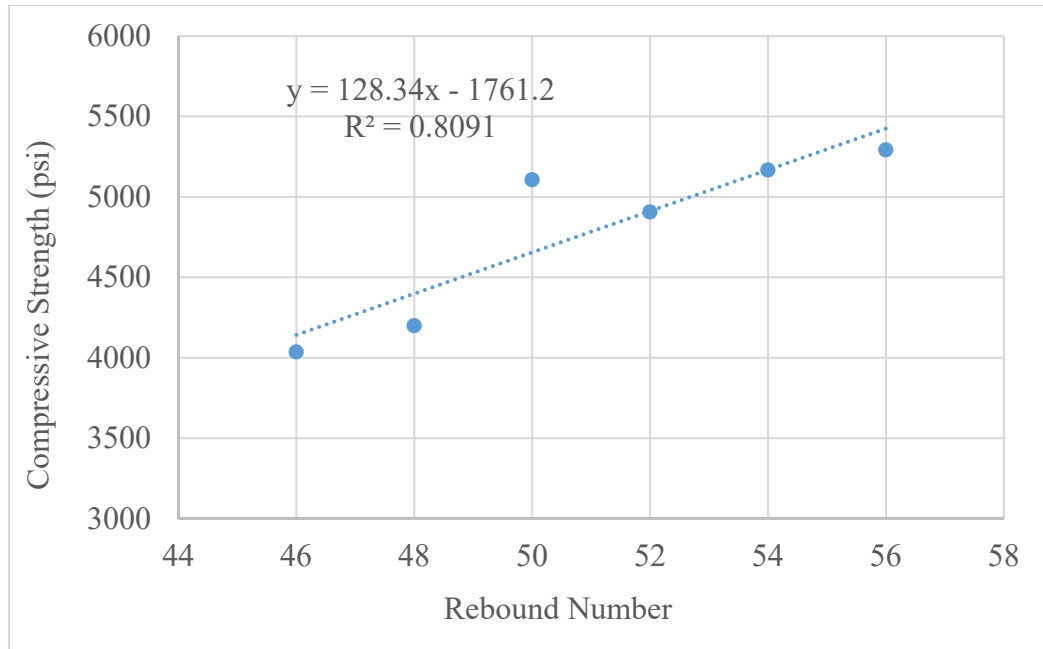Figure G.6: Rebound-Strength Relationship for Slab 7 with Overlay

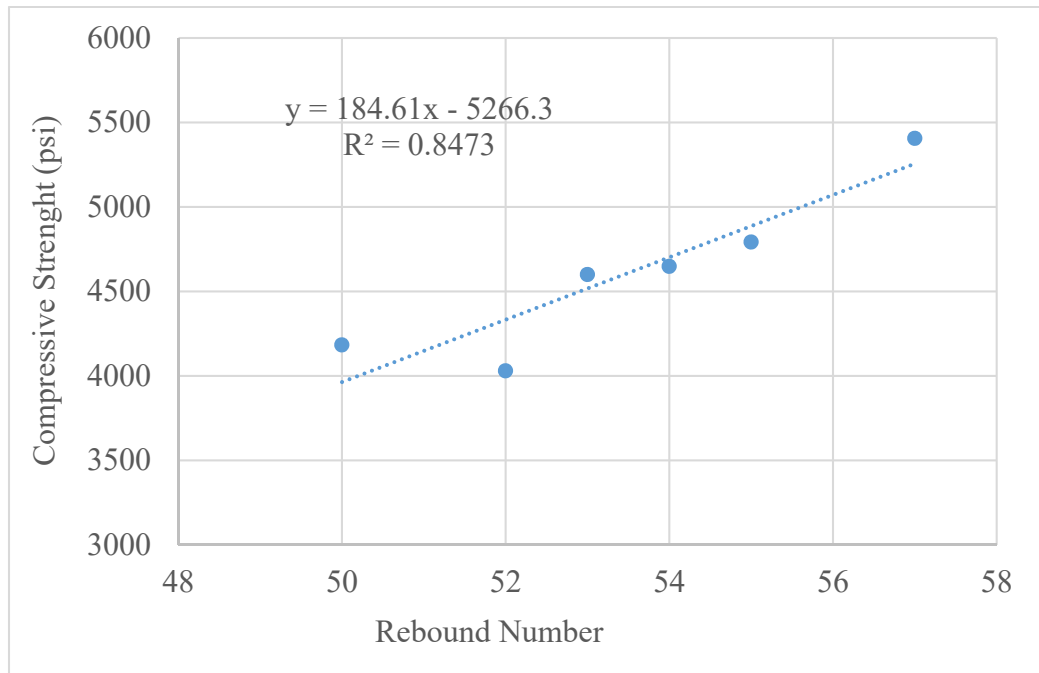Figure G.7: Rebound-Strength Relationship for Slab 1

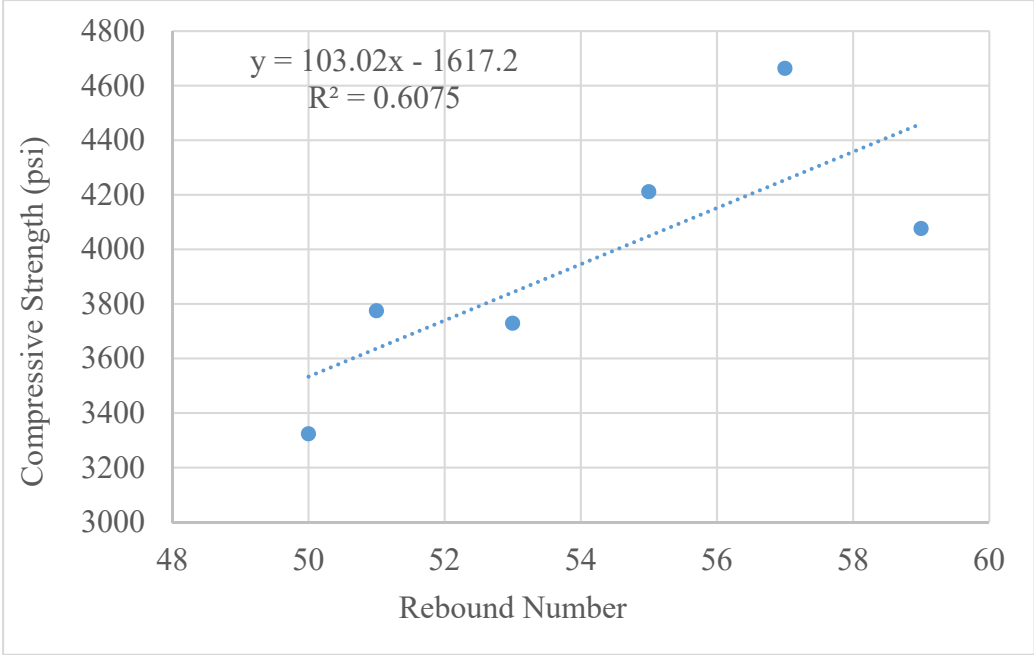Figure G.8: Rebound-Strength Relationship for Slab 4

Figure G.9: Rebound-Strength Relationship for Slab 9

VITA

Kristin Michelle Karleskint

Candidate for the Degree of

Master of Science

Thesis: NONDESTRUCTIVE TESTING FOR CORROSION ASSESSMENT OF EPOXY COATED REBAR

Major Field: Civil & Environmental Engineering

Biographical:

Education:

Completed the requirements for the Master of Science in Civil Engineering at Oklahoma State University, Stillwater, Oklahoma in December, 2020.

Completed the requirements for the Bachelor of Science in Civil Engineering at Oklahoma State University, Stillwater, Oklahoma in May, 2018.

Experience:

Kimley-Horn Structural E.I.T. – September 2020 to December 2020

Oklahoma Department of Transportation E.I.T. – December 2018 to July 2020

Professional Memberships:

Chi Epsilon

Tau Beta Pi